A HYBRID SOFT SOIL TIRE MODEL (HSSTM) FOR VEHICLE MOBILITY AND DETERMINISTIC PERFORMANCE ANALYSIS IN TERRAMECHANICS APPLICATIONS

Shahyar Taheri

Dissertation submitted to the faculty of the Virginia Polytechnic Institute and State University in partial fulfillment of the requirements for the degree of

Doctor of Philosophy
In
Mechanical Engineering

Saied Taheri, Chair
Corina Sandu, Co-Chair
Mehdi Ahmadian
Pablo Alberto Tarazaga
Celal Guney Olgun

August 28, 2015
Blacksburg, Virginia

Keywords: Tire Modeling, Soft Soil, Mobility, Terramechanics

A HYBRID SOFT SOIL TIRE MODEL FOR VEHICLE MOBILITY AND DETERMINISTIC PERFORMANCE ANALYSIS IN TERRAMECHANICS APPLICATIONS

Shahyar Taheri

ABSTRACT

Accurate and efficient tire models for deformable terrain operations are essential for performing vehicle simulations. Assessment of the forces and moments that occur at the tire-terrain interface, and the effect of the tire motion on properties of the terrain are crucial in understanding the performance of a vehicle. In order to model the dynamic behavior of the tire on different terrains, a lumped mass discretized tire model using Kelvin-Voigt elements is developed. To optimize the computational time of the code, different techniques were used in memory allocation, parameter initialization, code sequence, and multi-processing. This has resulted in significant improvements in efficiency of the code that can now run close to real time and therefore it is suitable for use by commercially available vehicle simulation packages. Model parameters are obtained using a validated finite element tire model, modal analysis, and other experimental test procedures. Experimental tests were performed on the Terramechanics rig at Virginia Tech. The tests were performed on different terrains; tire forces and moments, soil sinkage, and tire deformation data were collected for various case studies based on a design of experiment matrix. This data, in addition to modal analysis data were used to validate the tire model. Furthermore, to study the validity of the tire model, simulations at conditions similar to the test conditions were performed on a quarter car model. The results have indicated the superiority of this model as compared to other lumped parameter models currently available.

ACKNOWLEDGEMENTS

Firstly, I would like to express my sincere gratitude to my advisor Prof. Saied Taheri and my co-advisor Prof. Corina Sandu for their continuous support of my PhD study and related research, for their patience, motivation, and immense knowledge. Their guidance helped me during the research conducted and the writing of this thesis. I could not have imagined having better mentors for my PhD study.

Besides my advisors, I would like to thank the rest of my committee: Prof. Mehdi Ahmadian, Prof. Pablo A. Tarazaga and Prof. Celal G. Olgun, for their insightful comments and encouragement, which helped me to widen my research from various perspectives.

This project is funded in part by the Automotive Research Center, a U.S. Army Center of Excellence for Modeling and Simulation of Ground Vehicles. I want to thank my quad members, Dr. David Gorsich and Dr. Paramsothy Jayakumar from TARDEC, Dr. Brant Ross from Motion Port, and Mr. Daniel Christ from Michelin for all of the time and support they have dedicated to me.

To my friends and colleagues at Center for Tire Research (CenTiRe), Advance Vehicle Dynamic Laboratory (AVDL), and Center for Vehicle Systems and Safety (CVeSS): thank you for listening, offering me advice, and supporting me through this entire process. I would also like to show my gratitude to Dr. Schalk Els and his group at University of Pretoria for sharing some experimental data with me, and to Emilio Jimenez who participated in collecting part of it during the EVE project funded by the European Commission.

Last but not the least, I would like to thank my family: my parents, my brother, and my fiancé for supporting me, encouraging me in all of my pursuits, and inspiring me to follow my dreams.

TABLE OF CONTENTS

LIST OF FIGURES

LIST OF TABLES

NOMENCLATURE

A	Area
A_l	Rigid area of a track link as a proportion of its nominal contact area
A_u	Parameter characterizing terrain response to repetitive loading
a	Half of the contact patch
B	Wheelbase
b	Smaller dimension of a rectangular plate or the radius of a circular plate; width
b_{ti}	Tire width
b_{tr}	Track width
CI	Cone index
c	Cohesion
D	Diameter
D_h	Hydraulic diameter
D_r	Relative density
d	Diameter
E	Modulus of elasticity
e	Void ratio; base for the natural logarithm
F	Function; thrust, tractive effort
F_x	Longitudinal force
F_y	Lateral force
F_z	Vertical force
F_d	Drawbar pull
F_v	Tractive effort developed on the vertical shear surfaces on both sides of a track
f_0	Yield strength of an ice layer in tension; coefficient of track internal resistance
f_t	Radial deflection of the wheels of a track system
G	Sand penetration resistance gradient
G_e	Effective sand penetration resistance gradient
H	Horizontal component of a tension force

h	Thickness tire section height
h_l	Lug height
κ	Slip
j	Shear displacement
K	Shear deformation parameter
K_1, K_2	Parameters characterizing the shear stress–shear displacement relationship
k	Stiffness; resultant pressure–sinkage parameter
k_c, k_ϕ	Pressure–sinkage parameters in the Bekker equation
$k_c^{'}, k_\phi^{'}, k_c^{''}, k_\phi^{''}$	Pressure–sinkage parameters in the Reece equation
k_0	Parameter characterizing terrain response to repetitive loading
$k_{p1}, k_{p2}, k_{z1}, k_{z2}$	Pressure–sinkage parameters for snow cover
k_u	parameter characterizing terrain stiffness during the unloading–reloading cycle
L	Perimeter; characteristic length for an ice layer
L_t	Length of track in contact with terrain
l	Length
M_o	Limit bending moment per unit length of an ice layer
MI	Mobility index
m, m_m	Parameters characterizing the relation between the strength of the muskeg mat and that of the underlying peat
N	Number
N_c	Clay–tire numeric
N_{cs}	Cohesive-frictional soil–tire numeric
N_s	Sand–tire numeric
n	Exponent of sinkage
P	Load; power; spherical pressure
P_{co}	Collapse load for an ice layer
P_d	Drawbar pull
p	Pressure
p_{c0}, p_{c1}, p_{c2}	Collapse pressures for an ice layer

p_{cr}	Critical inflation pressure
p_g	Ground pressure
p_i	Tire inflation pressure
p_u	Pressure at the beginning of unloading in a loading–unloading–reloading cycle
p_w	Pressure–sinkage parameter for a snow cover
q	Surcharge; pressure exerted on the muskeg mat by the underlying peat
R	Radius; deviatoric stress
R^2	Coefficient of determination
R_c	Resistance due to terrain compaction
RCI	Rating cone index
r	Radius
s	Shear stress
$s_{\max}$	Maximum shear stress
T	Tension
V_j	Slip velocity
W	Load, weight
w_r	Weighting factor
z, z_o	Sinkage
z_u	Sinkage at the beginning of unloading in a loading–unloading–reloading cycle
z_w	Pressure–sinkage parameter for a snow cover
α	Tire slip angle
γ	Density
δ_t	Tire deflection
η	Efficiency
θ	Angle
μ	Poisson's ratio; drawbar coefficient; coefficient of friction
λ	Lagrange multiplier
σ	Normal stress
τ	Shear stress

ϕ	Angle of shearing resistance
ω	Angular speed

Chapter 1: Introduction.

1.1. Overview

The tire forces and moments depend on the structural behavior of the tire, as well as tire-terrain interaction. Therefore, based on the simulation application (e.g., handling, ride, mobility, durability), and type of the terrain (e.g., deformable, non-deformable, even, uneven) the approach for modeling the tire and the terrain would be different. The tire models that are used for vehicle simulation on mainly non-deformable terrains, such as FTire [1], RMOD-K [2, 3], CDTire [4], can be categorized based on usage, accuracy, computational efficiency, and degree of parameterization. The number of degrees-of-freedom (DOFs) and consequently the computational effort in these models can be sorted from empirical models (lowest) to finite element models (highest).

A direct application of an on-road tire model to simulate tire performance on soft soil is not feasible. This is due to the fact that traveling on deformable terrain raises issues for which on-road tire models do not account for. Moreover, the kinetics and kinematics of the tire on deformable terrains are subjected to different design and operational factors, as well as field characteristics. These factors, in addition to the uncertainties that exist in their parameterization, make the formulation of tire-terrain interaction a highly complex problem. Due to this complexity, the number of tire models, similar to the one developed in this research, which are usable in conjunction with multibody dynamic vehicle simulation models, are limited.

The proposed process of developing the complete soft soil tire model can be divided into two main sub-processes of mathematical modeling and physical modeling, as shown in Figure 1. For the mathematical modeling, different components of the system, such as tire materials, tire

structure and tire-ground interactions are described using semi-empirical mathematical correlations. Next, these mathematical models are implemented using a programing language, such as MATLAB. The developed code is checked to confirm that the model is correctly implemented and is free of errors. Meanwhile, a physical representation of the problem is essential to provide an insightful look into the real world situation. In this regard, a design of experiment case study was conducted to identify required experiments. The type and configuration of these experiments, which are required for both validating and parameterizing the implemented sub-models, are developed as a design of experiment table.

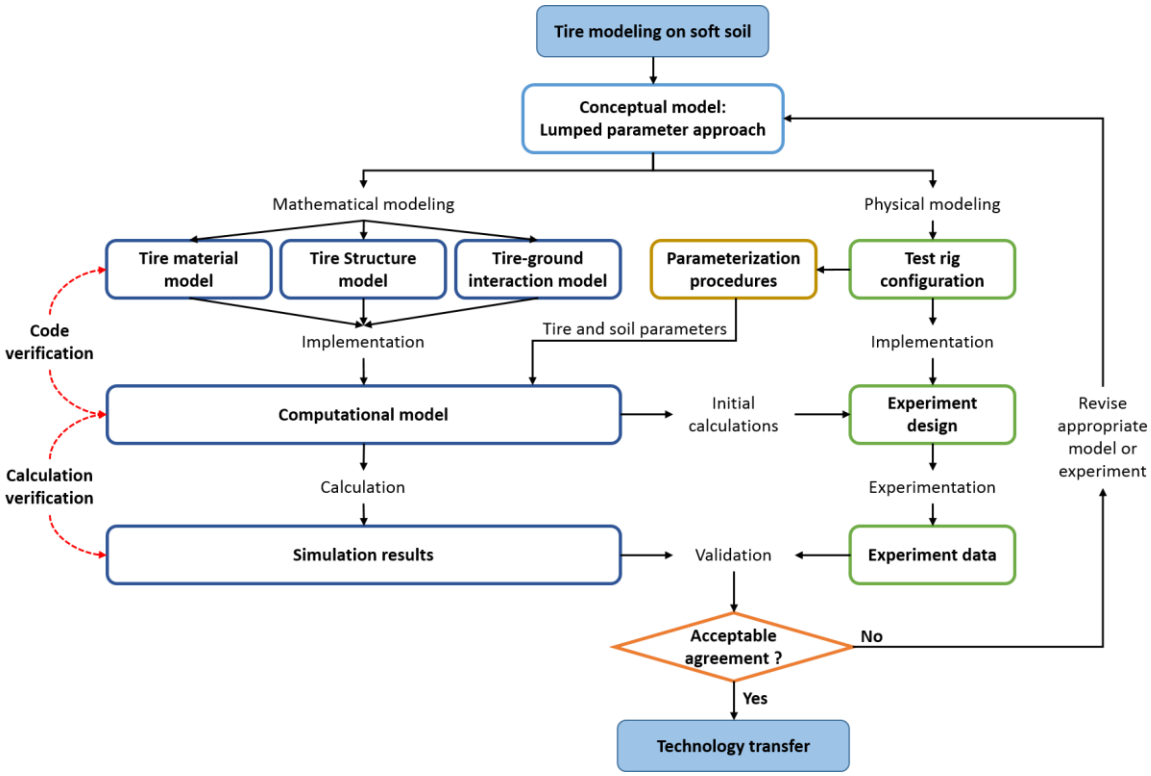

Figure 1: Tire modeling on the soft soil: Modeling, simulation, and experimental procedures work flow.

Using the parameters derived for the computational model, simulations are performed at conditions similar to the experiments. The results from this step are iteratively generated and compared to the test data until the acceptable agreement is achieved. In case the correlation accuracy was not achieved after extensive simulation iterations, the judgment is made whether to

make changes to one of the sub-models, experimental setup, parameterization procedures, or all of the above. The detailed description of the discussed steps will be given in the following chapters.

1.2. Objectives

The main objective of this study is to develop a new tire model for estimating tire forces and moments with high fidelity in terramechanics applications. The tire model is integrated with vehicle simulation software in order to simulate the tire forces and moments at the spindle in addition to the terrain response parameters such as sinkage and pressure distribution. Using this simulation test bench, the performance of the vehicle during handling maneuvers on various terrains is studied.

1.3. Methodology

The methodology of this study can be described as follows:

- Characterize the tire structure using a three-dimensional lumped parameter approach
- Include tire deformation in the contact patch, inflation pressure effect, and tread design
- Describe the material response of main tire components including sidewall, carcass, and tread to load/deformation inputs
- Model the interaction of the tire with rough non-deformable terrains with various wavelengths
- Specify the mechanical response of different terrains including mineral, muskeg, and snow covered terrains to tire inputs
- Parameterize the tire model as well the terrain model based on the measurement data from the control tire and studied terrain

- Implement a simulation environment that allows integration of the tire model with a vehicle simulation software in order to conduct full vehicle simulations
- Study the performance of the vehicle in various handling maneuvers on different terrain conditions

1.4. Overview of the Study

In the upcoming chapters the following are presented: A literature survey has been conducted to identify the previous efforts made in estimating the vehicle performance in terramechanics applications. The available models are categorized based on their underlying approach. The models from the same category are compared in terms of applications, parameterization, outputs, etc. Next, the methodologies for modeling the tire components material and structure are elaborated. Furthermore, the tire-terrain interaction is individually formulated for non-deformable and deformable terrains. The models for tire structure, tire material, and terrain are implemented in a unified model package, and the interface for communicating with a full-vehicle simulation software is established.

Moreover, the experimental procedures that are conducted for parameterization and validation purposes are described. The required tire model parameters are identified using the experimental data as well as the virtual test results from a previously developed FEM tire model. Using the developed tire model simulation test bench, the validation studies are conducted, and performance of the tire model is evaluated.

Chapter 2: Literature Survey

2.1. Introduction

Modeling the interaction of a vehicle with the terrain is a key part of the vehicle performance evaluation. In order to assess the vehicle performance within a simulation environment, research studies have been conducted to capture the physics within a mathematical framework. The vehicle performance can directly be correlated to the forces and moments between the tire and the ground and indirectly related to the variations of the terrain such as sinkage. The changes in the terrain properties can be neglected in case of a non-deformable terrain. For this type of terrain, researchers have developed various high fidelity models that can capture the tire response properties [2, 5-7]. Additionally, multiple commercial tire models have been developed for integration with vehicle simulation programs [3, 4, 8].

A direct application of an on-road tire model to simulate tire performance on soft soil is not possible. This is due to the fact that traveling on deformable terrain raises issues that on-road tire models do not account for. Moreover, the kinetics and kinematics of the tire on deformable terrains is subjected to different design and operational factors as well as field characteristics. These factors, in addition to the uncertainties that exist in their parameterization, make the formulation of tire-terrain interaction a highly complex problem.

The main objective of tire studies in the area of Terramechanics [9] is to determine the force and moment characteristics of the tire on a deformable (or, in general, an unprepared) terrain. This same criterion is also considered for the performance evaluation of the tire on soft soil. The secondary objective is to evaluate the effect of the tire passage on the geometrical and mechanical properties of the terrain such as soil height, compaction, erosion, and flow. This objective is very important in agricultural studies for assessing the effect of machinery on the soil.

The interaction of a wheeled vehicle with the ground results in normal and tangential stress fields in the contact patch of the tire. The integration of contact patch stresses in vertical and longitudinal directions produces resultant ground forces and moments. These forces and moments are related to operational parameters like slip ratio, slip angle, normal load, and inflation pressure.

Additionally, contact patch stress fields result in geometrical and mechanical changes in both the tire and the terrain. The geometrical changes include tire belt deformation in addition to soil sinkage, soil erosion and particles flow. The mechanical changes in the tire include variation of the tire structural stiffness and damping properties. Similarly, the mechanical changes in the soil cause variations of soil dry bulk density, compaction, and water content during the loading process.

Therefore, the tire-terrain interaction physics should be characterized initially for simulating the behavior of the tire-terrain interactions in off-road conditions. The main challenge in this regard is identifying and formulating the stress fields in the tire-terrain contact patch. These stress fields are influenced by kinetics and kinematics of both the tire and the terrain. The comprehensive characterization of this interaction requires detailed modeling of both the tire and terrain. Most of the Terramechanics models that are described in this paper, consider some preliminary assumptions in order to simplify this interaction. These simplifications are based on the application of the model, and require computational and experimental resources.

2.2. Terramechanics Models for Wheeled Vehicles

The terramechanics term is defined as the science of studying soil properties during interaction with tracked and wheeled vehicles (first defined by the U.S. Army Tank-Automotive Research Development and Engineering Center, TARDEC [9]). This paper reviews the studies that include the effects of the wheeled vehicles on deformable terrains. As it was mentioned earlier, the main challenge in studying the behavior of the vehicle in off-road condition is characterizing the tire-

terrain interaction (terramechanics). Throughout the years, a wide variety of models have been developed for formulating and simulating this interaction. The degree of complexity for these models is based on the application, accuracy and computational cost of development. Generally, these models can be grouped into three main categories: 1) Empirical models, 2) semi-empirical models, and 3) physics-based models. In this study, we will review the most relevant models in each category with a brief description of the proposed method, its capabilities in addition to its limitations. At the end of each section, there are two summary tables for the related family of models. The first table describes the following criteria: types of tire and soil studied; conditions in which simulations are performed; modeling technique for describing tire and terrain; computational effort; and advancements over previous studies introduced by a new model. The second table compares the common simulation outputs of each study in addition to its supplementary outputs. Readers can use these comparison tables for weighing the benefits of different methods to choose the suitable option based on their application. In conclusion, it should be mentioned that the main focus of this survey is to compare the methodologies used by different authors and for more detailed information about the modeling and experimental aspects, the reader should refer to the original text.

2.3. Empirical Models

The empirical models are usually used for simple vehicle mobility assessment like go or no-go situations. These models are purely based on laboratory (indoor) or field (outdoor) test data. The process of constructing an empirical model can be performed in three main steps. The first step is identifying the influential factors in the vehicle performance that can be specified using measurements. One of these empirical factors that researchers widely use is the vehicle mobility number. The vehicle mobility number, as a dimensionless variable, is a function of soil strength,

tire load, and tire geometry properties including width, diameter, section height, and deflection. There are different variations for this number; however, most of them are calculated by multiplying the wheel numeric (N) by a unique coefficient (k), where:

$$N = \frac{CI \cdot b \cdot d}{W} \cdot (k) \tag{1}$$

In Table 1, some of the most commonly recognized coefficients that researchers used, for calculating wheel mobility number, are shown:

Table 1: Wheel mobility number coefficients

Author	Wheel mobility number Coef.	Ref.
Wismer and Luth	$k_w = 1$	[10]
Freitag	$k_F = \sqrt{\frac{\delta}{h}}$	[11, 12]
Turnage	$k_T = \sqrt{\frac{\delta}{h}} \frac{1}{1 + b/2d}$	[13]
Brixius	$k_B = \left(\frac{1 + 5\delta/h}{1 + 3b/d} \right)$	[14]
Maclaurin	$k_M = \frac{\delta^{0.4}}{b^{0.2} d^{0.2}}$	[15-17]
Rowland Peel	$k_T = \sqrt{\frac{\delta}{h}} \frac{d^{0.15}}{b^{0.15}}$	[18, 19]
Hegazy and Sandu	$k_{HS} = \sqrt{\frac{h - \delta}{d}}$	[20]

Where δ is the tire deflection, h is the tire section height, b is the tire section width, and d is the overall tire diameter. The second step for characterizing the empirical model is to conduct wheel mobility experiments using various inputs such as wheel mobility number. Finally, using curve-fitting techniques, the trend in the data is captured by assigning the appropriate functions across the range of the given inputs. The following sections introduce the most important studies

that have been conducted based on purely empirical methods.

The experimental results investigated by researchers [20] showed that the wheel numeric increases nonlinearly when the tire load decreases, the tire diameter increases, the tire pressure decreases, and the tire width decreases. While not intuitive, since the tire parameters used were not independent, these results accurately reflect the data experimentally collected. For soil strength, the wheel numeric increases linearly when the soil strength increases.

2.3.1. WES VCI Model

The VCI model was proposed by the US Army Corps of Engineers Waterways Experiment station (WES) [21] in 1971. In this model a range of typical off-road vehicles are tested on inorganic fine and coarse-grained soils. Then, vehicle performance parameters such as drawbar pull, motion resistance, and vehicle cone index (VCI) are correlated to cone index (CI) for coarse grained soils and rating cone index (RCI) for fined-grained soils. For distinguishing between terrain types, a number 200 sieve is used. In this way, if more that 50 percent of soil grains (by weight) pass the sieve, the soil is considered fine grained; otherwise, it is coarse grained. The cone index factor is used to include the soil strength in the model. The cone index is defined as the force per unit area that is required to penetrate a cone-shaped probe into the soil with a steady state rate, and varies with the depth of penetration. The cone index incorporates the values for soil cohesion, angle of internal friction, and soil-metal friction in a single combined parameter. The flowchart for this process is illustrated in Figure 2.

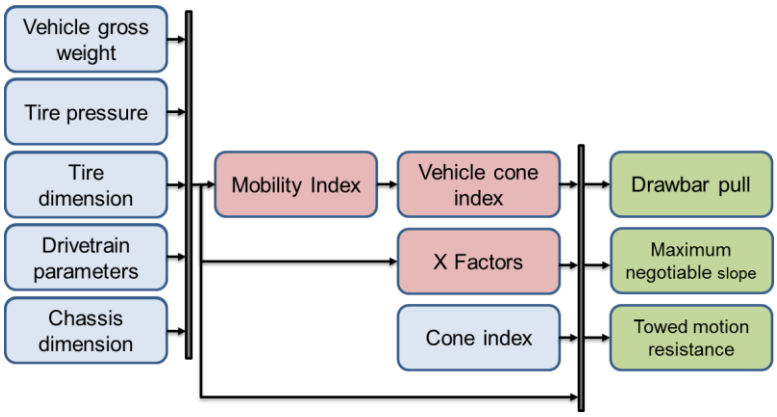

Figure 2: Process flowchart for WES VCI Model. Blue boxes (test data), red boxes (intermediate process parameters), and green boxes (vehicle performance factors as model outputs)

The Army uses the measured parameters of tire, drive train, chassis, and soil as the input data. Then based on a series of developed empirical equations, it calculates the mobility index and a series of correction factors (X factors). If the mobility index exceeds the cone index, then motion is possible; otherwise the vehicle will be stuck. Applying the linear and curvilinear regression techniques derive the empirical soil-vehicle performance equations for this model. The mobility index of the soil is used for computing the vehicle cone index, which is an indication of minimum required strength for critical soil layer to allow the vehicle pass a certain number of times. In conclusion, the vehicle performance parameters including draw bar pull, maximum negotiable slope and towed motion resistance are computed as the model outputs.

2.3.2. WES Mobility Numeric Model

The WES mobility numeric model developed in [22] is based on the dimensional analysis of the laboratory test data for straight line steady state motion of the tire on remolded clay and dry sand. In this model, performance parameters such as minimum soil strength to negotiate the first pass, drawbar pull, input torque at 20 percent slip, and towed motion resistance are related to a unique mobility numeric using experimental functions [23]. The mobility numeric is a dimensionless load factor that describes the ratio of soil strength to a nominal unit load that

deflected tire applies to the soil. These numeric values are calculated via empirical formulation and using input data such as cone index, tire geometry, vehicle load, and etc. The clay-tire numeric (N_c) and sand-tire numeric (N_s) for tires operating in the purely cohesive soils and frictional soils, respectively, are expressed as

$$N_c = \frac{Cbd}{W} \cdot \left(\frac{\delta}{h}\right)^{1/2} \cdot \frac{1}{1+(b/2d)} \tag{2}$$

$$N_s = \frac{G(bd)^{3/2}}{W} \cdot \left(\frac{\delta}{h}\right) \tag{3}$$

In the above equations, C is the cone index, b is the tire section width, d is the tire diameter, W is the tire load, δ is the tire deflection, h is the unloaded tire section height, and G is the sand penetration resistance gradient. These numeric values were further revised by Turnage [24] to include additional tire-soil parameters such as soil moisture content, soil relative density, void ratio, sand compatibility (difference between soil loosest and densest state void ratio divided by the densest state void ratio), sand grain median diameter (the median diameter for the 50 % finer portion of the soil by weight). These enhancements extended the performance prediction range of the model to a more comprehensive range of soil types. Also, in the subsequent studies it was shown that the initial idea of describing the terrain solely based on simple cone penetrometer measurements was not sufficient, and a set of field measurements including compatibility test and grain size distribution analysis is essential to describe the properties of the particular sand.

2.3.3. Deere & Company Technical Center Models

A similar approach to WES was proposed by Wismer and Luth [10] in 1973. According to Buckingham Pi theorem, authors considered seven dimensionless ratios to fully formulate the wheel-soil performance prediction model. Their model later was revised by Brixius [14] for mobility prediction of agricultural vehicles with bias ply tires. Brixius also included the effect of

the wheel slip, and based on the curve fitting to over 2500 test data that were collected for 121 soil-tire combinations, developed the required mathematical relations. These relations correlate wheel torque, motion resistance, tractive and net pull efficiency to wheel load, soil strength, tire geometry, and tire deflection. Additionally, Wismer and Luth compared the validity of their model with WES model, and concluded a reasonable agreement between the models for similar soil strength and slip values.

2.3.4 STIREMOD

The STIREMOD [25, 26] is a model created by Systems Technology Inc. as a part of the VDANL vehicle dynamics computer simulation software effort sponsored by the US Army TARDEC. The model was developed for paved surfaces and was then extended to un-paved off-road conditions by applying empirical shaping functions developed by Metz [27]. The general tire-road characteristics that are modeled are longitudinal and lateral forces in addition to aligning moment. Characteristics features of these parameters such as adhesion region gradient, peak coefficient of friction before entering the saturation region, and limiting force reduction at higher slip values are considered in the relations. The STIREMOD formulations are based on a quadratic slip function σ that is a representation of combined lateral and longitudinal slip. In order to establish the empirical formulation, first a set of initial parameters including composite slip σ, tire contact patch length a_p, lateral stiffness coefficient Ks, longitudinal stiffness coefficient Kc, and force saturation function $f(\sigma)$ are calculated from the test data.

The composite slip is defined as:

$$\sigma = \frac{\pi \cdot a_p^2}{8\mu \cdot F_z} \sqrt{K_s^2 \cdot \tan^2 \alpha + K_c^2 \left(\frac{S}{1-S} \right)^2} \tag{4}$$

Where S is the longitudinal slip, and α is the slip angle. Then the force saturation function is

introduced as a ratio of curve-fitted polynomials which in turn implicitly defines a load normalized composite force as:

$$N_s = \frac{G(bd)^{3/2}}{W} \cdot \left(\frac{\delta}{h}\right) \tag{5}$$

Metz introduced an exponential model for lateral forces during pure cornering. STIREMOD uses force saturation function shaping parameters to match the filed data with exponential shape of the Metz model. The final form of the lateral force function is:

$$\frac{F_y}{F_z} = A\frac{\frac{\left(\frac{B}{DsD\alpha}\right)^3}{6}\sigma^3 + \frac{\left(\frac{B}{DsD\alpha}\right)^2}{2}\sigma^2 + \left(\frac{B}{DsD\alpha}\right)\sigma}{\frac{\left(\frac{B}{DsD\alpha}\right)^3}{6}\sigma^3 + \frac{\left(\frac{B}{DsD\alpha}\right)^2}{2}\sigma^2 + \left(\frac{B}{DsD\alpha}\right)\sigma + 1} \tag{6}$$

Essentially, this model introduces “effective coefficients of friction” to simulate the increase resistance forces generated during running on an off-road terrain. Table 2 shows the list of the model parameters for different terrains.

Table 2: List of Metz's model parameters for evaluation of lateral force

Surface	A	B	C	D	M
Pavement	0.67	0.17	0.677	0.563	0.14
Plowed field	0.65	0.07	0.267	0.222	0.14
Gravel .56	0.52	19	0.588	0.489	0.14
Corn field	0.53	0.14	0.440	0.365	0.14
Meadow	88	0.15	0.784	0.652	0.14

The developed methodology can switch between different surfaces, which make it useful for analysis of highway shoulders and side-slopes. Furthermore, STIREMOD considers an

exponential relationship, similar to Wong [28] shear stress formula, for predicting the longitudinal force on deformable surfaces:

$$\frac{F_x}{F_z} = \tan(\phi)\left(1 - e^{-\Delta_s / X_c}\right) \tag{7}$$

Where D_s is the shear displacement, ϕ is the soil internal friction, and X_c is a characteristics compaction distance. The compaction distance is the amount of compaction that soil can handle without having significant property changes. The compaction distance value for materials such as sand is in the order of 0.1 feet. On the other hand, for the fields that have been plowed or furrowed, the compaction distance is on the order of a foot or tens of feet.

2.3.5. Summary Tables

Table 3: Summary of the features for purely empirical terramechanics models

First author (or model name if available)	Year	Application		Condition	Modeling approach	Computational effort	Advancement	Ref.
		Tire	Terrain					
WES VCI Model	1971	Truck tires	Inorganic fine and coarse grained soils	Steady-state	Correlating the performance parameters to cone index (CI)	Low	Including the effect of the drive terrain and chassis using correction factors	[22]
WES Mobility Numeric Model	1971	Truck tires	Remolded clay and dry sand	Steady-state	Correlating the performance parameters to mobility numeric	Low	Applying dimensional analysis to the test data	[22]
Wismer	1973	Agricultural bias ply tires	121 different soil-tire combinations	Steady-state	Correlating the performance parameters to seven dimensionless terms	Low	Including the effect of the wheel slip	[10]
Turnage	1984	Truck tires	Sand and clay	Steady-state	Correlating the performance parameters to three dimensionless terms	Low	Considering soil moisture content, soil relative density, void ratio, sand compatibility, and sand grain median diameter	[24]
STIREMOD	1997	Passenger and truck tires	Plowed field, gravel, pavement, corn field, and meadow	Steady-state	Applying empirical shaping functions to paved roads force-slip curve-fitting methods	Low	Introducing longitudinal and lateral force function vs. slip	[25]

Hegazy and Sandu	2013	Truck tire (7.5-R16)	Loose sand	Steady-state	Using a new mobility number in Brixus [14] equations for evaluating the mobility performance factors	Low	Using the tire parameters data from ultrasonic sensors, and proposing a new mobility number coefficient as a function of tire diameter and loaded height	[20]

Table 4: Summary of the verified output results for purely empirical models

First author (model name if available)	Motion resistance	Drawbar pull	Lateral force	Combined slip	Aligning moment	Bulldozing force	Multi-pass effect	Experimental validation	Additional outputs
WES VCI Model	✓	✓	×	×	×	×	×	✓	Maximum negotiable slop
WES Mobility Numeric Model	✓	✓	×	×	×	×	✓	✓	Minimum soil strength to pass
Wismer	✓	✓	×	×	×	×	✓	✓	Tractive and net pull efficiency
Turnage	×	✓	×	×	×	×	✓	✓	-
STIREMOD	×	✓	✓	✓	✓	×	×	✓	-
Hegazy and Sandu	×	✓	×	×	×	×	×	✓	Tractive and net pull efficiency

In conclusion, the purely empirical tire models are very useful as simple tools for evaluating the performance of the wheeled vehicles in conditions similar to the test environment and with tire properties similar to the test tire. Due to this limitation, empirical models cannot be used for extrapolating the results to the problems outside the scope of the experimental tests. Thus, a new tire design concept or testing the tire performance in a new operating condition cannot be studied using this family of terramechanics models. Also, the empirical models developed for passenger and truck size tires do not scale perfectly to the smaller size tires such as tires in robotic applications and lunar vehicles. More important, the dynamic response of the tire-terrain interaction cannot be captured for the time-varying elastic-plastic response of the terrain in the multi-pass iterations.

2.4. Physics-Based Models

Instead of relying on experimental analysis to characterize the tire-soil interaction, physics based models incorporate the physical principles and analytical methods to represent tire and terrain structures in addition to their interaction. This multi-disciplinary field of models incorporates applied mathematics, numerical analysis, computational physics, and even computer graphics to evaluate the performance of wheeled vehicles. The degree of complexity varies from the simple models that consider tire as a rigid ring and terrain as a spring-damper system to very detailed models that use finite element formulation for both tire and terrain. In the subsequent sections, the physics-based analytical tire models are discussed. Also, the summary of the main capabilities of these models is shown in Table 5. It should be noted that the majority of the physics based models, and especially those that use FEM and DEM methods, have high computational time requirements. For comparing the computational speed of these models, similar case studies with the same tire and soil input parameters should be simulated

on the identical hardware platform.

2.4.1 VTIM (Vehicle Terrain Interaction Model)

This model was proposed by Madsen and Seidel [29] in 2012, as a three-dimensional vehicle/terrain interaction model, which considers the deformation of both tire and terrain. The emphasis is on the real-time capability of the model in order to incorporate the model in a real-time vehicle dynamics simulator. Considering separate models for the soil and for the tire decouples the tire-terrain interaction. The tire modeling procedure is similar to the one proposed by Negrut and Freeman [30] for non-deformable surfaces. First, the tire circumference is divided into multiple lumped masses, which are connected to each other and to the rim by a set of springs and dampers in tangential and lateral directions. Additionally, the lumped masses are connected to the rim center by radial spring-damper elements. For simplification purposes, the dynamic behavior of the tire is excluded from this model. The components of the tire model are shown in Figure 3.

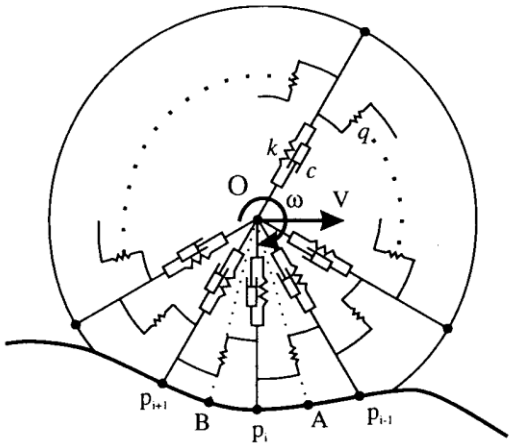

Figure 3: Tire structure model using Radial and inter radial spring damper system in VTIM

The terrain is discretized into a set of soil columns, and their deformation is related to the applied vertical stress using visco-elasto-plastic compressibility relationships. In order to find

the vertical stress distribution in the soil due to tire normal loading, the modified version of Boussineq and Ceruti soil mechanics equations [31] are used:

$$\sigma_z = \frac{vWz^v}{2\pi\left(r^2+z^2\right)^{(v/2v+1)}} \tag{8}$$

This equation calculates the stress (σ_z) at the depth z in a semi-definite, homogenous, isotropic elastic soil medium due to the point load (W) applied to the soil surface at the distance (r) from measurement point. Meanwhile, the Frohlich concentration factor (v) is applied to account for the soil cohesion. The value for this factor is considered $v=3$ for hard soil, $v=4$ for normal soil and $v=5$ for soft soil. Moreover, the vertical stress due to the horizontal point load applied to the soil surface is:

$$\sigma_z = \frac{3}{2\pi}\frac{r(\cos\Theta)}{\left(1+(r/z)^2\right)^{(5/2)}}\frac{H}{z^3} \tag{9}$$

Where H is the horizontal force and Θ is the angle between the direction of the applied force and direction of the vector connecting the position of the point load to the position at which the stress is calculated. The final vertical stress applied to a soil column is calculated by integrating vertical stresses over the soil element area. If the vertical loading compresses the soil with the initial bulk density of ρ_0, to final bulk density of ρ_1, the vertical displacement of the soil column with the initial height of (h) is:

$$z = (1-(\rho_0/\rho_1))\cdot h \tag{10}$$

The elastic plastic behavior of the soil in loading-unloading is found by multiplying the theoretical changes in bulk density with exponential decay functions ($1-e^{t/\tau}$) with individual compression and rebound time constants (τ_c and τ_r).

In order to determine the ground forces due to the longitudinal and lateral displacement of

the tire, the soil shear displacement is related to shear stress by the shear stress displacement model that was introduced by Janosi and Hanamato [32]. Furthermore, the bulldozing force that is applied to the tire sidewalls from the side soil wedges during sinkage is modeled via passive lateral earth calculations. If friction between the soil and tire is neglected, the maximum bulldozing force at the failure point of a displaced soil wedge is determined by

$$F = b\left(0.5\gamma Z^2 \cdot \tan^2(45+\phi/2) + 2cZ\tan\ (45+\phi/2)\right) \tag{11}$$

Where b is the width of the soil element, γ is the soil unit weight, Z is the tire sinkage, and $45+\phi/2$ is the angle of failure plane. To run the model in real time, the soil mechanics equations as well as the terrain geometry contact detection algorithm are implemented using a GPU-accelerated approach. Authors have conducted simulations including the vertical plastic deformation, and the required energy for performing soil plastic deformation.

2.4.2 Discrete Element Methods (DEM)

The main concept of discrete element methods stems from considering the soil as a system of discrete particles and models the mechanical interaction of the individual elements with adjacent elements, soil track, and the wheel. A number of past studies have established the mathematical framework for investigating the behavior of granular materials and more importantly mechanical interaction of the soil and machine [33, 34]. The application of DEM can be seen in terramechanics studies as well as other soil machine interaction studies such as, plane shearing of the soil, soil cutting by rotary tillage blade or plows [35].

Elements that are in contact with the wheel (track) receive the contact forces from the wheel (track) in addition to the forces from their neighboring elements. The resultant interaction forces in this method are calculated using force elements. The basic form of DEM assumes the stiffness and damping force elements in the normal and tangential directions between the

contacting terrain particles, as shown in Figure 4. Additionally a friction force element exists in the tangential direction that produces friction forces as the multiplication of friction coefficient and contact normal load. Same method is applied to calculate the contact forces between the terrain particles and tire (track).

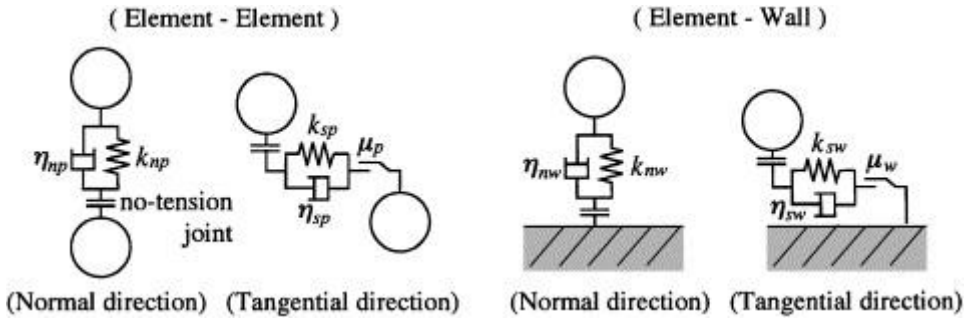

Figure 4: force elements between the elements and element/wall (Simulation of soil deformation and resistance at bar penetration by the Distinct Element Method, Tanaka, H., et al., Journal of Terramechanics, 2000. 37(1): p. 41-56, used with permission of Elsevier)

It should be mentioned that the viscous damping shown in Figure 4 is suitable for dry granular materials. In some studies, in order to include the effect of internal hysteresis loss due to deformation, this type of damping is replaced with Coulomb damping in both normal and tangential directions. Furthermore, to represent the cohesion of the soil and adhesion forces between particles and tire (track), adhesion elements is introduced by Asaf [36], as shown in Figure 5.

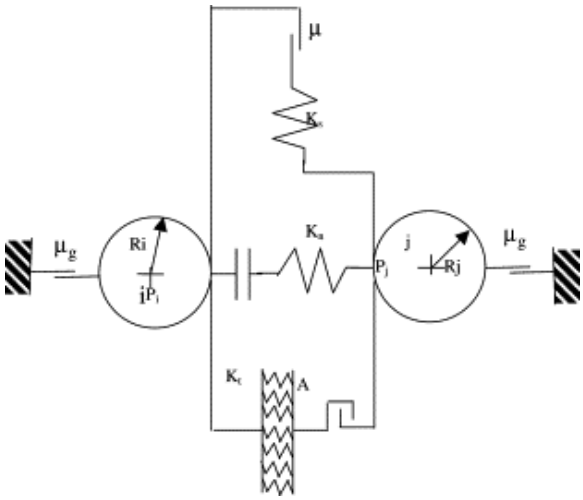

Figure 5: Representation of DEM including Coulomb damping, μ_g and cohesion element, K_t (Evaluation of link-track performances using DEM, Asaf, Z., D. Rubinstein, and I. Shmulevich, Journal of Terramechanics, 2006. 43(2): p. 141-161, used with permission of Elsevier)

The contact model is initiated with a quick search for possible interacting elements. Contact judgment is carried out by calculating the amount of the elements inter-penetration. The shape of the elements is considered as a circle in a two-dimensional analysis, and as a sphere in a three-dimensional analysis. Then, based on a penalty method, the contact forces between the interacting elements are expressed as the restoring force and the damping force proportional to the relative displacement and velocity.

Researchers who used DEM investigated different case studies and modified the theory and implementation techniques in order to achieve faster simulations with more accurate results (as compared to experimental data). Some of these researchers have incorporated the finite element method to model the effect of the tire contact patch and tire belt deformation on force characteristics. The description for the relevant models that have used the DEM method for studying the performance of the tire-wheel interaction is given in the following sections.

2.4.2.1. H. Nakashima and A. Oida FE-DE Model

One of the fundamental problems of the discrete element method (or distinct element

method) is the high computational cost due to the extensive contact detection steps as well as small time increments needed for capturing the dynamic of the system adequately. On the other hand, finite element methods are not able to handle the singular boundary conditions such as cases in which tire lug tip works as a singular stress point during tire soil interaction. In 2004, H. Nakashima and A. Oida [37] implemented a two dimensional combined FEM and DEM framework to tackle the difficulties mentioned above. In their study, they modeled the tire and lower soil layer using FEM, and the upper soil layer, which interacts with the wheel, using the DEM. Their DEM mathematical framework is based on the work which was performed by Oida [38, 39]. The finite element part of their model is originated from the previous efforts made by Nakashima for modeling the three dimensional tire-soil interactions [40, 41]. They have shown the qualitative accuracy of their model using a simple quasi-static sinkage simulation, which is shown in Figure 6.

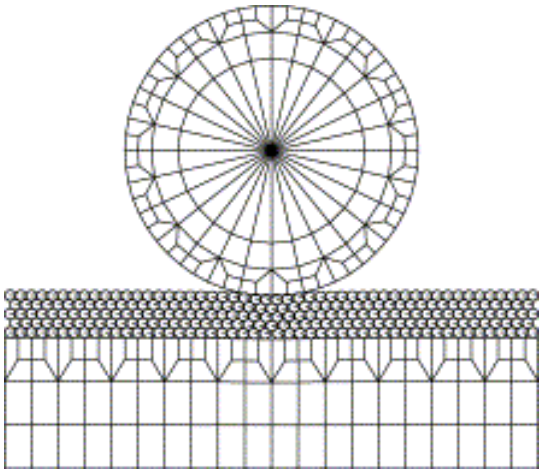

Figure 6: FE simulation of tire sinkage into a combined FE-DE soil bed with deformation shown after 15,500 time steps (Algorithm and implementation of soil–tire contact analysis code based on dynamic FE–DE method, Nakashima, H. and A. Oida, Journal of Terramechanics, 2004. 41(2–3): p. 127-137, used with permission of Elsevier)

2.4.2.2. F. Wakui and Y. Terumichi Model

In order to simplify the problem, most of the terramechanics models that incorporate the

discrete element method, consider tire as a rigid ring in a two-dimensional soil track. In 2010, F. Wakui and Y. Terumichi [42, 43] proposed a three dimensional tire-soil interaction model that adopts a lumped mass-spring system for the tire structure and a DEM with rigid soil particles for the soft ground formulation. Their tire model consists of a rigid cylinder rim, which is connected to a number of lumped masses located around the circumference of the tire. The connections are made using springs and dampers in radial, lateral and tangential directions as shown in Figure 7.

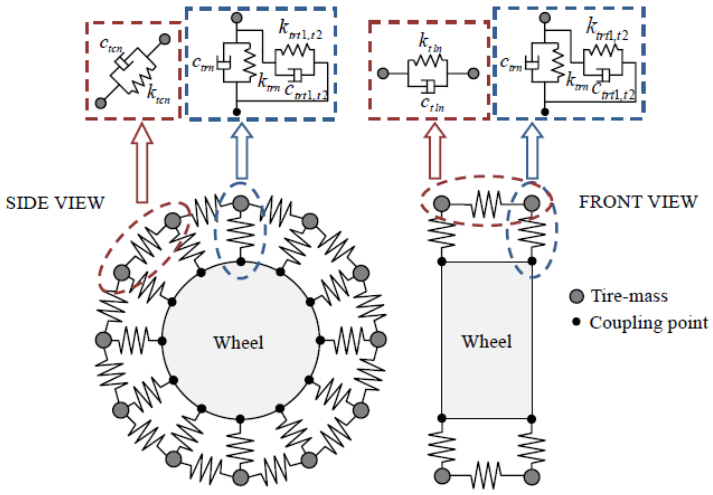

Figure 7: Modeling the tire using lumped mass approach (Numerical Simulation of Tire Behavior on Soft Ground, Wakui, F. and Y. Terumichi, Journal of System Design and Dynamics, 2011. 5(3): p. 486-500, used with permission of The Japan Society of Mechanical Engineers)

A numerical approach similar to the one proposed by Cundall [34] is used for modeling the soft ground. However, they modified the model in order to consider the actual non-spherical shape of the soil particles. Basically, the complicated polyhedrons shape of the soil particles constrains their rotation due to the clutching effect during contact. Limiting the rotational velocity of the soil particles captures this restraining behavior. This adjustment makes the interacting particles behave as a cluster of round grains, which in turn helps reduce the computational cost of the simulation.

Three-dimensional case studies including wheel drop test and tire translational and rotational motions are simulated using the DE soft ground model. Furthermore, tire performance in longitudinal, lateral and combined longitudinal and lateral with different slip ratios are compared qualitatively with previous cases. Additionally, in a later study by the same authors [43], the effect of soil grain shapes and terrain elastic-plastic properties on the tire driving performance is investigated. The elastic-plastic effect of the terrain in a multi-pass case is implemented using a set of parallel nonlinear springs and linear dampers that connect the lower ground masses of upper soft ground level to the base floor as seen in Figure 8. The nonlinear springs follow the modified Bekker's pressure equations suggested by Wong [44].

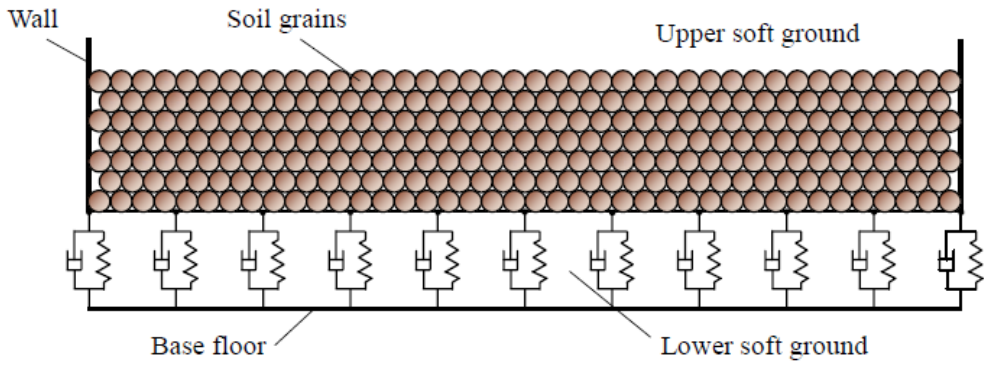

Figure 8: Combined DE and mass-spring soft ground model (Numerical Simulation of Tire-Ground System Considering Soft Ground Characteristics, Wakui, F. and Y. Terumichi, Journal of System Design and Dynamics, 2011. 5(8), used with permission of The Japan Society of Mechanical Engineers)

2.4.2.3. W. Smith and H. Peng Model

To study the mobility and performance of small unmanned ground vehicles (SUGVs) on uneven terrain, Smith and Peng [45] introduced this model. Since implementation of the widely used Bekker theory can lead to large errors, this method is claimed to be a good option for evaluating the performance of light-weight SUGVs. The DE algorithm was programed within the LIGGGHTS, which is an open source CFD-DEM software [46].

The DEM equations that specify the forces between particles and between particles and wall are decomposed into two three dimensional vectors including Hertzian friction force and cohesive forces. The Hertzian forces are applied in the normal and tangential directions to the contact plane where the tangential forces are limited by the maximum Coulomb friction. For the cohesive forces, a simplified Johnson-Kendall-Roberts method is used to include the cohesion of the soil as well as binding forces between the tire and soil particles. In view of the fact that spherical soil particles are used, a constant directional torque model is applied to simulate the interlocking actions between the particles [47]. The surface roughness is included in the model with its amplitude and frequency influencing the stress distribution in the tire contact patch. A soil packing strategy is used to tune the compaction of the terrain during the simulation. Meanwhile, the particles at the edges and bottom of the soil track are frozen to simulate the track boundary conditions.

In order to model the wheels, many spherical particles are attached together in a predefined manner to approximate the smooth surface of the tire circumference. The wheel properties are defined based on the experiments conducted by Harbin Institute of Technology and Cornell University on two sets of wheels named Ding and MER, respectively [48-50]. The simulation material parameters used in the ground model are similar to the properties of the lunar soil simulants used in the aforementioned studies which include dry sand for Harbin study and lunar regolith simulant JSC-1A for Cornel study. For validation, two groups of case studies are conducted in steady state and transient conditions and results are compared with the studies mentioned above. For steady-state simulations, wheel drawbar pull, sinkage and driving torque at a constant longitudinal velocity at different slip ratios are compared. For the transient simulations, the values for wheel sinkage and wheel torque in a digging test are evaluated over

the experimental results, as seen in Figure 9.

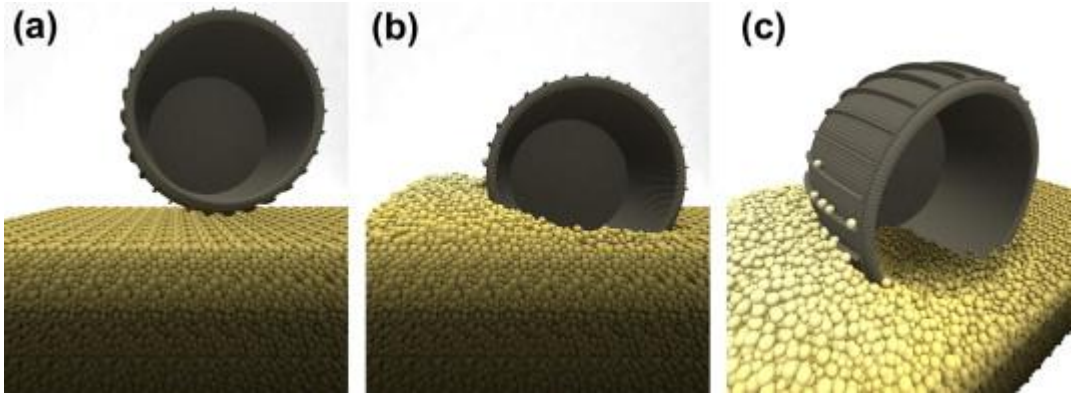

Figure 9: Simulation of the tire digging into the DE soil bed at t = 0 (a) and at t = 10.5 (b and C) (Modeling of wheel–soil interaction over rough terrain using the discrete element method, Smith, W. and H. Peng, Journal of Terramechanics, 2013. 50(5–6): p. 277-287, used with permission of Elsevier)

2.4.2.4. Conclusion of Discrete (Distinct) Element Method (DEM) Models

This method was initially developed for studying mechanics of granular material, which could be used instead of the continuum theorem. Although discrete element methods are still in their development stages, their effectiveness in areas such as lightweight robotic wheels interaction with granular soil was shown. However, there are some shortcomings associated with the current DEM models such as high computational requirements, consideration of simplified shapes for soil particles, non-corresponding size of the particles compared to actual soil grains, lack of robust parameterization procedures for model inputs, and underestimated number of particles due to computational constraints.

2.4.3. Finite Element Methods (FEM)

Mechanical behavior of the terrain depends on many aspects such as grain shape, water content, cohesion, and vegetation, etc. Identifying all of these parameters and correlating them to the vehicle performance using empirical closed form formulations are limited to the similar test conditions. On the other hand, using the simple physics based methods to model the terrain

can lead to significant errors in both estimating model input parameters and capturing terrain mechanics. This will ultimately cause the vehicle response to deviate from experimental data. One alternative numerical method for analyzing vehicle performance is the finite element method. Thanks to the fast rate of computational power improvements, and advancements in developing more sophisticated material models, FEM has become one of the practical tools for analysis of the complex systems [51, 52].

Numerous researchers have utilized FEM to model soil structure and soil-tool interaction. Abo-Elnor performed a FEA analysis that involved dynamic three dimensional soil-tool interactions [53]. He developed a hyperplastic constitutive model to show the monotonic behavior of the sand during loading at different speeds and accelerations. This model, which is based on the predefined failure surfaces, considers the dynamic behavior of the soil, and can be used for simulating the shearing effect in tire-soil interaction. In the following sections, the important FEM models in the field of wheeled vehicle terramechanics are described in a chronological order.

2.4.3.1. R. N. Yong and E. A. Fattah Model

The Yong and Fattah are from the early authors who studied the performance of the tire on soil using FEM [54, 55]. For representing the soil, they assumed the soil in plain stress, and included the stress-strain relationship with yield criteria in the terrain material model. However, tire is assumed as a semi-flexible ring with plane strain, and experimental boundary conditions are applied at the tire-soil interface. The applied boundary conditions are simplified soil stratum, tire-soil contact area, and stress distribution over the contact area [56]. These conditions are studied experimentally in separate studies, and assumed to be function of axial load, input torque, translational velocity and slip [57]. The resulted measurements are

formulated and assigned as nodal forces in every step of the simulation. Finally, tire soil performance factors such as drawbar pull, tire resistance and soil profile are evaluated against experimental data.

2.4.3.2. U.S. Army's Cold Regions Research and Engineering Lab. (CRREL)

This finite element model initially was developed for snow by the U.S. Army Corps of Engineers [58]. However, in the past few years it has been expanded to include other types of terrains such as sand. The process of tire-terrain modeling is divided into three main areas including terrain material modeling, tire modeling, and tire-terrain interface development. The developed terrain material models are a crushable foam model and a Drucker-Prager plasticity model with cap hardening. The parameterization of the material models is done using the plate sinkage test data from filed and lab in addition to literature data for similar terrains. The four tire models that are developed in this study include: (1) rigid tire model, (2) a simplified model similar to Darnell model [59], (3) modal analysis tire model with smooth tread (4) modal analysis tire model with straight ribbed tread.

The rigid tire model is used for very soft deformable terrains like snow. In the second model, the tire is divided into three major sections: tread, sidewall, and shoulder. Then, material properties are measured for these composite segments rather than their individual components. The tire tread structure is modeled using the shell elements and the tire sidewall is divided into ten equal-length, non-extensible beam elements which their force-displacement characteristics are described by a lookup table. The third model is a smooth tread tire model which uses four-node, reduced integration shell elements for the carcass, and linear, hybrid continuum elements for the tread cap. This model was initially constructed for tire vibration modal analysis. Based on this model, the straight ribbed tread model is developed by eliminating the segments of the

tread continuum elements.

Using the developed tire and terrain models, three case studies are conducted including rigid tire on fresh snow, Shoop-Darnell tire model on soil, and modal analysis tire models on snow. The comparison of the model results with experimental data shows a good agreement for spindles forces, and underestimation for tire sinkage. The author, in her later studies, compared the same mobility factors with the predications of NATO Reference Mobility Model (NRMM) and reports a similar trend [60]. Furthermore, it is shown that the assumption of rigid tire for soft deformable terrains such as deep fresh snow is valid with a reasonable accuracy.

2.4.4. Summary Tables

Table 5: Summary of the features for physics based terramechanics models

First author (or model name if available)	Year	Application		Condition	Modeling approach		Comp. effort	Parameterization	Advancement	Ref.
		Tire	Terrain		Tire	Terrain				
VTIM	2012	Truck tires	Semi-definite, nonhomogeneous soil	Steady-state	3D lumped mass	Analytical soil mechanics	Real-time	Trial and error	Combining 3D tire model with analytical soil mechanics in a real-time GPU accelerated framework	[29]
Nakashima	2004	Elastic tire	Granular soil	Steady-state	2D FEM	DEM for soil upper layer, and FEM for lower layer	High	Trial and error	Applying dimensional analysis to the test data	[37]
Wakui	2010	Smooth and lugged tires	Granular sand with irregular shape	Steady-state, dynamic	3D lumped mass	3D DEM for upper soil layer, nonlinear spring-damper for lower layer	High	Based on previous studies [44, 61]	Including soil elastic plastic behavior, and grain shape	[42, 43]
Smith	2013	Small unmanned small vehicle wheel	Dry and lunar regolith simulant	Steady-state, dynamic	3D solid ring and solid cylinder	3D DEM	High	Based on experimental data from [48-50]	Including Hertzian forces, cohesion forces, soil packing, and surface roughness	[45]
Yong	1978	Two buffed tires and one treaded tire	Sand-clay mix, and kaolinite clay	Steady-state	2D FEM rigid ring (plane strain)	2D FEM (plain stress)	Medium	Laboratory test	Incorporating load B.C. including contact area distortion due to slip, surface roughness factor, and pressure distribution	[54, 55]
CRREL	2001	Light truck	Snow (mainly), soil	Steady-state, dynamic	Solid ring, FEM smooth shell model, and FEM shell model with continuum elements for tread	3D FEM	High	Indoor tests (tire), outdoor tests (snow)	New material model for snow, modal analysis of tire on snow, and extensive model validation	[58]

Fervers	2004	14.00 R 20 MIL	Wet loam and dry sand	Steady-state	2D FEM	2D FEM with Drucker–Prager with cap plasticity	High	Indoor test (tire),	Developing air filled 2D tire model	[62, 63]
Grujicic	2009	Modern radial tire	Saturated sand and dry sand	Steady-state, dynamic	Eight-node solid elements for tread, carcass, and sidewall. Rebar elements for belts	Eight-node elements with reduced integration and hourglassing control	High	Tire data from [64], and sand data from [65]	Combination of FEM results with Pacejka magic formula to generate an off-road interaction model for vehicle simulations	[66]
Xia	2010	Arbitrary	Arbitrary	Steady-state, dynamic	Finite strain hyper elastic model	3D FEM with Drucker–Prager Cap model	High	Not mentioned	Modeling soil top layer as elastic-plastic material with cap hardening, and bottom layer as elastic	[67]
Li	2013	Steel-belted radial truck tire	Soil	Steady-state, dynamic	FEM neo-Hookean for rubber materials, and rebar elements for belts	3D FEM with Drucker–Prager Cap model	High	Tire data from [68-70], and soil data from [71]	Experimental pressure measurements using 3D kinetic scanner, and good experimental validation	[72]

Table 6: Summary of the verified output results for physics based models

First author (model name if available)	Pressure-sinkage	Drawbar pull	Lateral force	Combined slip	Aligning moment	Bulldozing force	Multi-pass effect	Pressure distribution	Experimental validation	Additional outputs
VTIM	✓	×	×	×	×	×	×	×	×	Total energy for performing soil plastic deformation
Nakashima	✓	×	×	×	×	×	×	×	×	-
Wakui	✓	✓	✓	✓	×	×	✓	×	×	-
Smith	✓	✓	×	×	×	×	×	×	✓	Driving torque for terrain perturbation with different amplitudes and frequencies
Yong	×	✓	×	×	×	×	×	✓	✓	Soil deformation energy contours, soil strain and velocity fields, deformation energy contours
CRREL	✓	✓	✓	✓	×	×	×	✓	✓	Variation in snow density, tire contact area, tire deflection
Fervers	✓	×	×	×	×	×	×	✓	×	Cleat test enveloping curve, compaction pressure for different soils
Grujicic	✓	✓	✓	×	×	×	×	✓	✓	Contact area, braking torque, motion resistance
Xia	✓	✓	✓	×	×	×	×	✓	×	Contact area, slip-sinkage, traveling distance before stuck, compaction density, volumetric plastic strain
Li	✓	✓	✓	×	×	×	×	✓	✓	Dynamic vertical load

2.5. Semi-Empirical Models

A broad range of tire-terrain interaction models fall into this category. These models combine experimental measurements, empirical formulations, and analytical methods to capture the tire-terrain interaction. Using such a hybrid approach reduces the computational effort, and simultaneously makes it possible to conduct simulation case studies [73-76]. This makes the semi-empirical tire models good candidates for full vehicle simulations and control applications. The majority of the models in this field use the two-dimensional empirical formulation developed by Bekker and Wong [28, 77-83]. In these formulations, the normal and shear stresses, in the tire contact patch, are expressed as the functions of the tire kinetics and kinematic variables. Consequently, the corresponding stress components are integrated over the contact patch to calculate the spindle forces, tire sinkage, soil deformation, tire deflection, etc.

The pressure-sinkage relationship for most of the mineral terrains is specified by following equation, which is equivalent to the soil pressure p under a circular plate with the smaller radius b, and at the depth z under the soil surface.

$$p = (k_c / b + k_\phi) z^n = k_{eqq} z^n \tag{12}$$

The coefficients n, k_c, and k_j are obtained by curve fitting to the pressure-sinkage experimental data. This equation is modified by Wong to include the terrain response during an unloading-reloading cycle:

$$p = \left(k_c / b + k_\phi\right) z_u^n - k_u \left(z_u - z\right) = p_u - k_u \left(z_u - z\right) \tag{13}$$

Where p_u, z_u, and k_u are the initial pressure, sinkage, and slope of the pressure-sinkage curve, respectively, at the beginning of the unloading phase. Similar to the terrain normal stress, the shear stress-displacement trend differs by changing the terrain type. The mineral terrains in

which shear stress increases with the shear displacement until it reaches a maximum value, without having a peak, the shear stress-displacement relationship can be shown as:

$$s/s_{\max} = 1 - \exp(-j/K) \tag{14}$$

Where s, $s_{\max}$, and j are shear stress, maximum shear stress, and shear displacement, respectively. Additionally, K is an empirical constant, which is called shear deformation parameter. For terrains such as muskegs, shear-displacement reaches a peak and then drops. This behavior can be captured using the following equation:

$$s/s_{\max} = (j/K_w)\exp(1 - j/K) \tag{15}$$

For snow covered terrains, the shear curve reaches to a peak and then decreases to a constant value. This behavior is shown in the following equation:

$$s/s_{\max} = K_r\left[1 + \left[1/K_r\,(1 - 1/e) - 1\right]\exp(1 - j/K_w)\right]\left[1 - \exp(-j/K_w)\right] \tag{16}$$

The maximum shear stress $s_{\max}$ in above equations can be described by the Mohr-Coulomb equation:

$$s_{\max} = c + p\tan\phi \tag{17}$$

Where parameter c is the soil cohesion, and j is the soil angel internal friction. The experimental values for the parameters introduced in the aforementioned equations can be found in the literature [84]. In recent years, new advancements have emerged in modeling of the tire-soil interaction that are mostly inspired by traditional Bekker's and Wong's formulations. In this chapter, models that have accomplished some major milestones in modeling the tire terrain interaction, performance analysis, and implementation are briefly described. At the end of the chapter, two tables are given that summarize the main features of the selected models as well as the performance aspects that have been investigated by each model.

2.5.1. NWVPM

The Nepean wheeled vehicle performance model (NWVPM) was developed by the Vehicle Systems Development Corporation in order to function as a computer-aided program for off-road parametric analysis of the wheeled vehicles [85]. Tire force characteristics including terrain resultant vertical reaction, motion resistance, and trust are calculated by integrating the radial normal stress and shear stress over the contact patch. The normal stress distribution in different contact patch sections, due to the terrain response to normal and repetitive loading, is characterized for various terrains such as mineral terrains, muskegs, and snow. Based on the tire deflection relative to the terrain sinkage, two models are considered for studying the tire-terrain interaction in rigid tire operating mode and elastic tire operating mode, as shown in Figure 10.

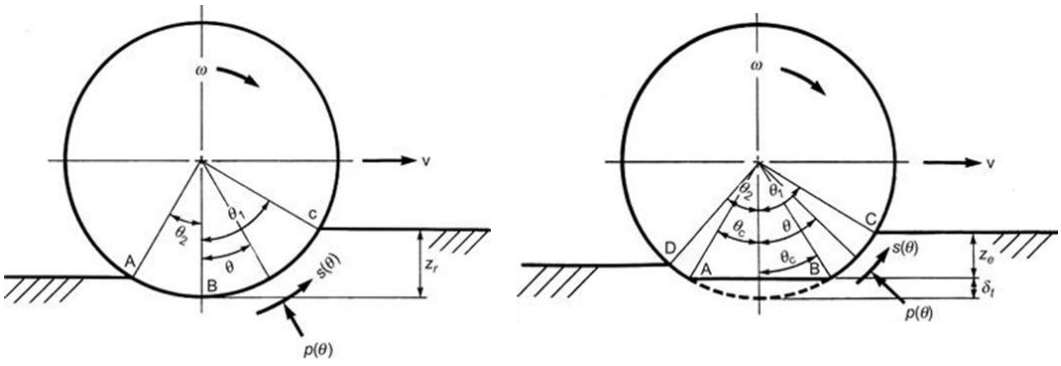

Figure 10: Tire-terrain interaction model. (a) Tire in solid operating condition (b) Tire in elastic operating condition (Terramechanics and Off-Road Vehicle Engineering: Terrain Behaviour, Off=Road Vehicle Performance and Design, Wong, J.Y., 2nd Edition ed. 2010, Amsterdam, Netherlands, used with the permission of Elsevier)

The shear displacement at the circular part of the contact patch (AB and BC in rigid mode, and BC and AD in elastic mode) is calculated using:

$$j = \int_0^t V_j dt = \int_0^{\theta_1} [1-(1-i)\cos\theta] d\theta = r[(\theta_1 - \theta) - (1-i)(\sin\theta_1 - \sin\theta)] \tag{18}$$

Where θ_1 is the entry angle of the point that comes into the ground contact initially. It should be noted that for the flat portion of the tire contact patch AB in elastic operating condition, slip

velocity is considered to be constant. Therefore, the shear displacement is linearly proportional to the tire slip and displacement from point B. The calculated performance factors for rigid ring and elastic operating modes are shown in Table 7. In the formulas that are mentioned in Table 7, b_{ti} is the tire width, D is the deflected tire diameter, θ_1 is the front contact angle, θ_2 is the front contact angle, p_g is the average ground pressure, and θ_c is the contact angle for half of the flat section.

The effect of the tire lug is considered in the model by decoupling the ground pressure acting on the lugs and that acting on the carcass, and calculating the equivalent ground pressure. For validation, the model results for the tractive performance of a lunar vehicle from Apollo program is compared to experimental data measured by WES.

Table 7: Model performance parameters in different operating conditions

	Rigid operating mode	Elastic operating mode
Vertical force	$W = \frac{b_{ti}D}{2}\left\{\begin{array}{l}\int_0^{\theta 1}[p(\theta)\cos\theta + s(\theta)\sin\theta]d\theta \\ +\int_0^{\theta_2}[p(\theta)\cos\theta - s(\theta)\sin\theta]d\theta\end{array}\right\}$	$W = \frac{b_{ti}D}{2}\left\{\begin{array}{l}\int_{\theta_c}^{\theta 1}[p(\theta)\cos\theta + s(\theta)\sin\theta]d\theta \\ +\int_{\theta_c}^{\theta_2}[p(\theta)\cos\theta - s(\theta)\sin\theta]d\theta\end{array}\right\} + b_{ti}Dp_g\sin\theta_c$
Motion resistance	$R_t = \frac{b_{ti}D}{2}\left\{\int_0^{\theta_1} p(\theta)\sin\theta d\theta - \int_0^{\theta_2} p(\theta)\sin\theta d\theta\right\}$	$R_t = \frac{b_{ti}D}{2}\left\{\int_{\theta_c}^{\theta_1} p(\theta)\sin\theta d\theta - \int_{\theta_c}^{\theta_2} p(\theta)\sin\theta d\theta\right\}$
Thrust	$F = \frac{b_{ti}D}{2}\left\{\int_0^{\theta_1} s(\theta)\cos\theta d\theta + \int_0^{\theta_2} s(\theta)\cos\theta d\theta\right\}$	$F = \frac{b_{ti}D}{2}\left\{\int_{\theta_c}^{\theta_1} s(\theta)\cos\theta d\theta + \int_{\theta_c}^{\theta_2} s(\theta)\cos\theta d\theta\right\} + b_{ti}\int_0^{l_{AB}} s(\theta)dx$
Applied torque	$M = \frac{b_{ti}D^2}{4}\left\{\int_0^{\theta_1} s(\theta)d\theta + \int_0^{\theta_2} s(\theta)d\theta\right\}$	$M = \frac{b_{ti}D^2}{4}\left\{\int_{\theta_c}^{\theta_1} s(\theta)d\theta + \int_{\theta_c}^{\theta_2} s(\theta)d\theta\right\} + \frac{b_{ti}D\cos\theta_c}{2}\int_0^{l_{AB}} s(\theta)dx$

2.5.2. B. Chan and C. Sandu Model

Chan and Sandu from Advanced Vehicle Dynamics Laboratory at Virginia Tech (AVDL) developed a semi-empirical tire model in an effort to further include some aspects that other tire models fail to include [86-89]. The soil surface in this model is developed using the plasticity theory derived from the strip load analysis. Therefore, the model is able to predict sinkage based on the normal pressure distribution of the contact patch. This is accomplished by using Bekker's semi-empirical approach [80]. Moreover, this model includes the effects of bulldozing. The model can also predict the response of the tire based on the combined longitudinal and lateral slip. As such, the model changes to pure longitudinal if the slip angle are zero, and consequently, to pure lateral if the slip ratio is zero. Furthermore, this is a three dimensional model, which outputs all the forces and moments at the contact patch while inputting the normal load, the slip ratio, slip angle and the camber angle. Thus, the parameterization of this model is relatively simple.

The model is valid for both rigid wheels and flexible tires. The rigid wheel model is developed based on the work done by Wong and Reece [28]. Then, the tire model has been extended to the flexible tire, which used the flexible ring on elastic foundation pictured in Figure 11 to provide a connection between analytical modeling and experimental characteristics of tire and soft soil interaction [90]. As it was previously mentioned, this off-road tire model can predict the pressure-sinkage relationship, shear stress along the tire contact patch, drawbar pull, driving torque, and lateral force, which takes the bulldozing and multi-pass effects into account.

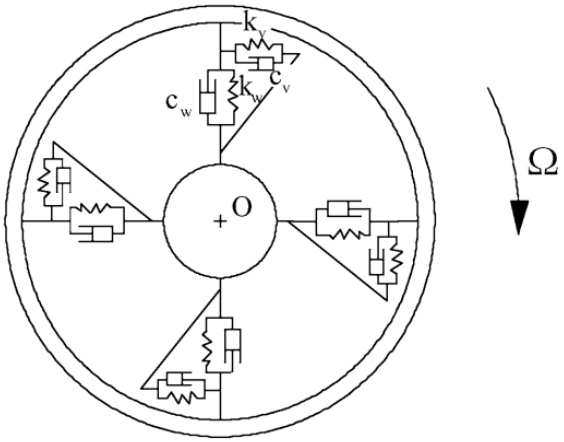

Figure 11: Tire structure modeling using flexible ring (A Simple Analysis Method for Contact Deformation of Rolling Tire. Vehicle System Dynamics, Yu, Z.-X., et al., 2001. 36(6): p. 435-443, used with the permission of Taylor & Francis)

In order to estimate the normal stress distribution along the contact patch, the pressure-sinkage relationship is needed. The pressure-sinkage relationship can be expressed by a semi-empirical formula originally introduced by Bekker and later modified by Reece, which is known as the Bekker-Reece equation [91]:

$$\sigma_n = \left(ck_c^{'} + b\gamma_s k_\phi^{'}\right)\left(\frac{z}{b}\right)^n \tag{19}$$

Where $k_c^{'}$ and $k_\phi^{'}$ are the sinkage index and constants, respectively, which are obtained from experimental data by using a bevameter or a penetrometer, and γ is the soil density. A diagram of how the pressure-sinkage relationship is calculated can be observed in Figure 12. It should be mentioned that the stress calculated at any sinkage by this formula is considered to act along the radial direction of the tire. Also, this formulation is valid for a homogeneous and isotopic terrain.

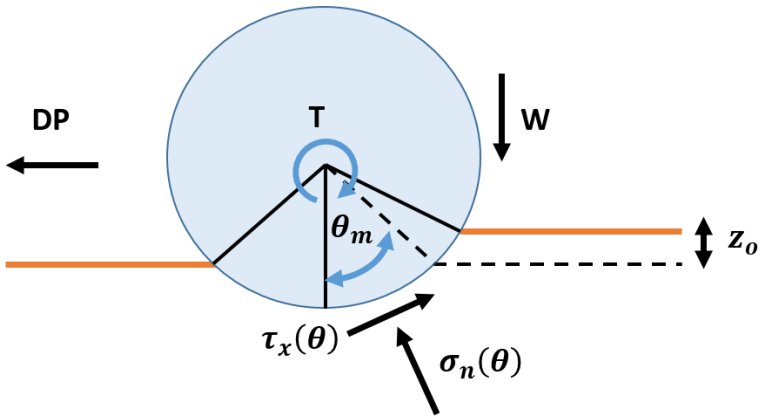

Figure 12: Resultants forces to tire due to ground stresses

The shear stress along the contact patch is expressed as an empirical equation first introduced by Janosi and Hanamoto [92]:

$$\tau_x = \tau_{\max}\left(1-e^{-\frac{j_x}{K_x}}\right), \tau_y = \tau_{\max}\left(1-e^{-\frac{j_y}{K_y}}\right) \tag{20}$$

Where $\tau_{\max}$ is the limiting shear stress that can be related to the normal stress through the Mohr-Coulomb equation as:

$$\tau_{\max} = c + \sigma_n \tan\phi \tag{21}$$

Also, j_x and j_y are the shear displacement in longitudinal and lateral directions respectively:

$$j_x(\theta) = \int_{\theta}^{\theta_e} R_{eff}(\theta)\left[1-(1-s_d)\cos\theta\right]d\theta \tag{22}$$

$$j_y(\theta) = R_{eff}(\theta)(1-s_d)(\theta_e-\theta)\tan\alpha_c \tag{23}$$

This model lacks some features that are vital to the accurate prediction of off-road traction and mobility [93]. The first drawback is that this model was developed for quasi-steady state situations; thus, the maneuvers that can be performed are limited. Furthermore, the model can't account for the tire detaching the surface, which is essential in case of irregularities. However, the biggest drawback of this model is that it has still not been validated against experimental data. The

validation has been performed on this model through the use of commercial on-road software CarSim® [94, 95].

2.5.3. VDANL

The Vehicle Dynamic Analysis, Non-linear (VDANL) is a vehicle dynamic simulation model developed by Systems Technologies Inc. for National Highway Administration [96]. This model is based on a semi-empirical approach that combines the soil mechanics theories with curve-fitted soil data in order to capture mobility factors such as soil compaction, soil shear deformation, and soil passive failure. The strategy for calculating the tire sinkage is identical to Bekker's method, which considers the tire as a solid ring. This implies that, the model will be accurate when the tire pressure is sufficiently high and terrain is relatively soft. For the longitudinal tire-terrain interaction, the following equation is used to determine the compaction resistance due to tire sinkage:

$$R = b_{tr}.\frac{z_r^{n+1}}{n+1}.(\frac{k_c}{b}+k_\phi) \tag{24}$$

where b_{tr} is the width of the tire, b is the small dimension of the projected contact patch of the tire. The tire lateral force during cornering is calculated by adding the lateral force due to soil shear deformation and soil bulldozing force. The soil shear stress-strain relationship is considered to have an exponential form analogous to Metz's [27] formulation, that its required coefficients are derived from the literature. Additionally, the soil cutting theory is used for expressing the bulldozing force, which has relatively significant values in maneuvers with significant tire sinkage. This theory uses the Mohr's circle techniques to determine the passive earth pressure, which brings the soil in front of the tire into a state of passive failure. The soil cutting force can be calculated by integrating the passive earth pressure over the tire sidewall at a given tire contact area A_s, and

slip angle α. The decomposition of this force normal to the direction of the tire mid-plane results in the bulldozing force:

$$F_c = F_p \cdot \sin\alpha = \int^{A_s} \sigma_p \cdot \sin\alpha \tag{25}$$

Where

$$\sigma_p = \gamma_s z N_\phi + 2c\sqrt{N_\phi} \tag{26}$$

In this equation, γ is the soil unit weight, Z is the tire sinkage, and $45+\phi/2$ is the angle of failure plane. For model verification, bulldozing force at different slip values is compared with the experimental data reported by Toffersen [97]. Moreover, the dynamic response of the tire in a full vehicle simulation is evaluated in multiple case studies such as straight-line full-throttle acceleration, straight-line braking, and fishhook maneuver.

2.5.4. AS2TM

The AESCO Soft Soil Tire Model (AS2TM) [98] is a semi-empirical off-road tire model that was built for the MATLAB/Simulink environment based on a research conducted by Schmid at IKK [99, 100]. This model runs approximately real time, and it is mostly used for vehicle dynamics simulations to predict traction and mobility. The Bekker's method is used to account for the vertical and horizontal deformations in the tire-soil interaction. AS2TM assumes the tire-terrain interaction as a two-dimensional single point contact, and encompasses both a rigid wheel and a flexible wheel approximation depending on the terrain that will be used. The elastic tire model uses a larger substitute circle to describe the deformed contact patch between the tire and soil, where the diameter of the substitute circle is calculated from the equilibrium between the vertical reaction force of the soil and the applied force from the tire (wheel load). This principle can be observed in Figure 13. It should be noted that the formula used to calculate the tire deflection is a

function of the tire inflation pressure, and is specified based on the tire manufacturer data.

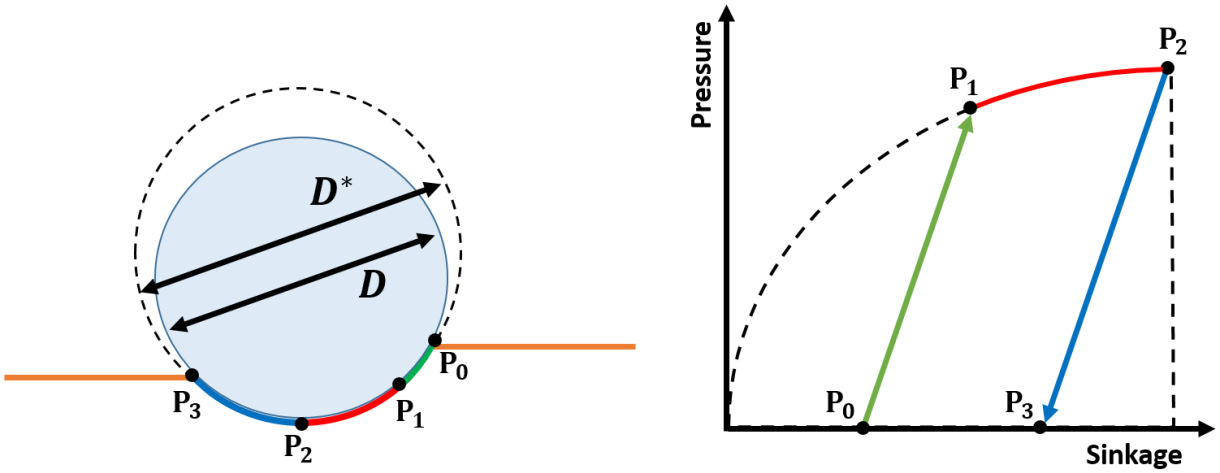

Figure 13: Using substitutive circle in order to account for flexible tire in tire-soil interaction

AS2TM predicts the pressure-sinkage relationship and the maximum shear stress using Bekker's equations. However, it takes into account both adhesion friction (μ_{ts}) and internal soil friction to calculate the maximum shear strength:

$$\tau_{\max} = \min\left(c + p\tan\phi, p\mu_{ts}\right) \tag{27}$$

Moreover, it uses Janosi and Hanamoto's approach to approximate the local shear stress. It also accounts for the multi-pass effect or repetitive loading of the soil using a description that is similar to that developed by Wong. In order to capture the soil plastic deformation, the track module in the model stores the vertical soil deformation and soil compaction of every loading so that it can be used for next loadings steps. Other important modeling aspects that are included tire rolling resistance effect due to slip sinkage, plastic soil deformation, and tire structure deformation.

The mathematical approach for calculating the lateral and longitudinal forces takes into account the combined longitudinal and lateral slip. This approach is based on the theories investigated by Schwanghart and Grecenko [101, 102]. In addition, the effect of the tire profile (lug height), is included by considering different pressure values and friction coefficients for the

positive and negative sections of the tire tread. However, it should be noted that lug shape is not considered in the model.

The AS2TM incorporates various soil parameters such as Bekker values for vertical soil strength (k_c, k_ϕ, and n), Coulomb parameters for horizontal soil strength (cohesion and angle of friction), tangent-module of the horizontal shear deformation, slippery coefficient for ice and wet grass, soil damping coefficient (linear), soil density, soil elasticity, and correction factors for compaction capacity and rolling resistance. The model can simulate the tire behavior in both steady-state and dynamic transient conditions. The dynamic behavior of the tire is captured by including the soil damping and the contact pressure variations due to the tire impetus effect.

2.5.5. SCM

The Soil Contact Model (SCM) is a three-dimensional semi-empirical terramechanics model developed based on the Bekker's theory [103, 104]. This model is computationally optimized to function as a module in the multi-body dynamic software (MBS) simulations. The tire is considered as a solid object, and its geometry is described using three-dimensional polygonal mesh, which is widely used in computer graphics and CAD. The soil is discretized into uniformly spaced columns, which their elevation represents the corresponding soil height, as seen in Figure 14. The contact detection algorithm uses the Spatial Binning and Z-Buffering methods to map the tire model vertices into the soil mesh, and find the tire's discrete contact patch.

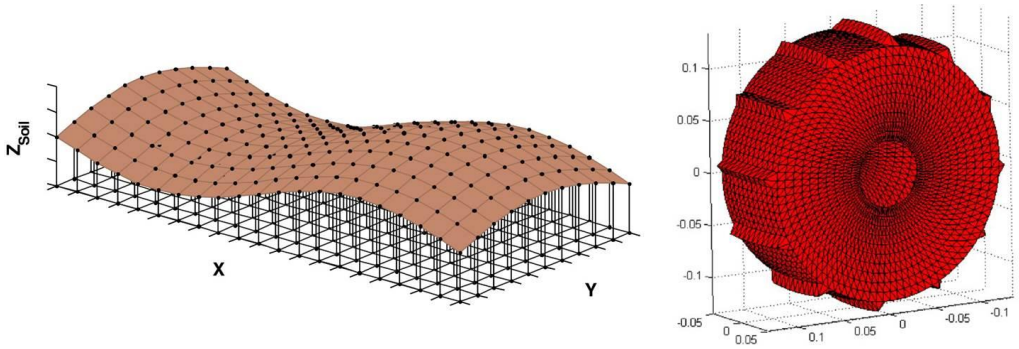

Figure 14: Geometry definition of contacting surfaces. Left: Soil topology. Right: surface geometry of contact body (Soft Soil Contact Modeling Technique for Multi-Body System Simulation, Krenn, R. and A. Gibbesch, Trends in Computational Contact Mechanics, 2011. 58: p. 135–155, used with the permission of Springer).

The contact forces and moments between the tire and soil are calculated as the functions of the contact parameters (contact patch area, surface gradient, and sinkage) and relative kinematics (penetration velocity and sliding velocity). Then, the plastic soil deformation calculation is carried out in three stages. In the first stage, soil displacements in horizontal, and vertical directions are calculated based on the local footprint depth and contact velocity. The second stage is conducted by initially banking up the displaced soil at the border of the footprint based on the soil flow field at this area. Finally, in the third stage, an iterative erosion algorithm is applied to smooth the soil around the contact patch. For verification, the force-sinkage results of the SCM are compared with the Bekker's model. Additionally, the model is implemented as a MBS library module to study the mobility of a planetary rover in a visual simulation.

2.5.6. FTire (Flexible Ring Tire Model)

The FTire Model family is comprised of three tire models: Flexible Ring Tire Model (FTire), Rigid Ring Tire Model (RTire), and the Finite Element Tire Model (FETire) [1]. The RTire model is a real-time model that is used for "test-rig simulations of the standing or slowly rolling tire." On the other hand, the FETire model is a really detailed finite element model [105]. Finally, the FTire model is probably the most widely used commercial tire model in the market. It is a time-domain,

spatial, nonlinear tire simulation model for high-frequency and short-wave-length excitations [8]. The model is really complex and it includes modules for tread-wear, distributed thermal modules, thread pattern geometry, and parameterization assistant.

FTire is developed as a three-dimensional vibrational model. It divides the tire circumference into multiple extensible and flexible ring elements, which has both in-plane and out-of-plane bending stiffnesses, as it can be seen in Figure 15. These belt elements are elastically suspended on the rim with the stiffness and damping elements in radial, tangential, and lateral directions, as shown in Figure 16. In this model $k_{friction}$ represents the stick-slip friction element between the tire and the rim. Using this setup, the in-plane and out-of-plane tire motions are possible. A user-defined number of tread blocks are attached to every belt element, using nonlinear spring and dampers in radial, tangential, and lateral directions. The required values for the spring stiffness and damping are specified in advance by a preprocessing module, which incorporates the static, dynamic, and modal analysis test data [106].

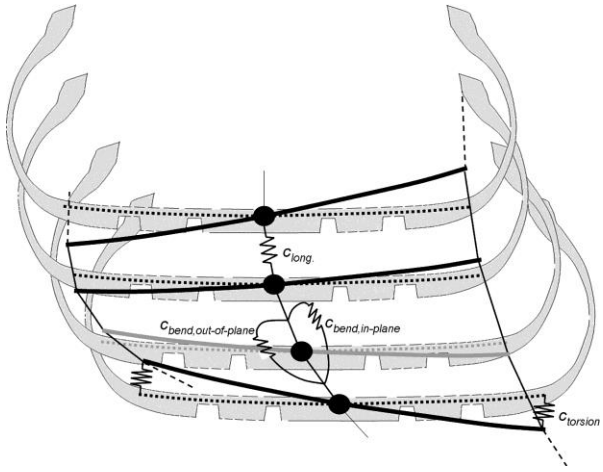

Figure 15: Force elements between adjacent belt segments (FTire – the tire simulation model for all applications related to vehicle dynamics. Vehicle System Dynamics, Gipser, M., Vehicle System Dynamics, 2007. 45(sup1): p. 139-151, used with permission of Taylor & Francis)

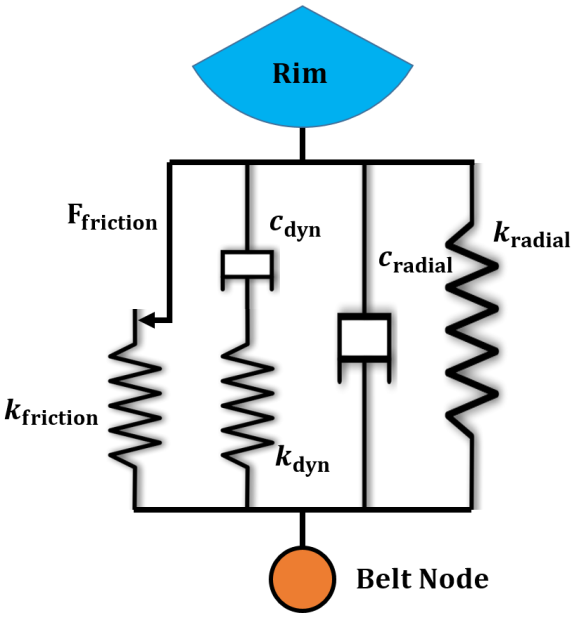

Figure 16: Force elements between a single belt node and rim

The forces and moments from the tire-road interaction are computed by integrating the nodal forces in the elastic foundation of the belt. FTire uses a high accuracy implicit solver, which can cooperate with MBS software like ADAMS. This makes it possible to study the high frequency simulations such as ABS braking and extremely uneven road perturbations. For soil modeling, the available regular grid roads (RGR) are enhanced with a simple place-holder technique [107], which considers the following relation for pressure-sinkage dependency:

$$F_d(\dot{z}) + k(z_0 - z) + p_{cont} = 0 \tag{28}$$

Where F_d is the nonlinear damping term, k is ground stiffness, z_0 is the unreformed surface height, z is the deformed surface height, and p_{cont} is the local contact pressure. It should be noted that, a large slope value is considered for the positive part of the damping term vs. penetration rate curve, which guarantees a persistent soil compaction, as seen in Figure 17.

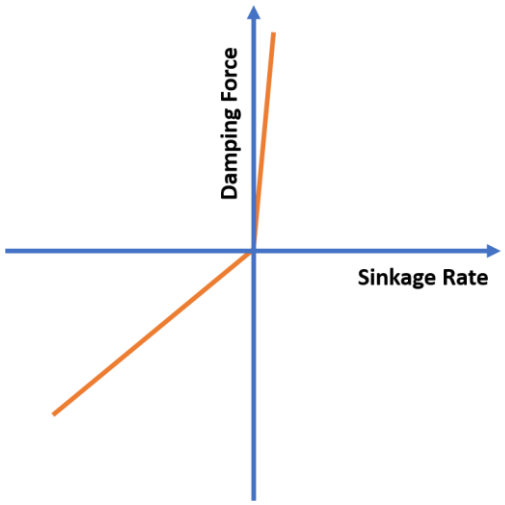

Figure 17: Non-Linear Damping Characteristic in Soft-Soil Placeholder Model

2.5.7. HSSTM Tire Model

The original goal of this project was to develop an accurate and efficient off-road tire model for soft soil that will interface with commercial multi-body dynamics software. The model will predict drawbar pull on soft soil, longitudinal and lateral forces, accounting for the combined slip in the contact patch, the sinkage, and the bulldozing effect. At the preliminary phase of the project, a simplified lumped mass approach for modeling the tire structure was introduced by Pinto [108-110]. This approach considered the tire structure as three layers of lumped masses, in which lumped masses are connected to the rim and also to each other through a set of linear spring and dampers. This three-layer structure approach is an advanced version of a lumped mass single layer on-road tire model developed by Umsrithong [111-116]. In 2012 [117], a new method for modeling the tire was introduced, and a more systematic approach was used for developing the software. This new approach is elaborated in the following chapters.

2.5.8 Summary Tables

Table 8: Summary of the features for semi-empirical models

First author (or model name if available)	Year	Application		Condition	Modeling approach		Comp. effort	Parameterization	Advancement	Ref.
		Tire	Terrain		Tire	Terrain				
NWVPM	1980	Truck tires	Sand, clay, loam, snow	Steady-state	2D rigid ring with empirical modification for elastic tire	Empirical formulation	Low	Outdoor testing	Elastic tire mode, effect of tire lugs, and contact length	[85]
STINA	1996	Rigid wheel	Sand, clay, loam	Steady-state, dynamic	2D rigid ring, and parabola model of the elastic tire [99]	Empirical formulation	Low	Based on user defined characteristics maps	Interface to ADAMS, including penetration speed	[118, 119]
VDANL	2004	Rigid wheel	Dry sand, sandy loam	Steady-state, Dynamic	2D rigid ring	Empirical formulation combined with soil mechanics	Low	Literature [27, 44]	Implementation in VDANL	[96]
Chan and Sandu	2010	Rigid wheel	Dry sand, moist Yolo loam	Steady-state	2D rigid ring with empirical modification for elastic tire	Empirical formulation	Low	Literature [86, 120]	Interface to CarSim	[86-89, 94]
AS2TM	2005	User defined	User defined	Steady-state, dynamic	2D rigid ring with substitute circle for elastic tire	Empirical formulation with one point contact	Real time	Load-deflection curve for tire, and pressure sinkage and shear-displacement data for soil	More comprehensive ver. of NWVPM with TYDEX interface that considers tire profile, and soil dynamics	[98]
SCM	2008	Rigid planetary rover wheel	Soil simulant DLR-A and DLR-D	Steady-state, dynamic	3D rigid polygonal mesh	Empirical formulation, enhanced with a soil plastic deformation model	Medium	Literature [121]	Considering soil deposition and erosion around contact area	[103, 104]

FTire	2008	User defined	User defined	Steady-state, dynamic	3D flexible ring	3D terrain with a simple nonlinear damping model	High	Defined parameterization procedure for tire	Detailed tire model, and ground pressure distribution	[122]
HSSTM	2012	User defined	User defined	Steady-state, dynamic	3D lumped mass model	3D analytical and empirical terrain models	Medium	Defined parameterization procedure for tire, and empirical soil data from literature [44]	Comprehensive 3D tire model and tire-soil interaction model for on road and off-road applications including ground pressure distribution	[74, 76, 117]

Table 9: Summary of the verified output results for semi-empirical models

First author (model name if available)	Pressure-sinkage	Drawbar pull	Lateral force	Combined slip	Aligning moment	Bulldozing force	Multi-pass effect	Pressure distribution	Experimental validation	Additional outputs
NWVPM	✓	✓	×	×	×	×	✓	✓	✓	Tractive efficiency
STINA	✓	✓	×	×	×	×	✓	✓	×	Spindle acceleration
VDANL	✓	✓	✓	✓	×	✓	×	×	×	Compaction resistance
Chan and Sandu	✓	✓	✓	✓	×	×	✓	×	✓	Tractive efficiency
AS2TM	✓	✓	✓	✓	✓	×	✓	✓	✓	Rolling resistance, slip sinkage, soil compaction
SCM	✓	✓	✓	×	×	×	✓	✓	×	
FTire	✓	×	×	×	×	×	×	✓	×	Standstill steering maneuver, and dynamic tests on multiple uneven terrains
HSSTM	✓	✓	✓	✓	✓	✓	✓	✓	✓	Standstill steering maneuver, and dynamic tests on multiple uneven terrains, road data base for various ground geometries and obstacles, and advanced visualization module

2.6. Conclusion

In this literature survey, terramechanics simulation models, which investigated the performance of wheeled vehicles on deformable terrains, are reviewed. The models are grouped into three categories, namely: empirical tire methods, physics-based tire methods, and semi-empirical methods. Although the empirical models are good for simple mobility assessments, they cannot be extrapolated beyond the test data used to establish them. The physics-based models incorporate methods including computational physics and numerical analysis to construct an applied framework for the complex problem of soil-tire interaction. These models require high computational resources to handle their highly discretized structures. Additionally, most of the models in this group (except for very detailed FEM models) use simplified parameterization procedures to evaluate the material properties and simulation input parameters. Consequently, correlating the physics-based models results with the experimental data is challenging. On the other hand, semi-empirical methods employ empirical relations in addition to analytical approaches in order to achieve high fidelity results while keeping the computational effort and number of model variables low. Therefore, such models are considered good candidates to be incorporated in multibody dynamics models and vehicle simulations.

Chapter 3: Tire Materials Modeling

3.1. Introduction

A typical modern tire is manufactured from nearly 10-35 different components. Information about tire material properties, processing, mixing, assembly, and curing are almost always confidential, and cannot be received from tire companies. Furthermore, the material properties for the same tire from a manufacturer may vary, due to the vulcanization process, for example. In order to accurately estimate the behavior of the tire components, elaborate material models are needed. The parameterization of these models for each tire materials requires performing extensive experimental and analytical procedures, such as elastic and viscoelastic tests on individual tire sections. This level of details is required for calculating the accurate stress and strains in the tire structure, which would be helpful in tire design stage.

The main scope of this study is to estimate the tire mobility performance factors including forces and moments at the tire spindle, tire sinkage, and terrain deformation. Therefore, simplified methods are chosen for describing the tire materials behavior, such as hyperelasticity and viscoelasticity.

3.2. Hyperelasticity

A great portion of the tire structure consists of vulcanized elastomers, such as rubber material. Rubber has a nonlinear and incompressible behavior towards loading, which is independent of the strain rate. This behavior is known as hyperelasticity, and the material that shows this behavior is called green elastic material or hyperelastic. A hyperelastic material differs from an elastic material in four main aspects:

- The tire has a high stiffness in the initial step of loading, and extensively softens in the unloading phase. This phenomenon is known as Mullin's effect.
- Instead of having a hysteresis loop in the stress-strain curves of the loading cycle, the hyperelastic materials have a simple equilibrium curve.
- The hyperelastic materials exhibit different behavior in tension and compression. This is in contrast with the Hooke's law, which considers the stress to be proportional to strain. As a matter of fact, hyperelastic materials such as rubber, have a higher stress magnitude in compression when compared to the tension for an identical strain magnitude.
- Finally, a hyperelastic material has different modes of deformation that should be studied with respect to the given loading conditions. Each deformation mode requires corresponding constants in the material model that must be characterized experimentally. The choice of model constants and required parameterization tests should be done with care in order to avoid false analytical system response quantities that are not present in the experiments.

The hyperelasticity feature of the rubber should be enhanced with the viscoelasticity in order to precisely describe the rate-dependent loading/unloading force-deflection characteristics of the tire.

3.3. Viscoelasticity

Viscoelastic materials show a combined elastic and viscous rate-dependent behavior when experiencing deformation [117]. In elastic materials, once the applied stress or strain is removed, the specimen quickly returns to its initial condition. On the other hand, viscous materials exhibit a resistance toward the shear flow developed due to the applied stress or strain. In other words, upon

applying a constant strain, the material creeps. Similarly, by applying a constant stress, the strain increases and then eventually decreases with time.

The internal damping, rolling resistance, and thermal characteristics of a tire are associated with the viscoelastic property of the rubber. Therefore, in order to properly quantify the transient response of the tire, the viscoelastic material property should be incorporated. For small strains, the linear viscoelasticity assumption may be chosen. In this case, the relaxation rate of the material is proportional to the immediate stress, and the total viscoelastic behavior can be expressed using the superposition principle.

3.4. Modeling Procedure

There are different mechanical models that can describe the combined hyperelastic viscoelastic characteristics of a material. Each of the mechanical models considers a certain form of stress or strain response for the material under different loading conditions. The hyperelasticity of the tire is modeled by interpolating the tire load vs. deflection data in compression/tension loading/unloading scenarios. Using this approach allows us to define different loading stiffness for loading and unloading paths.

To include viscoelasticity, three main models can be considered which are Maxwell model, Kelvin-Voigt model, and Standard Linear Solid model [123]. For the Maxwell model, the viscoelasticity is modeled using a damping element (Newtonian dashpot) connected to a Hookean spring (stiffness element) in a series configuration. The force-deflection characteristics of this model are shown in Figure 18. In case of a step force input the deformation output of the model is shown in the top images. The bottom images show model force output during the deformation step input.

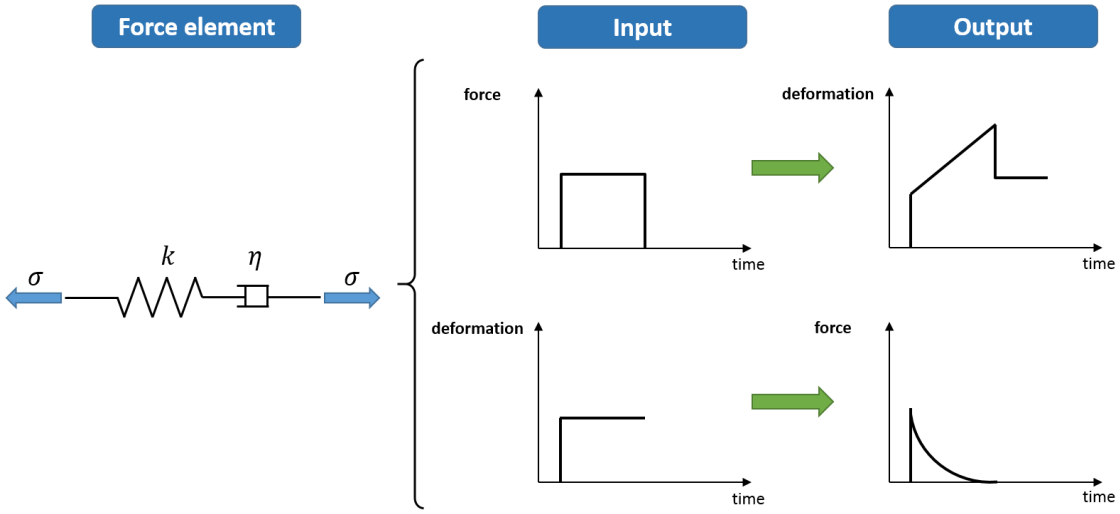

Figure 18: The force-deflection characteristics of the Maxwell model: (Top) deformation output during step force input (Bottom) force output during the step deformation input

The loading-deflection relation in axial direction can be modeled using the following formula:

$$k\sigma + \eta \frac{d\sigma}{dt} = k\eta \frac{d\varepsilon}{dt} \tag{29}$$

Where k is the axial stiffness, η is the damping stiffness, ε is the element strain, and σ is the applied stress. It should be noted that stress and strain of the element are analogous to the force and deflection. In the multi-axial loading the equation of motion is written as:

$$kS_{ij} + \eta \frac{dS_{ij}}{dt} = k\eta \frac{de_{ij}}{dt} \tag{30}$$

Where:

$$e_{ij} = \varepsilon_{ij} - \varepsilon_{kk}\delta_{ij} \tag{31}$$

$$\sigma_{ij} = S_{ij} + K\varepsilon_{kk}\delta_{ij} \tag{32}$$

K is the time-dependent bulk modulus, and S_{ij} is the element compliance. Considering the fact that the Maxwell model exhibits the unrestricted flow of material during loading, it isn't desirable

for the rubber element modeling. For the Kelvin-Voigt element, the stiffness and the damping elements are connected to each other in a parallel configuration. The force-deflection characteristics of this model for force step input and deflection step input are shown in Figure 19.

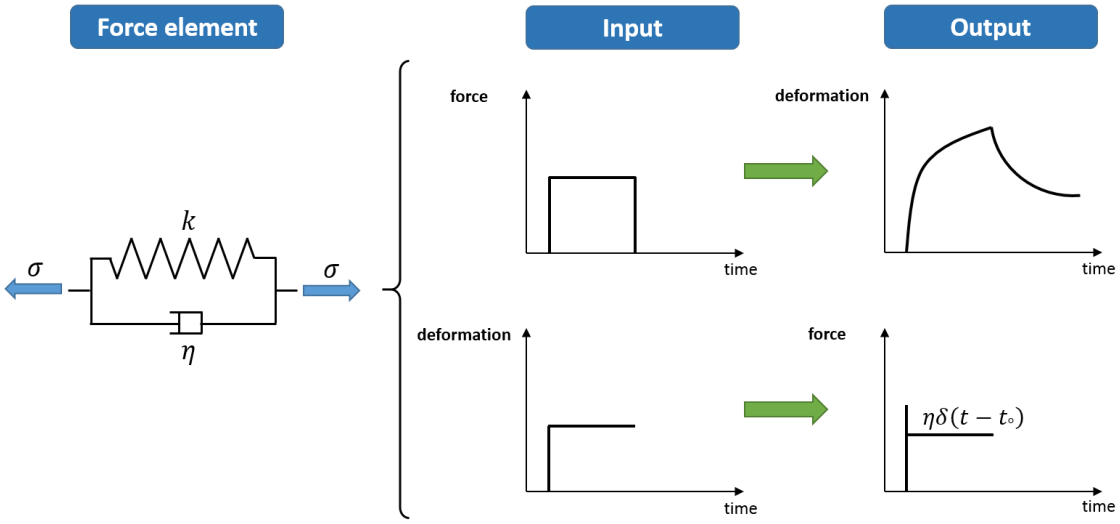

Figure 19: The force-deflection characteristics of the Kelvin-Voigt model: (Top) deformation output during step force input (Bottom) force output during the step deformation input

For this type of element, the force-deflection relation under axial loading has the following form:

$$\sigma = k\varepsilon + \eta\frac{d\varepsilon}{dt} \tag{33}$$

Where k is the axial stiffness, η is the damping stiffness, ε is the element strain, and σ is the applied stress. It should be noted that stress and strain of the element are analogous to the force and deflection. In the multi-axial loading the equation of motion is written as:

$$S_{ij} = Ke_{ij} + \eta\frac{de_{ij}}{dt} \tag{34}$$

K is the time-dependent bulk modulus, and S_{ij} is the element compliance. Another material model of interest is the Standard Linear Model (SLM), which is a Maxwell model that is connected to another stiffness element in a parallel configuration. The force-deflection characteristics of this model for force step input and deflection step input are shown in Figure 20.

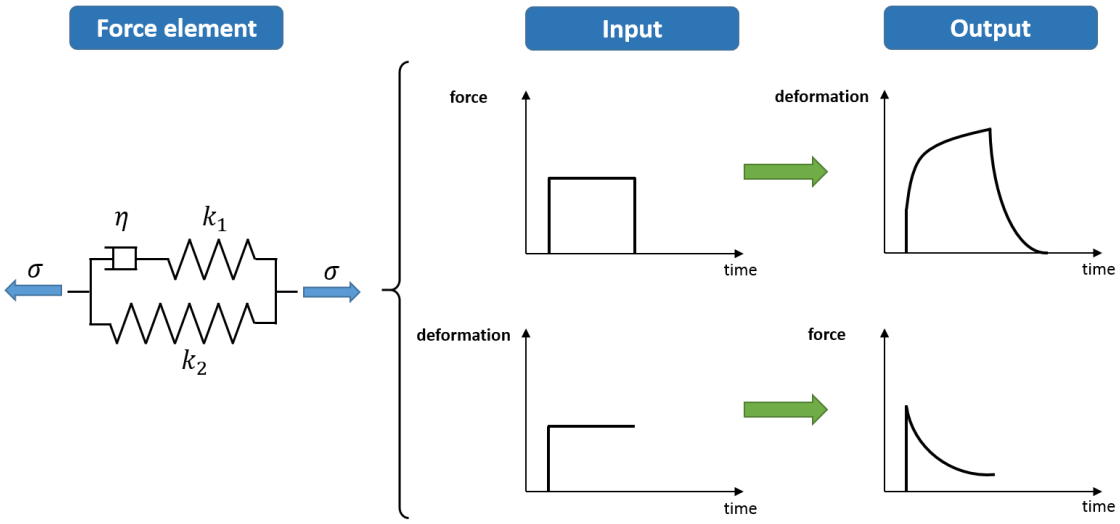

Figure 20: The force-deflection characteristics of the Standard Linear Solid model: (Top) deformation output during step force input (Bottom) force output during the step deformation input

These response characteristics in axial loading conditions can be captured using the following formula:

$$k_1 S_{ij} + \eta \frac{d\sigma}{dt} = k_1 k_2 \varepsilon + (k_1 + k_2)\eta \frac{d\varepsilon}{dt} \tag{35}$$

Similarly for multi-axial loading conditions:

$$k_1 S_{ij} + \eta \frac{dS_{ij}}{dt} = k_1 k_2 e_{ij} + (k_1 + k_2)\eta \frac{de_{ij}}{dt} \tag{36}$$

It is cumbersome to solve for the stress value in the Maxwell arm, since it contains both the stress and its derivative. Therefore, the Kevin-Voigt element is used as the main force element between tire/rim elements due to the fact that it is more accurate compare to the Maxwell model, and easier to solve for the stress values compare to the SLM.

3.5. Conclusion

In this chapter the material behavior of tire components was described via simplified material models. The main rubber mechanical properties that are included in the model are hyperelasticity and viscoelasticity. These mechanical properties were formulated using the Kevin-Voigt elements. This type of force element provides a superior accuracy compare to the other models while requiring less computational effort.

Chapter 4: Tire Structure Modeling

4.1. Introduction

As it was discussed earlier, a very detailed modeling of the tire structure is not required for studying the mobility of the tire. This is due to the fact that, for evaluating the tire performance, only forces and moments at the spindle and wheel sinkage are considered. Therefore, modeling the tire at a coarse level of tire structure discretization would be adequate and can result in a faster computational time. This feature is essential for full-vehicle simulations and control applications. The lumped parameter models reduce the DOFs in the model in favor of the computational effort, and consider the simplified material models in the respective directions. Such a method is used in HSSTM for representing the tire structure.

In the early phase of the project, a simplified lumped mass approach for modeling the tire structure was introduced by Pinto [108-110]. This approach considered the tire structure as three layers of lumped masses, in which the masses are connected to the rim and also to each other through a set of linear spring and dampers. This three-layer structure modeling approach is an advanced version of a lumped mass single layer on-road tire model developed by Umsrithong [111-116]. In 2012, an advanced method for modeling the tire was introduced [117], and a more systematic approach was used for developing the software. In this new approach, the tire belt is discretized circumferentially in multiple belt segments that are suspended on the rim using Kelvin-Voigt elements, which include variable stiffness and damping. These nonlinear elements capture the effect of the temperature and pressure changes on the tire mechanical characteristics through a set of empirical equations. Each belt segment is divided into a series of lumped masses connected to each other with in-plane and out-of-plane springs and dampers. The dynamics of these lumped masses, in addition to the wheel, is described in a state-space representation. The state is a set of

variables that, along with the time step, characterize the individual configuration of the system at any instance of time. The state variables are defined by equations of motion, and can be positions, velocities, acceleration, force, moment, torque, pressure, and etc. The state variables that are described using the differential equations are called state differential variables, and those that are defined directly from dynamic conditions, are called extra state variables. The standard notational convention for describing a state-space representation is as follows:

State equation: $\dot{q}(t)_{[N\times1]} = A(t)_{[N\times N]}q(t)_{[N\times1]} + B(t)_{[N\times M]}u(t)_{[M\times1]}$ (37)

Output equation: $v(t)_{[P\times1]} = C(t)_{[P\times N]}q(t)_{[N\times1]} + D(t)_{[P\times M]}u(t)_{[M\times1]}$ (38)

Where $q(t)$ is the state vector, $\dot{q}(t)$ is the derivative of the state vector, $A(t)$ is the state matrix, $B(t)$ is the input matrix, $C(t)$ is the output matrix, $D(t)$ is the direct transmission matrix, $u(t)$ is the input vector, $v(t)$ is the output vector, N is the number of states, M is the number of input variables, and P is the number of output variables. It should be noted that the input, output, and state vectors, as well as all the state-space representation matrices are time dependent. The choice of the state variables for different sections of the tire model is not unique, and would be discussed accordingly in the following sections. The type of mathematical model used to represent the tire structure is called a tire realization.

After discretizing the tire into smaller elements, we can express the dynamics of each element using a set of first order and second order differential equations. The second order differential equations can be rearranged as a set of first order ODEs. The complete set of the ODEs can be shown as follows:

$$\left\{\begin{array}{l} \dot{q}_1 = f_1(x_1,...,x_N,u_1,...,u_M,t) \\ \vdots \\ \dot{q}_N = f_N(x_1,...,x_N,u_1,...,u_M,t) \end{array}\right\} \tag{39}$$

$$\left\{\begin{array}{l} \dot{v}_1 = g_1(x_1,...,x_N,u_1,...,u_M,t) \\ \vdots \\ \dot{v}_N = g_N(x_1,...,x_N,u_1,...,u_M,t) \end{array}\right\} \tag{40}$$

Where $f_i(i=1,...,N)$, and $f_j(j=1,...,N)\,g_j\ (j=1\ldots P)$ include the following: (1) nonlinear functions of states and/or inputs, such as Sin and Cos functions, (2) terms with states and/or inputs appearing as powers of something other than 1 and 0, (3) terms with cross products of states and/or inputs. As a result, the multi-segments model that represents the tire characteristics is an autonomous (time-variant) non-linear system.

4.2. Coordinate System Convention

Before defining the state variables of the system, the coordinate systems for the sign convention must be defined. The definitions for the coordinate systems used in this study are similar to the Tyre Data Exchange format (TYDEX). TYDEX is a conventional interface between tire measurements and tire models developed and unified by an international tire working group to make the tire measurement data exchange easier. Additionally, TYDEX introduces an interface between the tire model and the simulation tool called Standard Tire Interface (STI), which would be described in details later on.

Along with the global reference frame, one additional right-hand orthogonal axis system used is the C-axis system (center axis system), as shown in Figure 21. The angles of rotation illustrated in this figure are: a positive slip angle α, a positive inclination angle γ, and a positive wheel rotation speed ω. The C-axis coordinate origin is mounted at the center of the wheel rim. The X_c axis is

in the central wheel plane and is parallel to the ground. The central wheel plane is constructed by decreasing the width of the wheel until it becomes a rigid disk with zero width. The Y_c axis is same as the spin axis of the wheel and rotates with the inclination angle γ. The Z_c axis is in the central plane of the wheel, point upwards, and turns with the inclination angle γ (camber).

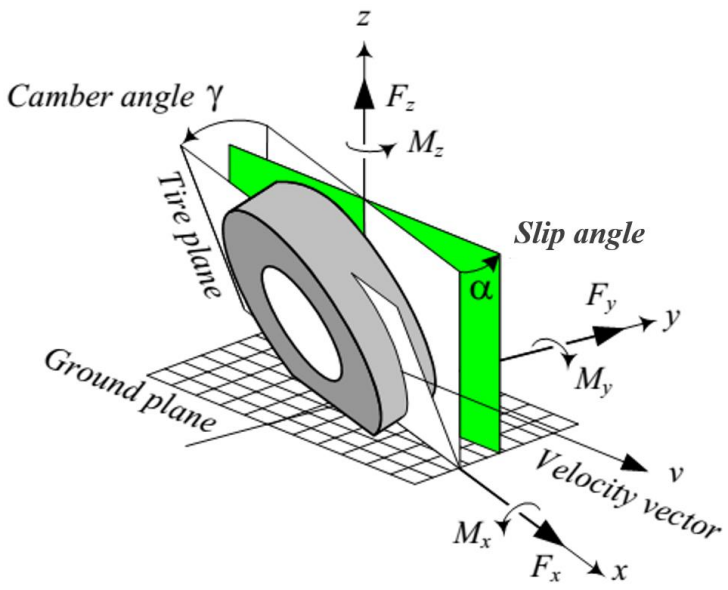

Figure 21: The representation of the C-axis coordinate system.

4.3. Wheel System

The rim kinematics can be described using six degrees of freedom (DOF) resulting in 12 state variables. Consider the position state vector of the wheel system as following:

$$ {}^{pos}_{rim}q = \begin{bmatrix} x_{rim} \\ y_{rim} \\ z_{rim} \\ \alpha_{rim} \\ \beta_{rim} \\ \delta_{rim} \end{bmatrix} \tag{41} $$

Where x_{rim}, y_{rim}, and z_{rim} are the translational coordinates of the wheel center in the global reference frame, α_{rim} is the wheel rotation angel around global X axis, β_{rim} is the wheel rotation angel around global Y axis, and δ_{rim} is the wheel rotation angel around Z axis. Furthermore, the velocity state vector of the wheel system is:

$$ {}^{vel}_{rim}q = \begin{bmatrix} \dot{x}_{rim} \\ \dot{y}_{rim} \\ \dot{z}_{rim} \\ \omega_x \\ \omega_y \\ \omega_z \end{bmatrix} \tag{42} $$

Where $\dot{x}_{rim}$, $\dot{y}_{rim}$, and $\dot{z}_{rim}$ are rim center translational velocities along global X, Y, and Z axes described in the global reference frame. Also ω_x, ω_y, and ω_z are rim center rotational velocities around global X, Y, and Z axes described in the global reference frame. Therefore, the final state vector of the wheel is given as:

$$ {}_{rim}q = \begin{bmatrix} {}^{pos}_{rim}q \\ {}^{vel}_{rim}q \end{bmatrix} \tag{43} $$

4.4. Tire Belt Model

If we discretize the tire belt circumference into N_{belt_seg} segments, the angle between the centers of each two segment will be:

$$ \Delta\theta_{seg} = \frac{2\pi}{N_{belt\_seg}} \tag{44} $$

Next, each segment is divided into N_{seg_elm} segment elements. The number of belt elements is assumed to be an odd number greater than three in order to always have at least one node at the middle of tire width and two neighboring nodes. Each segment element is actually a lumped mass with only translational DOF. Eliminating the rotational DOF from the belt segments helps reduce the computational effort of the model, while maintaining its accuracy. Consequently, the state vector for the segment elements is written as:

$$ {}_{seg}q = \begin{bmatrix} {}^{pos}_{seg}q_i \\ {}^{vel}_{seg}q_i \end{bmatrix} \qquad i = 1,...,N_{belt\_seg} \tag{45} $$

Where

$$ {}^{pos}_{seg}q_i = \begin{bmatrix} x_j \\ y_j \\ z_j \end{bmatrix}_i \qquad j = 1,...,N_{seg\_elm} \tag{46} $$

$$ {}^{vel}_{seg}q_i = \begin{bmatrix} \dot{x}_j \\ \dot{y}_j \\ \dot{z}_j \end{bmatrix}_i \qquad j = 1,...,N_{seg\_elm} \tag{47} $$

4.5. Pressure Effect

The general behavior of the tire depends substantially on tire inflation pressure. As the tire is loaded, its stiffness increases non-linearly. Meanwhile, there is a constant term in load-deflection curves of the tire mass elements due to the inner pressure force. The air pressure results in a directional force on each of the mass points. This force is calculated using the following formula:

$$ F_{pressure} = \frac{\pi \cdot r_{belt}}{n_{segments}} \cdot width_{tread} \cdot P_{actual} \tag{48} $$

Furthermore, to include the pressure change effects on the tire structure, the tire stiffness in the radial direction is updated at each time step based on the tire inflation pressure:

$$K_{\mathrm{mod}\,ified} = \left(a_1 + a_2 \cdot \frac{p_{actual}}{p_{measured}} \right) \cdot K_{measured} \tag{49}$$

Where a_1 and a_2 are constant terms, which are specified using the developed finite element tire model simulation results at different tire pressures. This procedure results in a look-up table, which is used for interpolating the relative stiffness of the tire in radial direction and at every normal load.

4.6. Tire Tread Model

In order to incorporate the tread design, a certain number of brush elements are assigned to each belt element in a rectangular array. Consider an array of bristles with N_{tread_circ} elements in the circumferential direction and N_{tread_lat} elements in the lateral direction. As a result, the number of total sensor points assigned to each belt element will be:

$$N_{tread\_total} = N_{tread\_circ} \times N_{tread\_lat} \tag{50}$$

Each brush element is a massless bristle that has translational stiffness in radial, longitudinal, and lateral directions. The base of these bristles is connected to each lumped mass (element segment), and the tip is touching the ground. This massless tip acts as a sensor point and can be used to detect the tire-road contact. Also, using the direction and the value of the deflection in the bristle, the ground forces generated are calculated. Through implementation of the sensor points, we are able to increase the resolution of the contact patch by having more contact detection points it this area. At the same time, to define their velocities in space, these massless points only require

extrapolation of the position and velocity of the nearby belt elements without the need for differential equations. Based on the findings of [74], there are only three state variables needed to describe the position of the brush tips in the space. These variables store the displacements of the brush tips in the global reference frame from previous iterations of the solver. Therefore, the state vector of each brush element will be:

$$ {}_{brush}q_{i,j}^{m,n} = \begin{bmatrix} \lambda_{i,j}^{(1)} \\ \lambda_{i,j}^{(2)} \\ \lambda_{i,j}^{(3)} \end{bmatrix} \qquad \begin{cases} i = 1,...,N_{tread\_lat} \\ j = 1,...,N_{tread\_circ} \end{cases} \tag{51} $$

Where m and n are the indices for the associated nth belt element in the m^{th} belt segment. The final state vector of the system can be constructed as follows:

$$ {}_{total}q = \begin{bmatrix} {}_{rim}q \\ {}_{seg}q \\ {}_{brush}q \end{bmatrix} \tag{52} $$

4.7. Initial Position Initialization

The initial position of the rim is expressed in the global reference frame by:

$$ {}_{rim}^{G}r_o = \begin{bmatrix} x_\circ \\ y_\circ \\ z_\circ \end{bmatrix} \tag{53} $$

The initial position of the tire elements depends on the tire geometrical properties, as well as the rim initial camber and slip angles. Consider the tire element P, with the position vector ${}^{W}r$ described in the wheel local reference frame noted as C-Axis. If this reference frame rotates around global X, Y, and Z axes with ψ, θ, and ϕ respectively, the coordinates of the point P in the global and in the rim local reference frames can be related using the equation:

$$ {}^{G}r = R_{total}\,{}^{W}r \tag{54} $$

Where R_{total} is the total transformation matrix after three consecutive rotations and can be calculated by multiplying individual transformation matrices for the rotation around each axis successively:

$$ R_{total} = R_{Y,\theta} R_{X,\psi} R_{Z,\phi} \tag{55} $$

$$ R_{Y,\theta} = \begin{bmatrix} \cos(\theta) & 0 & \sin(\theta) \\ 0 & 1 & 0 \\ -\sin(\theta) & 0 & \cos(\theta) \end{bmatrix} \tag{56} $$

$$ R_{Z,\phi} = \begin{bmatrix} \cos(\phi) & -\sin(\phi) & 0 \\ \sin(\phi) & \cos(\phi) & 0 \\ 0 & 0 & 1 \end{bmatrix} \tag{57} $$

$$ R_{X,\psi} = \begin{bmatrix} 1 & 0 & 0 \\ 0 & \cos(\psi) & -\sin(\psi) \\ 0 & \sin(\psi) & \cos(\psi) \end{bmatrix} \tag{58} $$

The position vector of the j^{th} element in the first tire segment is:

$$ {}^{W}_{seg}r_{1,j} = \begin{bmatrix} tire\_radius \\ \left(j - \dfrac{N_{seg\_elm}+1}{2} \right) \times \Delta y_{seg\_elm} \\ 0 \end{bmatrix} \tag{59} $$

Where Δy_{seg_elm} is the lateral displacement between the centers of two adjacent elements in each tire segment:

$$ \Delta y_{seg\_elm} = \frac{tire\_width}{N_{seg\_elm} - 1} \tag{60} $$

Consequently the local position of the j^{th} element in the i^{th} segment is:

$$ {}^{W}_{seg}r_{i,j} = R_{Y,(\Delta\theta_{seg}\times i)} \times {}^{W}_{seg}r_{1,j} \tag{61} $$

Where $\Delta\theta_{seg}$ is the angular difference between two adjacent belt segments:

$$ \Delta\theta_{seg} = \frac{2\pi}{N_{belt\_seg}} \tag{62} $$

The initial position of the j^{th} element in the i^{th} belt segment described in the global reference frame can be expressed as:

$$ {}^{G}_{seg}r_{i,j} = {}^{G}_{rim}r_{o} + R_{Z,(Slip\_angle)} \times R_{Z,(Camber\_angle)} \times {}^{W}_{seg}r_{i,j} \tag{63} $$

Finally, the initial state vector of the system becomes:

$$ {}_{total}q_{\circ} = \begin{bmatrix} {}_{rim}q_{\circ} \\ {}_{seg}q_{\circ} \\ {}_{brush}q_{\circ} \end{bmatrix} \tag{64} $$

4.8. Tire Kinematics

In order to write the equations of motion for the rim and the lumped masses, the internal forces between the tire elements and the rim should be identified. The Kelvin-Voigt force elements that connect tire belt elements to each other and to the rim generate the internal forces as functions of relative displacement and relative velocity of lumped masses with respect to the rim circumference. Therefore, formulating the model kinematics is essential for calculating the kinetics of the elements. In this section, a set of kinematic parameters that are required for writing the model equations of motion are introduced.

The transformation matrix for the i^{th} belt segment is defined as:

$$ R^{i}_{tot} = R_{Z,\phi_{rim}} \times R_{X,\psi_{rim}} \times R_{Y,(\theta_{rim}+\Delta\theta_{seg}\times i)} \tag{65} $$

For the un-inflated tire, the unity vector ${}^{G}_{cw}r_i$ normal to the center of the i^{th} belt segment, which passes through the rim center is given as:

$$ {}^{G}_{cw}r_i = R^i_{tot} \times \begin{bmatrix} Tire\_radius \\ 0 \\ 0 \end{bmatrix} \tag{66} $$

$$ {}^{G\wedge}_{cw}r_i = \frac{{}^{G}_{cw}r_i}{\left| {}^{G}_{cw}r_i \right|} \tag{67} $$

The vector from the rim center to the j^{th} element of the i^{th} belt segment of the tire is:

$$ {}^{G}_{cwo}r_{i,j} = R^i_{tot} \times \begin{bmatrix} Tire\_radius \\ \left(j - \frac{N_{seg\_elm}+1}{2} \right) \Delta y_{seg\_elm} \\ 0 \end{bmatrix} \tag{68} $$

$$ {}^{G\wedge}_{cwo}r_{i,j} = \frac{{}^{G}_{cwo}r_{i,j}}{\left| {}^{G}_{cwo}r_{i,j} \right|} \tag{69} $$

The relative position of the first belt element near the left sidewall in the i^{th} belt segment from its projection on the rim is given as:

$$ {}^{G}_{wtl}r_i = {}^{G}_{tire}r_{i,N_{belt\_seg}} - {}^{G}_{rim}r_{i,N_{belt\_seg}} \tag{70} $$

Similarly, the relative position of the last belt element near the right sidewall in the i^{th} belt segment from its projection on the rim is given as:

$$ {}^{G}_{wtr}r_i = {}^{G}_{tire}r_{i,1} - {}^{G}_{rim}r_{i,1} \tag{71} $$

For the intermediate belt elements located between the first and last elements, which are directly connected to the rim, the relative position of each element from the center of its left and right neighboring elements are:

$$ {}_{left\_elm}^{G}r_{i,j} = {}_{tire}^{G}r_{i,j} - {}_{tire}^{G}r_{i,j+1} \qquad j = 2,...,N_{seg\_elm} - 1 \tag{72} $$

$$ {}_{right\_elm}^{G}r_{i,j} = {}_{tire}^{G}r_{i,j} - {}_{tire}^{G}r_{i,j-1} \qquad j = 2,...,N_{seg\_elm} - 1 \tag{73} $$

The relative position of the tread block center from its neighbor j^{th} belt element is:

$$ {}_{tread}^{G}r_{i,j} = {}_{tire}^{G}r_{i,j} + \left|tread\_tickness\right| \times {}_{cw}\hat{r}_i \tag{74} $$

The local coordinate system at the center of the i^{th} belt segment described in global reference frame is:

$$ {}_{tread}^{G}r_{i,j} = {}_{tire}^{G}r_{i,j} + \left|tread\_tickness\right| \times {}_{cw}\hat{r}_i \tag{75} $$

The position of the point P described at the local reference frame of the i^{th} belt segment is:

$$ {}_{belt}P^i = p_1 \cdot e_1^i + p_2 \cdot e_2^i + p_3 \cdot e_3^i \tag{76} $$

Where:

$$ e_1^i = \frac{\tilde{e}_2^i \times {}_{cw}\hat{r}_i}{\left\| \tilde{e}_2^i \times {}_{cw}\hat{r}_i \right\|}, \quad e_2^i = \frac{R_{Z,\phi_{rim}} \times R_{X,\psi_{rim}} \times \begin{bmatrix} 0 & 1 & 0 \end{bmatrix}^T}{\left\| R_{Z,\phi_{rim}} \times R_{X,\psi_{rim}} \times \begin{bmatrix} 0 & 1 & 0 \end{bmatrix}^T \right\|}, \quad e_3^i = {}_{cw}\hat{r}_i \tag{77} $$

$$ \tilde{e}_2^i = \begin{bmatrix} 0 & -e_{2z}^1 & e_{2y}^i \\ e_{2z}^i & 0 & -e_{2x}^i \\ -e_{2y}^i & e_{2x}^i & 0 \end{bmatrix} \tag{78} $$

The tire structural stiffness and damping behaviors are simulated using the tire model Voigt elements. The force that is produced by a Voigt element is proportional to its length and the relative velocity between its two ends. The direction of this force is parallel to the element centerline. Therefore, the position and velocity of the force element tips relative to their bases should be calculated.

The relative distance between a lumped mass in the j^{th} belt element and its projected position on the rim, described in the i^{th} belt segment local reference frame is expressed as:

$$ {}_{belt}D^{i,j} = DT_1^{i,j} \cdot e_1^i + DT_2^{i,j} \cdot e_2^i + DT_3^{i,j} \cdot e_3^i \tag{79} $$

Where

$$ \begin{bmatrix} DT_1 \\ DT_2 \\ DT_3 \end{bmatrix}^{i,N_{belt\_elm}} = \begin{bmatrix} e_1^i \\ e_2^i \\ e_3^i \end{bmatrix}^T \cdot {}^G_{wtl}r \tag{80} $$

$$ \begin{bmatrix} DT_1 \\ DT_2 \\ DT_3 \end{bmatrix}^{i,1} = \begin{bmatrix} e_1^i \\ e_2^i \\ e_3^i \end{bmatrix}^T \cdot {}^G_{wtr}r \tag{81} $$

The relative distance between the center of the j^{th} belt element and its left and right belt element neighbors, described in the i^{th} belt segment local reference frame is given as:

$$ \begin{bmatrix} DBL_1 \\ DBL_2 \\ DBL_3 \end{bmatrix}^{i,j} = \begin{bmatrix} e_1^i \\ e_2^i \\ e_3^i \end{bmatrix}^T \cdot {}^G_{left\_elm}r_{i,j} \qquad j = 1,...,N_{seg\_elm} - 1 \tag{82} $$

$$ \begin{bmatrix} DBR_1 \\ DBR_2 \\ DBR_3 \end{bmatrix}^{i,j} = \begin{bmatrix} e_1^i \\ e_2^i \\ e_3^i \end{bmatrix}^T \cdot {}^G_{wtl}r - {}^G_{right\_elm}r_{i,j} \qquad j = 2,...,N_{seg\_elm} \tag{83} $$

Relative velocity component becomes:

$$ {}^{W}\dot{DT}^{i,j} = \dot{DT}_1^{i,j} \cdot e_1^i + \dot{DT}_2^{i,j} \cdot e_2^i + \dot{DT}_3^{i,j} \cdot e_3^i \tag{84} $$

$$ \begin{bmatrix} \dot{DT}_1 \\ \dot{DT}_2 \\ \dot{DT}_3 \end{bmatrix}^{i,N_{belt\_elm}} = \begin{bmatrix} e_1^i \\ e_2^i \\ e_3^i \end{bmatrix}^T \cdot {}^{G}_{wtl}\dot{r}^i \tag{85} $$

$$ \begin{bmatrix} \dot{DT}_1 \\ \dot{DT}_2 \\ \dot{DT}_3 \end{bmatrix}^{i,1} = \begin{bmatrix} e_1^i \\ e_2^i \\ e_3^i \end{bmatrix}^T \cdot {}^{G}_{wtr}\dot{r}^i \tag{86} $$

$$ \begin{bmatrix} \dot{DBL}_1 \\ \dot{DBL}_2 \\ \dot{DBL}_3 \end{bmatrix}^{i,j} = \begin{bmatrix} e_1^i \\ e_2^i \\ e_3^i \end{bmatrix}^T \cdot {}^{G}_{left\_elm}\dot{r}_{i,j} \qquad j = 1,...,N_{seg\_elm} - 1 \tag{87} $$

$$ \begin{bmatrix} \dot{DBR}_1 \\ \dot{DBR}_2 \\ \dot{DBR}_3 \end{bmatrix}^{i,j} = \begin{bmatrix} e_1^i \\ e_2^i \\ e_3^i \end{bmatrix}^T \cdot {}^{G}_{right\_elm}\dot{r}_{i,j} \qquad j = 2,...,N_{seg\_elm} \tag{88} $$

Where

$$ {}^{G}_{left\_elm}\dot{r}_{i,j} = {}^{G}_{tire}\dot{r}_{i,j} - {}^{G}_{tire}\dot{r}_{i,j+1} \tag{89} $$

$$ {}^{G}_{right\_elm}\dot{r}_{i,j} = {}^{G}_{tire}\dot{r}_{i,j} - {}^{G}_{tire}\dot{r}_{i,j-1} \tag{90} $$

Velocity of a point located at the projection of the j^{th} belt element in the i^{th} belt segment on the rim circumference, and described in the i^{th} belt segment local reference frame is:

$$ {}^{W}_{rim\_circ}v_{i,j} = \begin{bmatrix} e_1^i \\ e_2^i \\ e_3^i \end{bmatrix}^T \cdot {}^{G}_{rim\_circ}v_{i,j} \tag{91} $$

$$ {}^{G}_{rim\_circ}v_{i,j} = v_{rim} + \tilde{\Omega}_{rim} \times_{cwo} \hat{r}_{i,j} \tag{92} $$

4.9. Tire Kinetics

The components of the left sidewall force vector between i^{th} belt segment and the rim are calculated as:

$$ \begin{bmatrix} FL_1 \\ FL_2 \\ FL_3 \end{bmatrix}^i = \begin{bmatrix} e_1^i \\ e_2^i \\ e_3^i \end{bmatrix}^T \cdot \begin{bmatrix} -k_{t1} \cdot \left(DT_1^{i,N_{belt\_elm}}\right) - c_{t1}\left(\dot{DT}_1^{i,N_{belt\_elm}} - \left({}^{W}_{rim\_circ}v_{i,N_{belt\_elm}}\right)_1\right) \\ -k_{t2} \cdot \left(DT_2^{i,N_{belt\_elm}}\right) - c_{t2}\left(\dot{DT}_2^{i,N_{belt\_elm}} - \left({}^{W}_{rim\_circ}v_{i,N_{belt\_elm}}\right)_2\right) \\ -k_n \cdot \left(DT_3^{i,N_{belt\_elm}} - h_{carcass}\right) - c_n\left(\dot{DT}_3^{i,N_{belt\_elm}} - \left({}^{W}_{rim\_circ}v_{i,N_{belt\_elm}}\right)_3\right) \end{bmatrix} \tag{93} $$

Where $h_{carcass}$ is the tire carcass height, k_{t1} is tire sidewall tangential stiffness, c_{t1} is tire sidewall tangential damping, k_{t2} is tire sidewall lateral stiffness, c_{t2} is tire sidewall lateral damping, k_n is tire sidewall radial stiffness, and c_n is tire sidewall radial damping. The resultant force that is applied to the i^{th} belt segment by the rim from the left sidewall is given as:

$$ {}^{W}_{sidewall}FL^{i,j} = FL_1^i + FL_2^i + FL_3^i \tag{94} $$

Similarly for the force vector in the right sidewall between tire and the rim we have:

$$\begin{bmatrix} FR_1 \\ FR_2 \\ FR_3 \end{bmatrix}^i = \begin{bmatrix} e_1^i \\ e_2^i \\ e_3^i \end{bmatrix}^T \cdot \begin{bmatrix} -k_{t1} \cdot \left(DT_1^{i,1}\right) - c_{t1}\left(\dot{DT}_1^{i,1} - \left({}^{W}_{rim\_circ}v_{i,1} \right)_1 \right) \\ -k_{t2} \cdot \left(DT_2^{i,1}\right) - c_{t2}\left(\dot{DT}_2^{i,1} - \left({}^{W}_{rim\_circ}v_{i,1} \right)_2 \right) \\ -k_n \cdot \left(DT_3^{i,1} - h_{carcass}\right) - c_n\left(\dot{DT}_3^{i,1} - \left({}^{W}_{rim\_circ}v_{i,1} \right)_3 \right) \end{bmatrix} \tag{95}$$

The resultant force that is applied to the i^{th} belt segment by the rim from the right the sidewall is given as:

$${}^{W}_{sidewall}FR^{i,j} = FR_1^i + FR_2^i + FR_3^i \tag{96}$$

Next, the force components within the belt segment that are generated between the neighboring belt elements are calculated. The forces exerted to the j^{th} belt element in the i^{th} belt segment by its neighboring elements are:

$$\begin{bmatrix} FB_1 \\ FB_2 \\ FB_3 \end{bmatrix}^{i,j} = \left(e^i\right)^T \cdot \left[K_{belt} \cdot \left(DBR^{i,j} + DBL^{i,j}\right) - C_{belt} \cdot \left(\dot{DBR}^{i,j} + \dot{DBL}^{i,j} - {}^{G}_{rightt\_elm}\dot{r}_{i,j} - {}^{G}_{left\_elm}\dot{r}_{i,j} \right) \right] \tag{97}$$

Where K_{belt} is the tire belt stiffness matrix and is defined as:

$$K_{belt} = \begin{bmatrix} k_{bt1} & 0 & 0 \\ 0 & k_{bt2} & 0 \\ 0 & 0 & k_n \end{bmatrix} \tag{98}$$

In the tire belt mass matrix, k_{bt1} is the tire belt inner-tangential stiffness, k_{bt2} is the tire belt inner-lateral stiffness, and k_{bn} is the tire belt inner-radial stiffness. Moreover, C_{belt} is the tire belt damping matrix, which is defined as:

$$C_{belt} = \begin{bmatrix} c_{bt1} & 0 & 0 \\ 0 & c_{bt2} & 0 \\ 0 & 0 & c_n \end{bmatrix} \tag{99}$$

In the tire belt damping matrix, c_{bt1} is tire belt inner-tangential damping, c_{bt2} is tire belt inner-lateral damping, and c_{bn} is tire belt inner-radial damping. The total force vector that was exerted to the j^{th} belt element in the i^{th} belt segment from its neighboring elements can be identified as:

$${}^{W}FB^{i,j} = FB_1^{i,j} + FB_2^{i,j} + FB_3^{i,j} \tag{100}$$

Therefore, the total structural forces on the j^{th} belt element in the i^{th} belt segment is given as:

$${}^{W}_{structure}F^{i,j} = {}^{W}FB^{i,j} + {}^{W}_{sidewall}FL^{i,j} + {}^{W}_{sidewall}FR^{i,j} \tag{101}$$

Finally, the total internal force that is applied to the belt element can be written as:

$${}^{W}_{\text{int}ernal}F^{i,j} = {}^{W}_{structure}F^{i,j} + \begin{bmatrix} 0 \\ 0 \\ -mg \end{bmatrix} + F^{i,j}\left(r_{tire}, t\right) \cdot \hat{e}_3 \tag{102}$$

The torque from the tire i^{th} belt segment to the rim is written as:

$${}^{W}_{belt}T^{i} = {}_{cwo}\tilde{r}^{i,1} \times {}^{W}_{structure}F^{i,1} + {}_{cwo}\tilde{r}^{i,N_{belt\_elm}} \times {}^{W}_{structure}F^{i,N_{belt\_elm}} \tag{103}$$

Where:

$${}_{cwo}\tilde{r}^{i,j} = \begin{bmatrix} 0 & -{}_{cwo}r_3^{i,j} & {}_{cwo}r_2^{i,j} \\ {}_{cwo}r_3^{i,j} & 0 & -{}_{cwo}r_1^{i,j} \\ {}_{cwo}r_2^{i,j} & {}_{cwo}r_1^{i,j} & 0 \end{bmatrix}$$

After calculating the individual force components applied to each lumped mass, we can write the equation of motion such as:

$$\begin{bmatrix} \ddot{x} \\ \ddot{y} \\ \ddot{z} \end{bmatrix} = \frac{1}{m}\left\{ {}_{structural}F + {}_{internal}F + {}_{external}F + {}_{gravity}F \right\} \tag{104}$$

$${}_{lumped\_mass}{}^{G}q^{i,j} = \begin{bmatrix} x & \dot{x} & y & \dot{y} & z & \dot{z} \end{bmatrix} \tag{105}$$

For simplicity, the rim is considered as a spatial rigid body. As a result, three translational and three rotational DOF are used for describing its motion:

$$m \cdot \ddot{r} = {}^{G}F = {}_{rim}{}^{G}F + \sum {}_{belt}F^{i} \tag{106}$$

$$J \cdot \ddot{\phi} = {}^{G}M = {}_{rim}M + \sum {}_{bet}M^{i} \tag{107}$$

Where ${}_{rim}F$ is the applied force vector to the rim center, ${}_{belt}F^{i}$ is the structural force from the i^{th} belt segment, ${}_{rim}M$ is the applied torque vector to the rim center, and ${}_{belt}M^{i}$ is the applied toque vector from i^{th} belt segment to the rim center, and is given as:

$$\sum {}_{bet}M^{i} = \sum \left[\left({}_{rim\_circ}r - {}_{rim}r \right) \times F^{i} \right] \tag{108}$$

The rim translational dynamics is represented in the global reference frame as follows:

$${}^{G}F = m \cdot \left({}_{rim}{}^{G}a \right) = m \cdot \left({}_{rim}{}^{G}\ddot{r} \right) \tag{109}$$

Consequently, rim translational equations of motion expressed in the rim local reference frame are given as:

$${}^{W}F = {}^{W}R_{G}\,{}^{G}F = m\,{}^{W}R_{G}\,{}_{rim}{}^{G}\ddot{r} = m\left({}_{rim}{}^{B}\ddot{r} \right) + m\left({}^{W}\omega \times {}_{rim}{}^{W}\dot{r} \right) \tag{110}$$

With the following vector form:

$$
{}^{W}\begin{bmatrix} F_x \\ F_y \\ F_z \end{bmatrix} = m\,{}^{W}\begin{bmatrix} \ddot{r}_x \\ \ddot{r}_y \\ \ddot{r}_z \end{bmatrix} + m\,{}^{W}\begin{bmatrix} w_x \\ w_y \\ w_z \end{bmatrix} \times {}^{W}\begin{bmatrix} \dot{r}_x \\ \dot{r}_y \\ \dot{r}_z \end{bmatrix} = m\,{}^{W}\begin{bmatrix} \ddot{r}_x + \left(w_y \dot{r}_z - w_z \dot{r}_y \right) \\ \ddot{r}_y + \left(w_x \dot{r}_z - w_z \dot{r}_x \right) \\ \ddot{r}_z + \left(w_x \dot{r}_y - w_y \dot{r}_x \right) \end{bmatrix} \tag{111}
$$

The applied forces to the rim center consist of the axle forces and suspension forces:

$$
{}^{G}_{rim}F = {}^{G}_{axle}F + {}^{G}_{suspension}F \tag{112}
$$

Next, the rotational dynamics for the rim is studied. The applied moment to the rim from the axle, described in the rim local reference frame, is given as:

$$
{}^{W}_{rim}M = M_x \hat{i} + M_y \hat{j} + M_z \hat{k} = I\,{}^{W}_{rim}\dot{\omega} + {}^{W}_{rim}\omega \times \left(I\,{}^{W}_{rim}\omega \right) \tag{113}
$$

Where ${}^{W}_{rim}\omega$ is the rim angular velocity vector, and I is the inertia matrix, which is written as:

$$
I = \begin{bmatrix} I_{xx} & I_{xy} & I_{xz} \\ I_{yx} & I_{yy} & I_{yz} \\ I_{zx} & I_{zy} & I_{zz} \end{bmatrix} \tag{114}
$$

Additionally, the components of the torque vector are described as:

$$
M_x = I_{xx}\dot{\omega}_x + I_{xy}\dot{\omega}_y + I_{xz}\dot{\omega}_z - \left(I_{yy} - I_{zz} \right)\omega_y\omega_z - I_{yz}\left(\omega_z^2 - \omega_y^2 \right) - \omega_x\left(\omega_z I_{xy} - \omega_y I_{xz} \right) \tag{115}
$$

$$
M_y = I_{yx}\dot{\omega}_x + I_{yy}\dot{\omega}_y + I_{yz}\dot{\omega}_z - \left(I_{zz} - I_{xx} \right)\omega_x\omega_z - I_{xz}\left(\omega_x^2 - \omega_z^2 \right) - \omega_y\left(\omega_x I_{yz} - \omega_z I_{xy} \right) \tag{116}
$$

$$
M_z = I_{zx}\dot{\omega}_x + I_{zy}\dot{\omega}_y + I_{zz}\dot{\omega}_z - \left(I_{xx} - I_{yy} \right)\omega_x\omega_y - I_{xy}\left(\omega_y^2 - \omega_x^2 \right) - \omega_z\left(\omega_y I_{xz} - \omega_x I_{yz} \right) \tag{117}
$$

If we assume the orientation of the rim such that $I_{ij} = 0$ when $i \neq j$, the rim coordinate system becomes a principal coordinate frame and the moment vector components are identified as:

$$M_x = I_{xx}\dot{\omega}_x - \left(I_{yy} - I_{zz}\right)\omega_y\omega_z \tag{118}$$

$$M_y = I_{yy}\dot{\omega}_y - \left(I_{zz} - I_{xx}\right)\omega_x\omega_z \tag{119}$$

$$M_z = I_{zz}\dot{\omega}_z - \left(I_{xx} - I_{yy}\right)\omega_x\omega_y \tag{120}$$

Consequently:

$$\ddot{\alpha} = \frac{1}{I_{xx}}\left(M_x + \left(I_{yy} - I_{zz}\right)\dot{\beta}\dot{\delta}\right) \tag{121}$$

$$\ddot{\alpha} = \frac{1}{I_{xx}}\left(M_x + \left(I_{yy} - I_{zz}\right)\dot{\beta}\dot{\delta}\right) \tag{122}$$

$$\ddot{\delta} = \frac{1}{I_{zz}}\left(M_z + \left(I_{xx} - I_{yy}\right)\dot{\beta}\dot{\alpha}\right) \tag{123}$$

The moment equations, for the sidewall, that exist between the belts segments and the rim are expressed in the wheel local reference frame. In order to express these equations in the global reference frame, the following transformation matrix is used:

$${}_{rim}R(t) = R_{Z,\delta(t)}R_{X,\alpha(t)}R_{Z,\beta(t)} \tag{124}$$

It should be noted that the transformation matrix in (91) is a function of time, and is recalculated at every time step based on the spatial orientation of the rim. The final moment vector at the spindle form the tire sidewall, expressed in global reference frame is calculated as:

$${}_{sidewall}^{G}M^{i} = {}_{rim}R(t)\cdot {}_{sidewall}^{B}M^{i} \tag{125}$$

Where ${}_{sidewall}^{B}M$ is the sum of individual torque vectors applied by the belt segments to the tire, as follows:

$$ {}^{B}_{spindle}M = \sum_{i=1}^{N_{belt\_seg}} \left({}^{B}_{sidewall}M^{i} \right) \tag{126} $$

4.10. Conclusion

In summary, the kinetics and the kinematics of the tire structure were formulated using a lumped parameter approach. Considering the fact that only forces and moments are required at the tire spindle in this approach, a relatively coarse level of tire structure discretization was chosen that can lead to a faster computational time. The tire carcass was divided into multiple segments that are suspended by the rim using the force elements. These force elements represent the sidewall characteristics of the tire. Each carcass segment includes a user-defined number of lumped masses that are connected to each other using force elements in in-plane and in out-of-plane directions. Finally, the equations of motion were derived for the lumped masses and the rigid wheel.

Chapter 5: Tire-Terrain Interactions

5.1. Introduction

Once the tire structure and the tire material properties are modeled and implemented in the mathematical framework, the interface between the tire and the road surface should be established. This interface searches for the nodal points that are close to the ground (contact search algorithm), and once the contact is detected, the algorithm applies the required contact condition (contact interface algorithm). Therefore, the contact simulation is initiated by detecting the penetration between the objects and then, by applying the contact constraints (such as contact forces), this penetration is reduced, minimized, or eliminated [37, 124].

Furthermore, the mechanics of the tire-terrain interaction is fundamentally important in characterizing the performance of the tire on the terrain. In this regard, the mechanics of the tire-terrain interaction is divided into on-road and off-road case studies. For the on-road studies, the terrain is considered as a solid (non-deformable) surface with irregularities. For this type of terrain, researchers have developed various high-fidelity models that can capture the tire response properties [2, 6, 125, 126]. Additionally, multiple commercial tire models have been developed for integration with vehicle simulation software [8, 127, 128]. For off-road cases, the terrain is assumed as a deformable media, and, as a result, the complexity of the contact modeling problem increases [44]. A direct application of an on-road tire model to simulate tire performance on soft soil is not possible. This is due to the fact that traveling on deformable terrain raises issues that on-road tire models do not account for.

Different terrains respond differently to similar loading inputs. The key factor for characterizing this behavior is to describe different terrain responses to the loading inputs using

mathematical relationships such as stress-strain relationship, pressure-sinkage relationship, and shear stress-shear displacement relationship [117]. The structure of the natural terrains varies greatly, and, as a result, the terrain responses cannot be modeled using a single theory or method. The techniques for investigating the tire interaction with deformable terrain can be categorized into three main groups [75]: (1) empirical methods, (2) analytical methods, and (3) semi-empirical methods.

For empirical models, researchers measure terrain responses under conditions that are close to the vehicle operational condition, and then construct the empirical functions through curve-fitting and statistical analysis of the measurement data. Although the empirical models are good for simple mobility assessments, they cannot be extrapolated beyond the test data used to establish them. The physics-based models incorporate methods including computational physics and numerical analysis to construct an applied framework for the complex problem of soil-tire interaction. These models require high computational resources to handle their highly discretized structures. Additionally, most of the models in this group (except for very detailed FEM models [52]) use simplified parameterization procedures to evaluate the material properties and simulation input parameters. Consequently, correlating the physics-based models results with the experimental data is challenging. On the other hand, semi-empirical methods employ the empirical relations in addition to analytical approaches in order to achieve high fidelity results while keeping the computational effort and number of model variables low. Therefore, they are considered as good candidates for using in MBS and vehicle simulations.

In the following sections, the semi-empirical terrain module developed is introduced first and its functionality within the HSSTM simulation environment is described. The terrain module consists of contact search and contact interface algorithms, which are elaborated, respectively. The

contact interface algorithms for deformable and non-deformable terrains are handled differently due to the unique characteristics of each case. Finally, the terrain model is integrated within the HSSTM package, and multiple simulation case studies are conducted on various types of terrains and with different simulation input conditions. The simulation results are compared with the experimental data to evaluate the performance of the terrain model.

5.2. Terrain Model

The developed tire model should be able to function in a complete vehicle simulation environment, and provide forces and moments at various input conditions. At the beginning of each simulation time step, vehicle model provides the tire model with wheel kinetic and kinematic variables including spindle position, orientation, and velocity components. Tire model uses these data in addition to the previous state of the tire/road contact point and road surface to estimate the deflection of the tire. Next, the tire model provides the wheel center data and the approximate position of the tire contact patch to the terrain model, in order to calculate the new tire/terrain contact point coordinates. The terrain model estimates the normal and the shear pressure distribution at the contact patch, and updates the terrain profile based on the penetration of the tire into the terrain. The tire model uses the pressure distribution at the contact patch to calculate the resultant forces and moments (F&M). The calculated F&M are transformed from the W-Axis coordinate system, located at the center of the contact patch, to the coordinate system located at the wheel center. The vehicle model receives the tire F&M data at the wheel center, and solves the inertia equations for the wheel assembly, which will result in the updated wheel kinetics and kinematics at the end of the time step. The simulation environment data flow during tire-terrain interaction is shown in Figure 22.

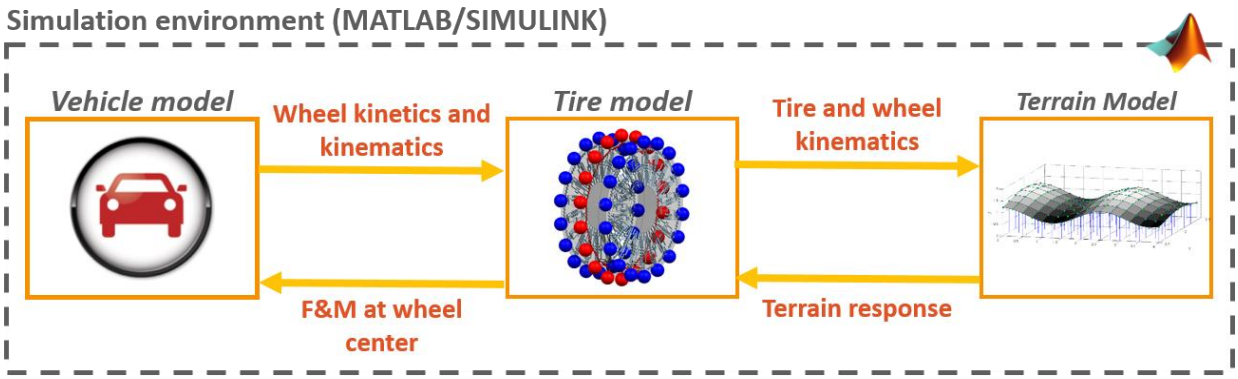

Figure 22: Simulation environment data flow during tire-terrain interaction

5.3. Contact Analysis

During tire interaction with terrain, the contact algorithm searches for the nodal points that are close to the ground (contact search algorithm), and when the contact is detected it applies the required contact condition (contact interface algorithm). Therefore, the contact simulation is initiated by detecting the penetration between the objects and then, by applying the contact constraints (such as contact forces), this penetration is reduced, minimized, or eliminated.

5.3.1. Contact Detection Algorithm

Two main scenarios in the contact problems can be identified as master-slave contact and self-contact. During master-slave contact, surfaces of the two objects have contact with each other, and each node of the slave surface is checked for penetration into the elements of the master surface. The self-contact requires interaction of the segments of the object with themselves, which is the case for crash simulations and airbag deployment. For this type, there is only one slave surface, and nodes/edges of the surface are examined for penetration into the segments of the same surface. The master-slave contact method is used for developing the tire-ground contact detection algorithm. The master nodes are considered as the lumped masses and salve surface is assumed to be ground. The ground elevation model is constructed using the three dimensional regular grid

road data files (RGR Files). The ground geometry representation using this method is shown in Figure 23.

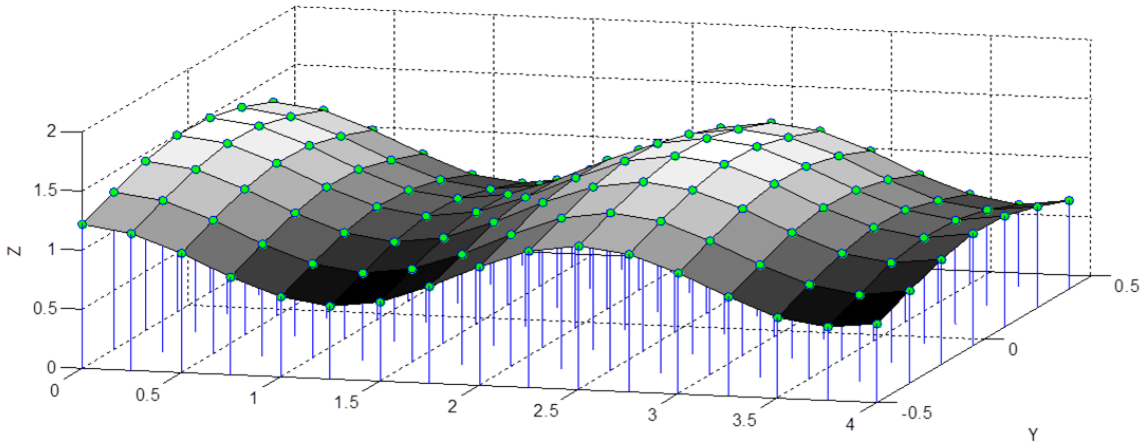

Figure 23: Three-dimensional soil elevation map representation using the three dimensional regular grid road (RGR) data files.

The contact search algorithm can be divided into two main methods: node-to-segment correspondence search and node-to-node proximity search. The node-to-node proximity search algorithm looks for the closest master node to a certain slave node, and it is very useful for contact surfaces with matching mesh. Node-to-segment is mostly used for large deformation contact problems that exist between surfaces with non-matching meshes [124]. In this method, the proximity of the slave surface nodes to the master surface segments are examined, and, by preventing the penetration of nodes on the slave surface to corresponding master segments, the non-penetration conditions are enforced, as illustrated in Figure 24.

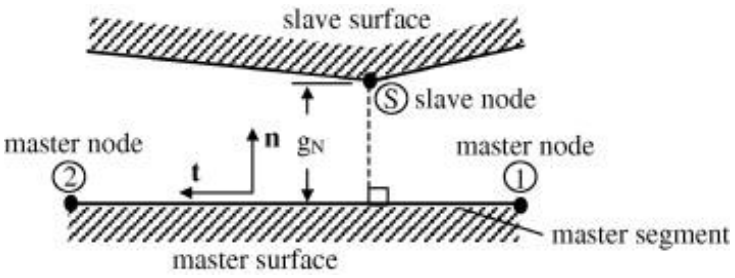

Figure 24: Node-to-segment contact element geometry (The node-to-segment algorithm for 2D frictionless contact: Classical formulation and special cases, Zavarise, G. and L. De Lorenzis, Computer Methods in Applied Mechanics and Engineering, 2009. 198(41–44): p. 3428-3451, use with the permission of Elsevier)

5.3.2. Contact Interface Algorithm: Penalty Method

After contact is properly detected, the contact conditions are applied upon penetration using the contact interface algorithm. The two major contact algorithms that are used extensively are Lagrange Multipliers and Penalty Method [52]. Penalty method calculates the contact forces relative to the contact penetration, and no extra degree-of-freedom is introduced into the system, as seen in Figure 25.

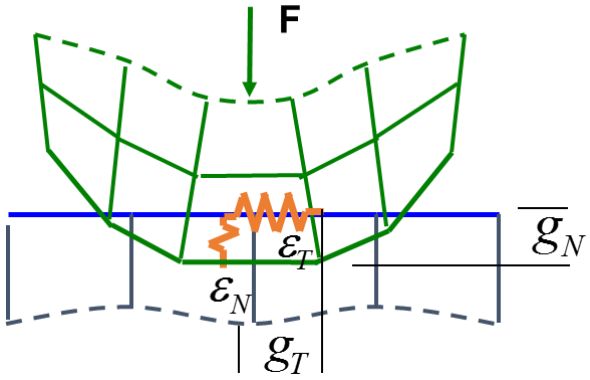

Figure 25: Penalty method contact

The amount of penetration is a function of bulk modulus, volume, and surface area of the master segment. The penalty parameter is analogous to a spring stiffness that produces a force based on its deflection. Therefore, this method does not consider a zero gap assumption between the contacting surfaces:

$$\Psi = \int_V \sigma^T \delta\varepsilon dV + \int_\Gamma \left(\varepsilon_N g_N \delta g_N + \varepsilon_T g_T \delta g_T\right) dA \tag{127}$$

Where Ψ is the total virtual work during contact, ε_N is the normal penalty term, g_N is normal penetration, ε_T is the tangential penalty term, g_T is tangential penetration. The normal and tangential contact forces in penalty method contact read:

$$F_n = \varepsilon_N g_N \tag{128}$$

$$F_T = -\text{sgn}\left(g_T\right)\mu\left(\varepsilon_N g_N\right) \tag{129}$$

Where μ is the coefficient of friction. It should be noted that as long as the penetration does not change the contact region, the penetration will not influence the contact pressure and stress underneath the contact element. The condition of the stiffness matrix crucially depends on the contact stiffness itself. If the contact stiffness is too large, it will cause convergence difficulties. In this case, the model can oscillate, with contacting surfaces bouncing off of each other.

5.3.3. Contact Interface Algorithm: Lagrange Multiplier Method

The Lagrange Multiplier method adds a term, which consists of a Lagrange Multiplier coefficient and a gap function λ, to the energy equation of the system:

$$\Psi = \int_V \sigma^T \delta\varepsilon dV + \int_\Gamma \left(\lambda_N \delta g_N + \lambda_T \delta g_T\right) dA \tag{130}$$

Contact constraint condition $g_N \geq 0$ ensures no penetration, and $\lambda_N \leq 0$ ensures compressive contact force/pressure. Also, $\lambda_N g_N = 0$ implies that there is no contact (non-zero gap) when $\lambda_N = 0$, and there is contact (non-zero contact force) when $g_N = 0$. The equation is linear, in case of linear elastic and Node-to-Node contact. Otherwise, the equation is nonlinear and an iterative method is used to solve the equation. Usually the Newton-Method is used.

The Lagrange Multiplier coefficient can be interpreted as a reaction force. It should be noted that the Lagrange Multiplier approach introduces new degrees of freedom into the system, which requires additional computational resources.

During tire contact with non-deformable surfaces, the Lagrange Multiplier Method is used for tire-terrain interaction modeling. However, for tire contact with deformable terrain, due to the high number of tire and terrain 3D elements, the penalty contact method is used.

5.4. Tire Contact with Non-deformable Terrain

The friction forces generated between the tire and road surface primarily determine the tire contact with a non-deformable surface. Consequently, having a proper friction model is the key factor in identifying tire-road friction dynamics. The two methods for including the tire friction dynamics are considered in this study. The first method is a relaxation length-based approach. This model is an extension of the Magic Formula tire model that includes a simple lumped-parameter brush sub-model of the tire tread compliance. The second method adopts a three dimensional brush model based on a first-order LuGre dynamic friction model. These approaches are discussed in more details in the following sections.

5.4.1. Relaxation Length Model

The steady-state F&M are considered time independent, which makes them functions of kinematic variables, such as slip angle or slip ratio. However, once these kinematic inputs are applied to the rolling tire, there is a time delay in the F&M generation. This dynamic delay is also known as the relaxation length, which is the distance that the tire travels until the F&M reach steady-state, every time the input conditions change. The relaxation length is different for longitudinal and lateral tire dynamics. In order to apply the transient effect to the already implemented tire model, new lagged slip angle and slip ratio values are calculated and passed to

the model [73]. Initially, the tire kinematic inputs are used to compute the velocity components in lateral and longitudinal directions:

$$V_x = V\cos\alpha \tag{131}$$

$$V_{sy} = |V_x|\tan\alpha \tag{132}$$

The following differential equation is employed for estimating the tire lateral deflection due to side slip v_α:

$$\frac{dv_\alpha}{dt} + \frac{1}{L_\alpha}|V_x|v_\alpha = |V_x|\tan\alpha = -V_{sy} \tag{133}$$

Where L_α is the lateral relaxation length, V_x is the longitudinal slip velocity, and V_{sy} is the lateral slip speed. With the cornering slip stiffness $C_{F\alpha}$ and carcass lateral stiffness C_{Fy}, the relaxation length may be introduced as:

$$L_\alpha = \frac{C_{F\alpha}}{C_{Fy}} \tag{134}$$

For linear, small slip condition, the modified slip angle becomes:

$$\tan\alpha' = \frac{v_\alpha}{L_\alpha} \tag{135}$$

The process workflow for calculating the lagged slip angle is shown in Figure 26.

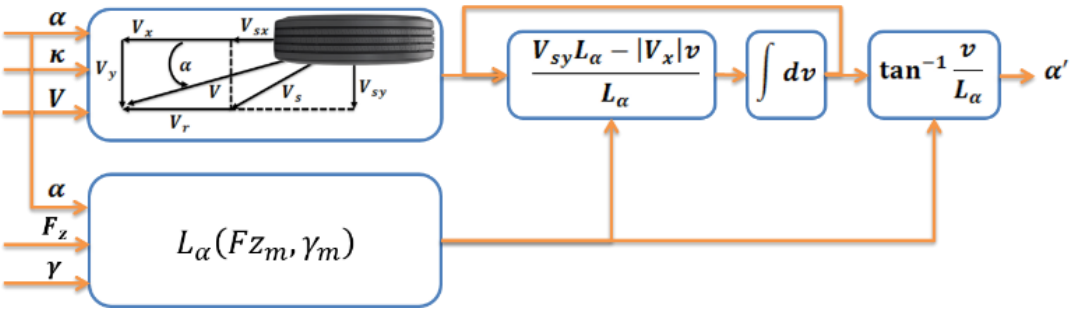

Figure 26: The signal workflow for calculating the lagged slip angle

In order to find the relaxation length, equation (130) should be rearranged in terms of lateral force. The lateral force from the road surface to the tire at steady-state condition read:

$$F_y^{ss} = C_{F\alpha}\alpha = -C_{F\alpha}\frac{V_{sy}}{|V_x|} \tag{136}$$

Also, the lateral internal force due to carcass deflection that balances the lateral side slip force is:

$$F_y = C_{Fy}v \tag{137}$$

Substituting equations (133) and (134) in (130) yields:

$$L_\alpha \frac{dF_y}{dt} + |V_x|F_y = |V_x|F_y^{ss} \tag{138}$$

The left side of this differential equation represents the transient lateral force at the tire/terrain single contact point, and the right side, corresponds to the lateral force at its steady-state condition $F_y^{ss}(\alpha, F_z, \gamma)$. This force is calculated directly from the pure slip lateral force regression function. The developed differential equation is equivalent to a first order delay:

$$\frac{F_Y}{F_Y^{ss}}(f_\alpha) = \frac{1}{i\left(2\pi\frac{L_\alpha}{V_x}f_\alpha\right)+1} = \frac{1}{\sqrt{\left(2\pi\frac{L_\alpha}{V_x}f_\alpha\right)^2+1}}\angle -\tan^{-1}\left(2\pi\frac{L_\alpha}{V_x}f_\alpha\right) \tag{139}$$

Where f_α is the frequency of input slip angle changes. The effect of the slip angle frequency changes on the lateral force is shown in Figure 27. At each frequency value, the slip angle increases from 0 to 1 degrees, then it decreases to -1 degree, and finally it increases again to 0 degrees. At very slow slip angle changes, the increasing and decreasing portions of the V_x vs α curve are very close, but as the frequency increases, they depart. This is due to the fact that at high frequency inputs, the tire cannot respond quickly to its inputs, due to the hysteresis in its tread and sidewall.

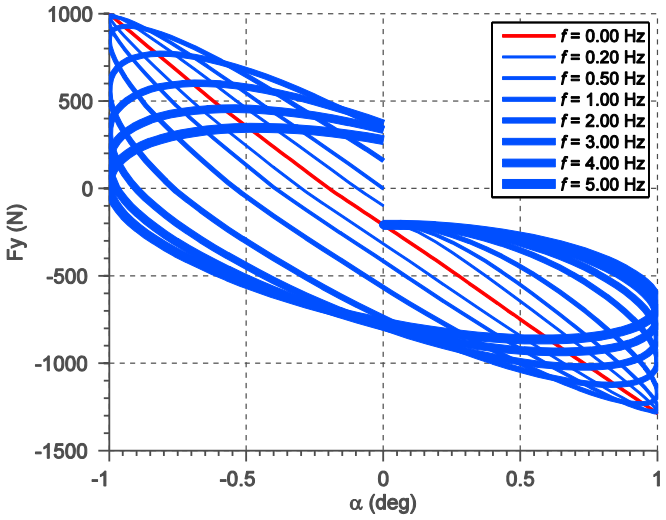

Figure 27: The effect of the slip angle frequency changes on lateral force

By keeping the longitudinal slip at zero, the relaxation length can be calculated as:

$$L_\alpha = \frac{V_x}{2\pi f_\alpha}\sqrt{\left(\frac{F_Y^{ss}}{F_Y}\right)^2 - 1} \tag{140}$$

To estimate the relaxation length, a transient pure cornering experimental test needs to be conducted. For this test, the input slip angle is varied using the chirp input signal during multiple transient cornering cycles at various camber angles and normal loads. Meanwhile, the spindle was set to a neutral condition to keep the slip ratio zero. The time history of the main input signals for the transient cornering test are shown in Figure 28. The shown signals are the commanded signals that should be applied to the tire in order to study the lateral force behavior due to harmonic slip angles, and at different levels of constant camber angle and normal load.

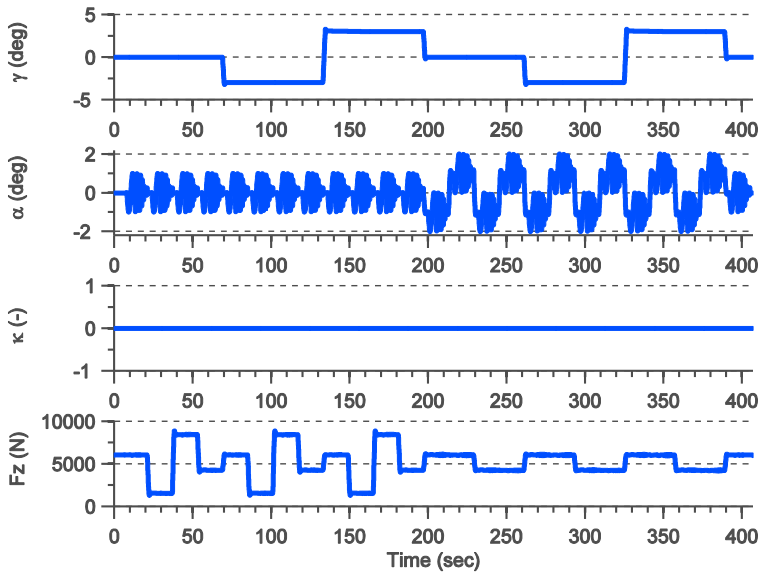

Figure 28: F&M test input signals for transient cornering maneuver

The recorded input and output signals including the lateral force from the spindle force hub are transformed to the tire contact patch, W-axis coordinate system, and divided into individual cycles for processing. Throughout each cycle, the slip angle input follows a commanded chirp signal that sweeps multiple frequencies including 0.2, 0.5, 1, 2, 3, 4, and 5 Hz for the duration of 5, 2, 2, 1, 1, 1, and 1 seconds respectively. For calculating the amplitude ratio and phase difference between lateral force output and slip angle input, the corresponding signals are fitted to harmonic functions at every frequency value tested. Next, the amplitude ratio and phase difference terms in the first order delay equation (136) are fitted to the harmonic fit data points using the least-square method, and the lateral relaxation length values are calculated.

It should be pointed out that at the end of the described process, the relaxation length values are calculated at various normal loads, camber angles, and average slip angles. Using these data points, the interpolation function $L_\alpha(Fz_m, \gamma_m)$ is constructed similarly to the multi-dimensional regression functions that were established for the cornering F&M data earlier. At each simulation step, using the function $L_\alpha(Fz_m, \gamma_m)$, the relaxation length is calculated based on the simulation

inputs, and passed on to the differential equation (130) to find the lagged slip angle value, as shown in Figure 26.

5.4.2. 3D Brush-type Friction Model

The tire tread is modeled as brushes with stiffness in longitudinal and lateral directions, as seen in Figure 29. The model is based on a 3D LuGre friction model that includes different friction effects including Coulomb or dry friction, viscous friction, Stribeck at low relative speeds, and stick in near zero speeds [129].

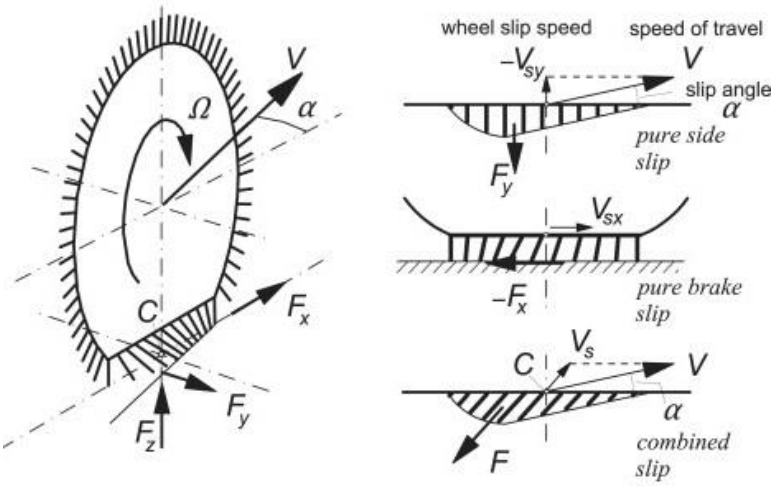

Figure 29: Above the tire tread deflection is shown during longitudinal, lateral, and combined slip maneuvers (Tire and vehicle dynamics, Pacejka, H., 2005, used with the permission of Elsevier)

There are two representations for the LuGre model: the lumped version, and distributed version. Both versions are discussed to explore their characteristics. The lumped LuGre model is denoted as:

$$F_x = \left(k_{tx} z + c_{tx} \dot{z} + c_v v_r\right) F_z \tag{141}$$

Where *z* is the brush deformation, k_{tx} is the tire tread longitudinal stiffness, c_{tx} is the tire tread longitudinal damping, c_v is the viscous relative damping, and $v_r = r\omega - v$ is relative velocity. The brush deformation that is equivalent to tire tread deformation can be calculated using the following differential equation:

$$\dot{z} = v_r - \frac{k_{tx}|v_r|}{g(v_r)} z \tag{142}$$

With:

$$g(v_r) = \mu_c + (\mu_s - \mu_c) e^{-|v_r/v_s|^{\alpha}} \tag{143}$$

Where μ_c is the normalized coulomb friction, μ_s is the normalized static friction, v_s is the Stribeck relative velocity, and α is a constant that is used to capture the steady-state friction force behavior.

For the distributed LuGre model the bristle deflection at a point λ of the contact patch is described using the following differential equation:

$$\frac{dz(\lambda,t)}{dt} = v_r(t) - \frac{k_{tx}|v_r|}{g(v_r)} z(\lambda,t) \tag{144}$$

The differential of bristle deflection can be written as:

$$dz(\lambda,t) = \frac{\partial z(\lambda,t)}{\partial \lambda} d\lambda + \frac{\partial z(\lambda,t)}{\partial t} dt \tag{145}$$

Rearranging this equation yields:

$$\frac{\partial z(\lambda,t)}{\partial t} = \frac{dz(\lambda,t)}{dt} - \frac{\partial z(\lambda,t)}{\partial \lambda}\frac{d\lambda}{dt} = \frac{dz(\lambda,t)}{dt} - r|\omega|\frac{\partial z(\lambda,t)}{\partial \lambda} \tag{146}$$

Substituting $\frac{\partial z(\lambda,t)}{\partial t}$ into the initial partial differential equation yields to:

$$\frac{\partial z(\lambda,t)}{\partial t} = v_r(t) - \frac{k_{tx}|v_r|}{g(v_r)} z(\lambda,t) - r|\omega|\frac{\partial z(\lambda,t)}{\partial \lambda} \tag{147}$$

For the combined slip situation that tire slip relative to the ground in both longitudinal and lateral directions, the bristle deflection dynamic is captured using following set of equations:

$$\begin{cases} \dfrac{\partial z_x(\lambda,t)}{\partial t} = v_{rx}(t) - \dfrac{k_{tx}|v_r|}{g(v_r)} z_x(\lambda,t) - r|\omega| \dfrac{\partial z_x(\lambda,t)}{\partial \lambda} \\ \dfrac{\partial z_y(\lambda,t)}{\partial t} = v_{ry}(t) - \dfrac{k_{ty}|v_r|}{g(v_r)} z_y(\lambda,t) - r|\omega| \dfrac{\partial z_y(\lambda,t)}{\partial \lambda} \end{cases} \tag{148}$$

These equations can be discretized in space for a finite number of bristles *N*:

$$\begin{cases} \dot{z}_{ix} = v_{rx}(t) - \dfrac{k_{tx}|v_r|}{g(v_r)} z_{ix}(\lambda,t) - r|\omega| \dfrac{N-1}{L} \left(z_{ix} - z_{(i-1)x} \right) \\ \dot{z}_{iy} = v_{ry}(t) - \dfrac{k_{tx}|v_r|}{g(v_r)} z_{iy}(\lambda,t) - r|\omega| \dfrac{N-1}{L} \left(z_{iy} - z_{(i-1)y} \right) \end{cases} \qquad i = 2,...,N \tag{149}$$

Where z_{ix} and z_{iy} are the horizontal and lateral deflections of the i^{th} bristle respectively, and *L* is the length of the contact patch.

5.5. Tire Contact with Deformable Terrain

Once a tire contact node hits deformable ground, it causes the ground to deform, and, consequently, stress distribution will appear at the contact patch. The generated stress field depends on the contact node velocity, angle of attack, and relative penetration into the ground in addition to the ground stiffness and damping. Different ground response scenarios that can happen based on the direction of the contact node velocity are shown in Figure 30. In order to understand the physics of the tire-terrain interaction systematically and characterize it more accurately, the terrain responses to normal and shear loadings are studied separately. In the following sections, the methods that are used in this study for representing the terrain response to various types of loadings are described.

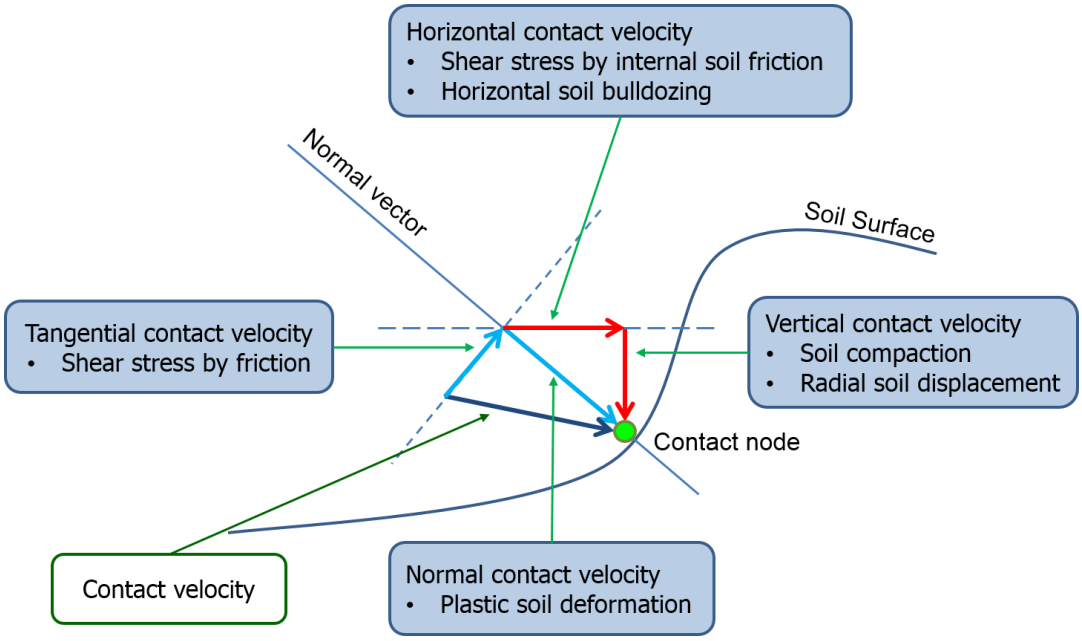

Figure 30: Terrain responses to tire loading depend on contact node velocity, angle of attack, and relative penetration into the ground surface.

5.6. Terrain Response to Normal Loading

When a tire is travelling over the terrain, a normal pressure distribution is generated in the tire contact patch normal to the tire-terrain interface. This pressure distribution amplifies the normal stress tensor in the soil levels that are closer to the surface. This makes the terrain surface deform accordingly, which causes the tire to sink into the ground. This behavior is represented using the pressure-sinkage relationships, which have different expressions for different terrains such as mineral, muskegs and snow-covered terrains. In this study the ground normal stress distribution formulation for mineral and snow covered terrains are implemented. The pressure sinkage relationship for the mineral terrains can be described using the equation that is initially proposed by Bekker [77, 78, 80]:

$$p = \left(k_c / b + k_\phi \right) z^n = k_{eq} \cdot z^n \tag{150}$$

Where p is the pressure distribution, b is the radius of the circular plate or the smaller dimension of a rectangular plate, z is the sinkage, and n, k_c, and k_j are the pressure-sinkage parameters which are calculated empirically. At every time step, the locations and the velocities of the tread elements are passed to the road model. Using this information and the terrain geometry, which was updated as well at the previous time step, the possibility of the contact is studied. In case of contact, the pressure distribution at the tire-terrain interface is calculated, and is applied to the tire, as well as to the ground. At equilibrium, the deformation of the tire and the soil sinkage reach their steady-state values and do not change considerably.

The surface of the mineral terrains can be covered with vegetation including grass, sedges, mosses, and low woody shrubs. This type of terrain is called muskeg. The fragile surface mat can break down if the applied pressure exceeds a critical pressure. The sinkage corresponding to the critical pressure is called critical sinkage, beyond which the resistance to penetration suddenly decreases. The surface mat under normal load usually fails due the lower levels of tensile strength compare to the shear strength.

In modeling the muskeg terrains the surface layer is idealized as a membrane structure, and the beneath peat as a spring that produces resistive force proportional to the vertical deformation. The general pressure-sinkage relationship for this type of terrain is:

$$p = kz_\circ + m_m z_\circ^2 \left(L/A\right) = kz_\circ + 4m_m z_\circ^2 \left(1/D_h\right) \tag{151}$$

Where k is the peat stiffness, $z_\circ$ is the critical sinkage, A and L are the area and perimeter of the loading area, and D_h is the hydraulic diameter of the plate and is equal to $4A/L$. The coefficient m_m is defined as:

$$m = \sqrt{kF_h / z_\circ^2} \tag{152}$$

With:

$$F_v / F_h = dz / dx \tag{153}$$

Where F_v and F_h are the vertical and longitudinal components of the tension force that exists in the surface mat. The k, m_m, and $z_\circ$ are influenced by the rate of penetration, loading plate shape, and plate size, and should be specified accordingly.

The mechanical properties of the snow-covered roads is different as compared to the mineral terrains. For the snow covered terrains, the pressure-sinkage characteristics would change slightly once the ice layer below the surface of the snow fails. It has been shown that the exponential relationship can represent the shape of the pressure-sinkage curves during the terrain loading [44]:

$$z = z_w \left[1 - \exp\left(- p / p_w \right) \right] \tag{154}$$

Where p is the pressure distribution, z is the sinkage, z_w and p_w are empirical parameters that depend on the structural properties of the snow. Therefore, different values of empirical parameters z_w and p_w for before and after ice layer failure should be identified. The following equations are used for curve-fitting these empirical parameters:

$$p_w = k_{p1} + r k_{p2} \tag{155}$$

$$z_w = k_{z1} + k_{z2} / r \tag{156}$$

Where r is the radius of the loading plate, and k_{p1}, k_{p2}, k_{z1}, and k_{z2} are the shape coefficients that are functions of the snow geometrical (depth) and physical properties.

5.6.1. Repetitive Loading

When a wheeled vehicle travels over a deformable terrain, the interface of the tire-terrain goes under deflection. Once the leading wheel of the vehicle passes, it unloads the terrain and consequently stresses are reduced. Due to hysteresis, the force-deflection path is different for loading and unloading situations. During reloading, the slope of the force-deflection curve is approximately similar to the one from the unloading step. The characteristics of the repetitive terrain load for a mineral terrain, also known as the multi-pass effect, is shown in Figure 31.

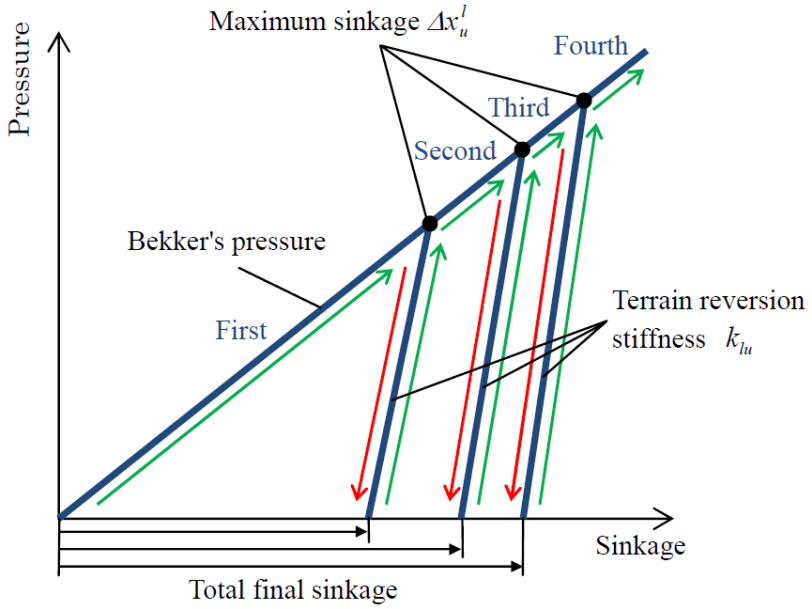

Figure 31: Soil response to tire repetitive loading known as multi-pass effect.

The pressure-sinkage relationship for a mineral terrain during loading and unloading can be described as:

$$p = \left(\frac{k_c}{b} + k_\phi\right) z_u^n - k_u\left(z_u - z\right) = k_{eq} z_u^n - k_u\left(z_u - z\right) = p_u - k_u\left(z_u - z\right) \tag{157}$$

The terrain stiffness k_u during unloading and reloading cycles is a function of unloading sinkage z_u:

$$k_u = k_\circ + A_u z_u \tag{158}$$

This equation can be used for the repetitive loading of muskeg terrains when z_u is less than the critical sinkage z_b. The terrain elastic sinkage z_e can be written as:

$$z_e = \left(\frac{\frac{k_c}{b} + k_\varphi}{k_\circ + A_u z_u} \right) z_u^n \tag{159}$$

5.7. Soil Damping

The damping behavior of the deformable terrain material during loading/unloading steps should be considered. The soil damping is particularly important when tire is considered as rigid during the simulation. In this type of situation, due to the lack of structural damping from the tire, the transient tire-terrain interaction should be damped out by the terrain model in order to have overall model stability. The following formulation is used to model the damping force from the terrain:

$$s_{damping} = \begin{cases} - C_{ng} v_n^{i,j} & if \quad v_n^{i,j} < 0 \quad and \quad contact = true \\ 0 \end{cases} \tag{160}$$

Where C_{ng} and $v_n^{i,j}$ are soil damping and velocity of the in contact tire element in a normal direction relative to the soil surface. The soil damping can be found using the formulation suggested by McCullough [130] as a function of soil shear deformation factor G, poison ratio υ, and tire contact area A_z:

$$C_{ng} = \frac{3.4 G A_z^2}{1 - \nu} \sqrt{G g} \tag{161}$$

In order to find the tire element velocity component normal to the ground surface, the terrain normal vector should be calculated. Consider the ground at the immediate point of the tire tread element contact having the constant slopes of dZ/dX and dZ/dY in the global X and Y directions respectively. The ground normal vector at this point is defined as:

$$t_z = \frac{n_z - \left(\frac{dZ}{dX}\right)n_x - \left(\frac{dZ}{dY}\right)n_y}{\left\| n_z - \left(\frac{dZ}{dX}\right)n_x - \left(\frac{dZ}{dY}\right)n_y \right\|} \tag{162}$$

Where n_x, n_y, and n_z are the unit vectors parallel to the global X, Y, and Z axes. The tire element velocity component normal to the ground surface is defined as $v^{i,j} \times t_z$.

5.8. Terrain Response to Shearing

The local shear behavior of the soil depends on the local slip velocity of the tire tread elements $\left(v_t^{i,j}\right)$, at the tire-terrain interface. The concept of the tire slip velocity on a deformable surface is similar to the one on a rigid surface. The slip velocity is the local tangential velocity of a tire tread element relative to the surface. In order to find this value the velocity vector of the tread element should be projected into the ground plane.

The projection of the tread element velocity $\left(v^{i,j}\right)$ on the ground plane that has the normal vector of t_z is given as:

$$v_t^{i,j} = v^{i,j} - \frac{v^{i,j} \cdot t_z}{\left\| t_z \cdot t_z \right\|^2} \cdot t_z \tag{163}$$

Then the shear displacement along the tire-terrain interface is defined as

$$\lambda_s = \sum_{i=1}^{N_{Belt\_seg}} \sum_{j=1}^{N_{belt\_elm}} v_t^{i,j} \tag{164}$$

Previously, the pressure-sinkage characteristics during normal loading conditions were characterized for different types of loading curve shapes corresponding to different terrain types including mineral, muskeg, and snow covered terrains. Similarly, these terrains exhibit unique shear stress-displacement behavior that needs to be formulated separately. For mineral terrains, the shear stress increases with shear displacement, and approaches a constant value. Using the Janosi and Hanamoto's approach, the shear stress distribution at the contact patch is described as:

$$\tau \Big/ \tau_{\max} = \left(1 - e^{-\lambda_s / k}\right) \tag{165}$$

Where $\tau_{\max}$ is the maximum shear stress, and K is the shear deformation parameter, which identifies the magnitude of the shear displacement required for the development of the maximum shear stress. This values is calculated from the measurement data:

$$K = -\frac{\sum\left(1 - \tau \Big/ \tau_{\max}\right)^2 \lambda_s^2}{\sum\left(1 - \tau \Big/ \tau_{\max}\right)^2 \lambda_s \left[\ln\left(1 - \tau \Big/ \tau_{\max}\right)\right]} \tag{166}$$

The maximum shear stress $\tau_{\max}$ is defined using the Mohr-Coulomb equation:

$$\tau_{\max} = \left(c_a + p \tan\phi\right) \tag{167}$$

Where p is the normal stress, ϕ is the angle of shearing resistance, and c_a is the soil cohesion (or adhesion). Similarly, a discretized version of shear stress equation is implemented in the model, which is used for integrating the stress field over the tire-ground contact patch and calculating the shear forces.

The shear curve of the muskeg terrains exhibit a maxima and then the shear stress decreases continually with the increase of the shear displacement. This behavior is described as:

$$\tau \Big/ \tau_{\max} = \left(\lambda_s \Big/ K_w\right) \exp\left(1 - \lambda_s \Big/ K_w\right) \tag{168}$$

The value of K_w is obtained by solving the following equation:

$$\sum\left(\tau/\tau_{\max}\right)^2\left[\ln\left(\tau/\tau_{\max}\right)-\left(1+\ln\left(\lambda_s/K_w\right)-\lambda_s/K_w\right)\right]\left[K_w-\lambda_s\right]=0 \tag{169}$$

As for the snow-covered terrains, the shear curve displays a maxima and then decreases to an asymptotic value. In this case, the shear stress behavior is computed as:

$$\tau/\tau_{\max}=K_r\left[1+\left[\frac{1}{K_r(1-1/e)}-1\right]\exp\left(1-\lambda_s/K_w\right)\right]\left[1-\exp\left(-\lambda_s/K_w\right)\right] \tag{170}$$

Furthermore, using the Mohr-Coulomb equation is adequate for describing the maximum shear stress $\tau_{\max}$ in this equation.

5.9. Results and Discussion

The mathematical formulations for modeling the terrain behavior on non-deformable and deformable terrains were described in previous sections. The developed models are implemented in the HSSTM package. During the simulation of tire on non-deformable terrains, the terrain model provides the tire model with forces and moments at the center of the contact patch. On the other hand, on deformable terrains, the terrain model inputs the normal pressure and shear pressure distribution across the contact patch to the tire model. At the same time, the terrain model calculates the elastic and plastic terrain deformations, and updates the terrain profile respectively. In order to validate the performance of developed terrain models, a series of simulations are conducted on various terrain types, and with different simulation input conditions. The results are provided in the following sections, and discussions are made on the accuracy of the models.

5.9.1. Non-Deformable Terrain Model

In order to find the required parameters for the non-deformable terrain model, the experimental data described by the Magic Formula are used. The required Magic Formula parameters are

adopted from the literature [5, 129]. The tire force and moments are replicated using the parameterized magic formula equations. Next, the longitudinal and lateral force vs. slip curves are used to capture the normalized coulomb friction μ_c, normalized static friction μ_s, Stribeck relative velocity v_s, and steady-state friction force constant a used in the LuGre friction function:

$$g(v_r) = \mu_c + (\mu_s - \mu_c) e^{-|v_r/v_s|^a} \tag{171}$$

The process of curve-fitting is conducted using a nonlinear least-square fitting method. The parameterized friction function $g(v_r)$ is incorporated in the developed distributed LuGre model to calculate the time dependent brush deformation in longitudinal and lateral directions. As it was mentioned earlier, each of the contact brushes is attached to belt nodes. Therefore, the final deformation of the brushes relative to ground depends on the brush stiffness as well as tire sidewall and belt stiffness values in longitudinal and lateral directions. Consequently, in order to estimate contact patch shear forces the parameters for brush model and tire structure model should be identified simultaneously. This procedure is described in detail in Chapter 7.

5.9.2. Deformable Terrain Model

As it was mentioned earlier, the semi-empirical formulations for various types of terrains are implemented in the terrain model using an incremental approach. This, in addition to the three-dimensional RGR road profile representation, allows a wide variety of tire maneuvers to be simulated using the terrain model. Initially, the terrain pressure-sinkage behavior is studied using a pressure plate loading simulation. During this test, different flat terrain profiles are undergone loading/unloading with a rectangular plate that its vertical position varies sinusoidally. The amplitude of the plate vertical displacement increases linearly with time as well. The pressure-sinkage characteristics of two mineral terrains during the aforementioned loading/unloading cycle

are shown in Figure 32. The mechanical terrain properties of mineral terrains that are used for conducting the simulations are described in Table 10.

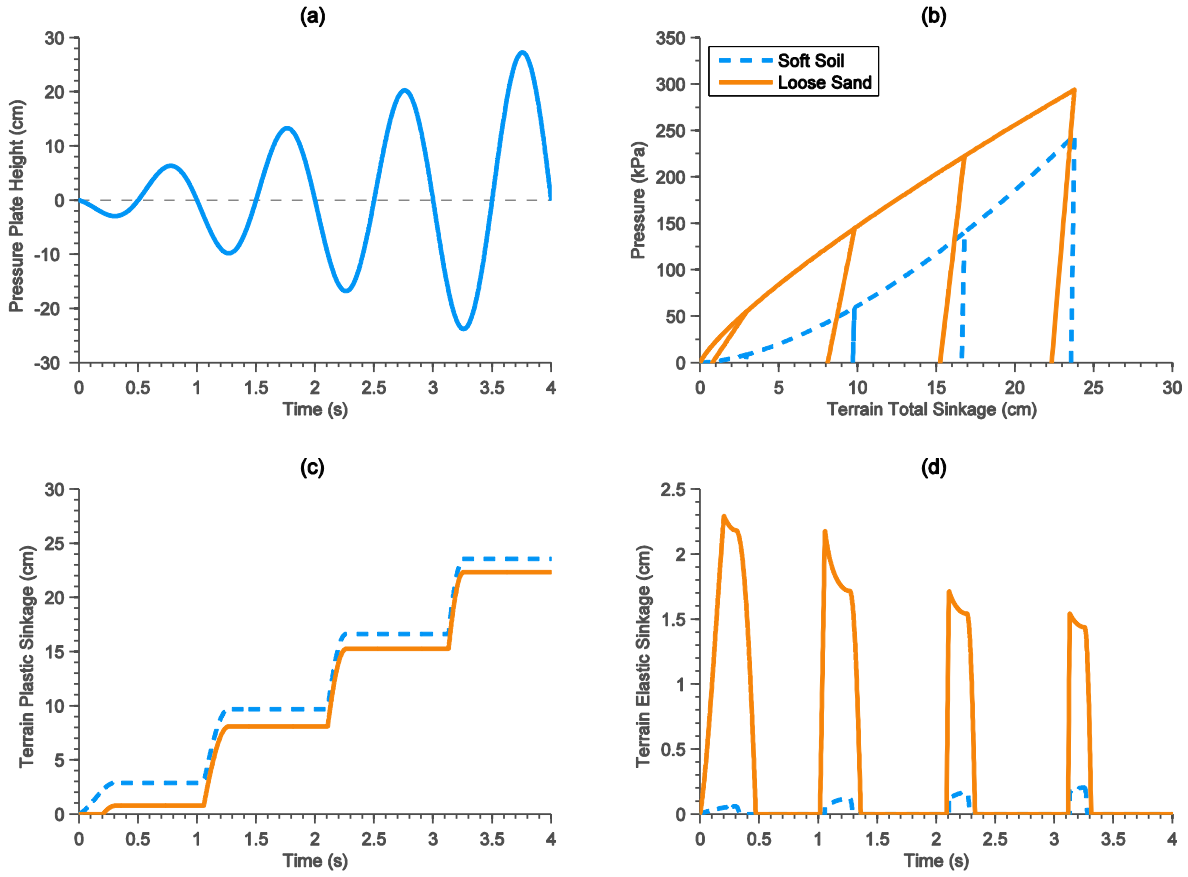

Figure 32: Plate pressure loading of mineral terrains (a) pressure plate height (b) terrain pressure vs. sinkage (c) terrain plastic sinkage time history (d) terrain elastic sinkage time history

Table 10: Mechanical properties of mineral terrains used in simulations

	Normal pressure			Repetitive loading		Shear stress (rubber-terrain)		
Terrain Type	n (–)	K_c $\left(\frac{kN}{m^{n+1}}\right)$	K_ϕ $\left(\frac{kN}{m^{n+1}}\right)$	K_o $\left(\frac{kN}{m^{n+1}}\right)$	A_u $\left(\frac{kN}{m^{n+1}}\right)$	C $\left(\frac{kN}{m^{n+1}}\right)$	Φ (deg)	K (–)
Soft soil	1.6	225.14	2216	0	503000	1.15	31.5	-
Loose sand	0.8	16.54	911.4	0	86000	2.7	26.1	0.45

The overall terrain pressure-sinkage curve follows the trend that was discussed in Figure 31. Every time the plate displacement goes below the initial flat terrain profile, the terrain pressure-sinkage follows the nonlinear loading path. Upon unloading the terrain, the pressure would decrease from the local maximum unloading pressure linearly to zero. The slop of the unloading/reloading line depends on the maximum unloading pressure, so it changes for each unloading cycle. The sinkage corresponding to the zero unloading pressure is terrain plastic sinkage. During the reloading, when loading plate goes below the plastic sinkage level from the previous unloading stage, terrain pressure increases through the unloading/reloading linear line until it reaches the local maximum unloading pressure from the last unloading step. Beyond this point, the pressure increase will follow the nonlinear loading patch again until the next unloading step is initiated.

Furthermore, the formulation for non-mineral terrains is included in the terrain model as well. Figure 33 shows the pressure sinkage behavior of muskeg and snow terrains during the plate loading simulations. The parameters used for characterizing the models for these terrains are included in Table 11 and Table 12.

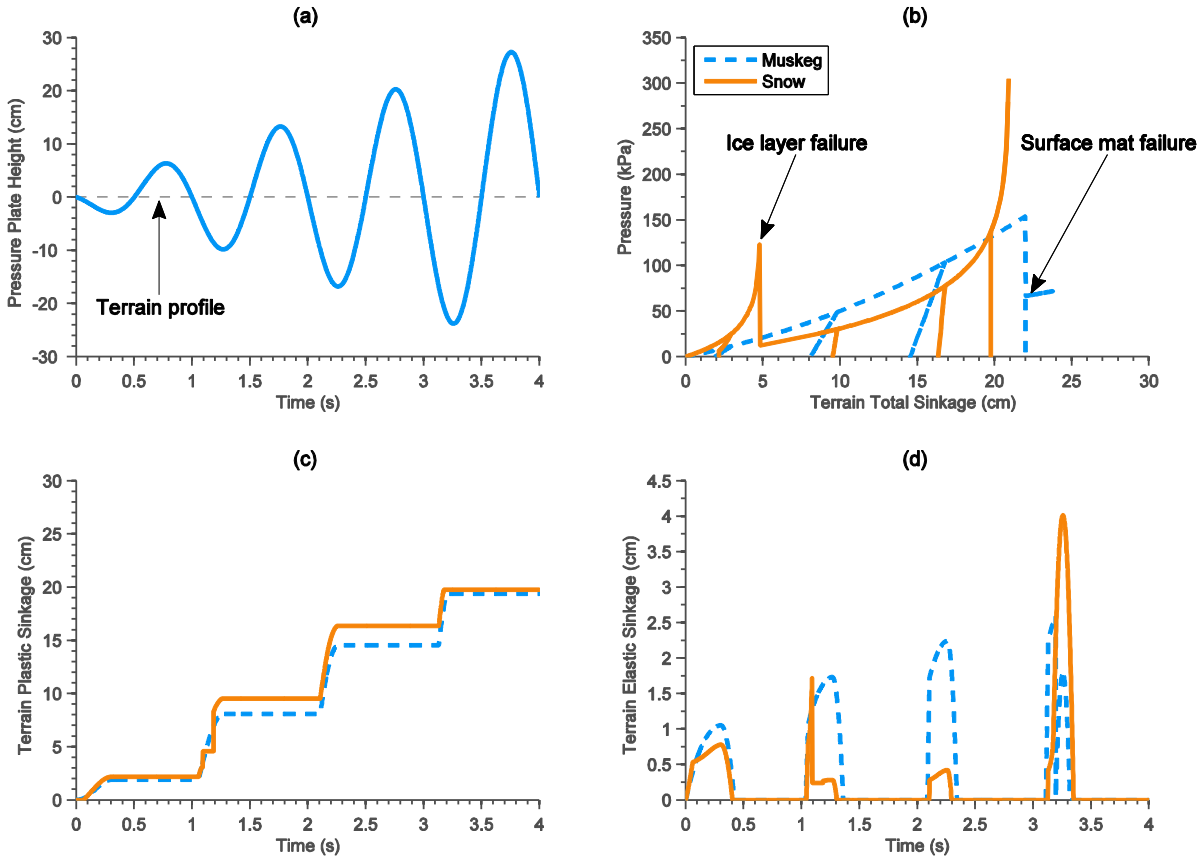

Figure 33: Plate pressure loading of non-mineral terrains (a) pressure plate height (b) terrain pressure vs. sinkage (c) terrain plastic sinkage time history (d) terrain elastic sinkage time history

Table 11: Mechanical properties of muskeg terrain used in simulations

	Normal pressure				Repetitive loading		Shear stress (rubber-mat)		
Terrain Type	k $\left(\frac{kN}{m^3}\right)$	m_m $\left(\frac{kN}{m^3}\right)$	z_b (cm)	Peat Stiff. $\left(\frac{kN}{m^3}\right)$	K_o $\left(\frac{kN}{m^{n+1}}\right)$	A_u $\left(\frac{kN}{m^{n+1}}\right)$	C $\left(\frac{kN}{m^{n+1}}\right)$	Φ (deg)	K (–)
Petawawa Muskeg	338	53	22	302	334	25430	1.7	40.3	0.9

Table 12: Mechanical properties of snow covered terrain used in simulations

Terrain Type	Normal pressure				Repetitive loading		Shear stress (rubber-snow)		
	k_{p1} (kPa)	k_{p2} $\left(\frac{kPa}{cm}\right)$	k_{z1} (cm)	k_{z1} (cm^2)	K_o $\left(\frac{kN}{m^{n+1}}\right)$	A_u $\left(\frac{kN}{m^{n+1}}\right)$	C $\left(\frac{kN}{m^{n+1}}\right)$	Φ (deg)	K (–)
Petawawa Snow (before ice layer failure)	3.18	2.34	0.85	39.69	0	109600	0.16	17	0.34
Petawawa Snow (after ice layer failure)	52.71	-0.48	14.21	67.34	0	109600	0.16	16.1	0.35

The process of loading the muskeg terrain is different than for the mineral terrains. The muskeg consists of a surface layer of fibrous composition and an underlying peat layer. The surface layer is idealized as a membrane-like structure that can sustain a certain level of sinkage. Once the sinkage passes this critical point, the surface mat will fail. The underlying peat is assumed to have a resistance proportional to its vertical deformation. As a result, once the surface mat layer fails, the pressure suddenly drops, and then increases linearly upon loading the terrain further with the loading plate. This behavior is correctly captured in simulation results shown in Figure 33. It should be mentioned that the unloading/reloading characteristics of the muskeg is similar to that of mineral terrains.

During the loading of the snow-covered terrains, the terrain pressure increases gradually until the lower boundary of the deformation zone of the snow under the plate reaches the underlying ice layer. At this point, terrain pressure increases rapidly, and after a certain pressure level ice layer fails. After fracture of the ice layer, further penetration of the plate into the snow beneath the ice layer causes the pressure to increase gradually again. This trend continues until plate approaches

the frozen ground at the base of the snow layer. Then, the pressure increases rapidly again, and the pressure-sinkage curve approaches an asymptotic line, as shown in Figure 33 (b).

To validate the normal pressure and shear stress distribution across the contact patch of a driven wheel, the performance of a rigid wheel with a diameter of 1245 mm and a width of 305 mm was simulated on the loose sand, and compared with the experimental data reported by Onafeko [131]. The simulation results for a vertical load of 9.28 kN, and two slip ratio values of 3.1% and 22.1 % are reported in Figure 34. The normal pressure and shear stress values are plotted against the polar coordinate (θ) starting beneath the tire center increasing in a counter clockwise direction. The developed terrain model provides promising estimations compared to experimental data. It can be seen that by increasing the tire slip ratio, the peak of the normal and shear stress curves shifts toward the front of the contact patch in the direction of moving. At the same time, the maximum value of the normal pressure decreases while the shear stress increases. This is caused by the soil flow in the contact patch that increases as the tire travels with a higher slip ratio value.

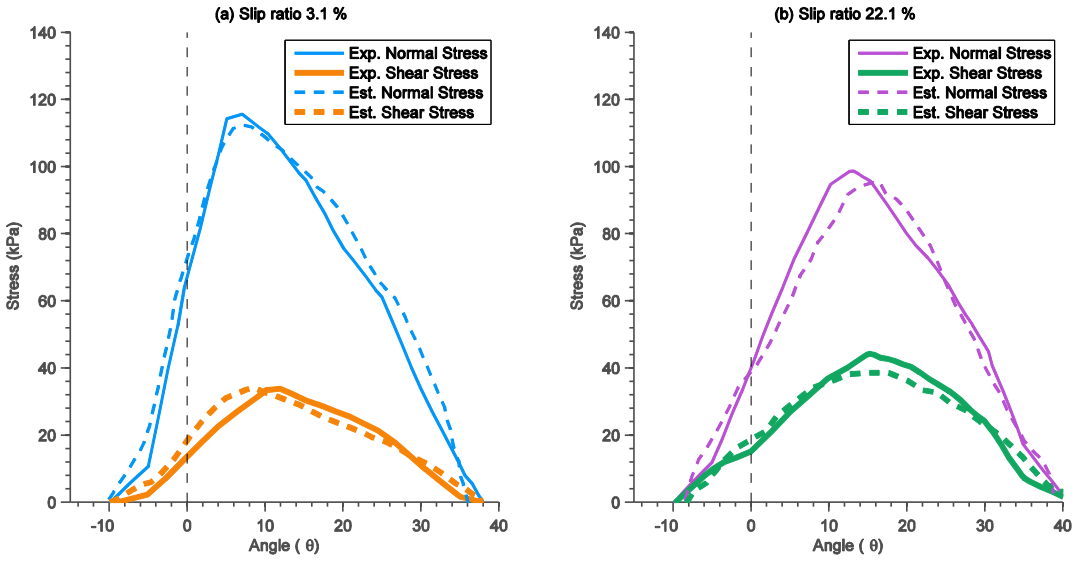

Figure 34: Comparison of experimental and estimated normal and shear stress across the tire contact patch (a) slip ratio 3.1 % (b) slip ratio 22.1 %

5.10. Conclusion

The computational models used in the Hybrid Soft Soil Tire Model (HSSTM) terrain model for evaluating the interaction of the tire with deformable and non-deformable terrains are described. Initially, a contact search algorithm searches for tire nodal points that are close to the ground and detects the penetration of the contact surfaces. Next, the contact interface algorithm applies the contact constraints to minimize or eliminate penetration. The contact interface algorithm for non-deformable terrains is implemented using two different methods: 1) a single point contact model based on Magic Formula enhanced with a relaxation length module for dynamic manoeuvres and 2) a distributed three-dimensional (3D) brush model. The contact interface algorithms for deformable terrains are based on the semi-empirical formulations for various terrain types that are implemented using an incremental approach in a 3D scheme.

The terrain response to tire inputs for deformable surfaces was handled for normal and shearing loadings separately. For the normal direction, the repetitive loading of the terrain that causes the terrain to react differently in consecutive passes was accounted for. The corresponding formulation was given for various deformable surfaces including mineral, muskeg, and snow-covered terrains. Both contact algorithms are incorporated in HSSTM package to simulate the tire-terrain interaction during different manoeuvres with an explicit approach.

Chapter 6: Experimental Study

6.1. Introduction

Experimental studies are necessary to parametrize and validate the tire model developed. The required parameters for tire and terrain models should be determined individually. The terrain model is parametrized using the geotechnical data available for different types of terrains [44]. The parameters for tire materials models are identified using two different approaches. The in-plane stiffness and damping values are calculated using the modal analysis tests and plate loading. The out-of-plane stiffness and damping values are estimated using the flat track machine data, as well as virtual tests conducted with a validated FEM tire model [51].

Moreover, the tire interaction with the deformable terrain is studied at the terramechanics test rig. The tire is mounted on a carriage, representing the quarter car rig model, and is moved over the soil. The test inputs conditions are controlled at different levels and the outputs are recorded. The experimental results from these tests are used to validate the tire model. The detailed description of the experimental setup is given in the following sections.

6.2. Modal Analysis Test Setup

The modal analysis test is performed in order to extract tire mode shapes and associated natural frequency and damping values. These values are directly used for parameterization of the HSSTM tire model. The schematic of the test rig that is typically used for conducting the radial modal analysis experiments on the tire is illustrated in Figure 35. The tire is hanged from a steel structure by cords to avoid effect of the mounting structure on the vibrational characteristics of the tire. The tri-axis accelerometers are attached to ten equally spaced locations on the tire surface with heated

beeswax. The employed accelerometers are small, so they would not change the structural characteristics of the tire at the installation location.

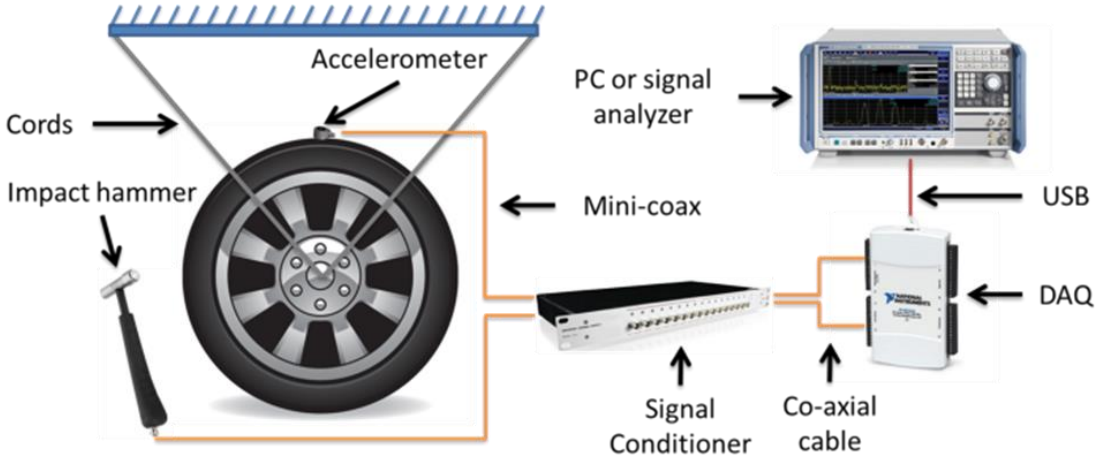

Figure 35: The modal analysis test rig schematic for extracting the tire natural frequencies and damping values. These values are used accordingly to parameterize the tire material model.

The tire is excited with an impulse force generated by an instrumented handheld hammer. In order to achieve accurate estimations for the frequency response functions, the input energy to the tire should be uniformly distributed over the frequency range of interest. To achieve this ideal input excitations, a plastic material used as the tip of the hammer, and a piece of aluminum is mounted on the tire at the impact location. The signals from the hammer force transducers and accelerometers are amplified by a signal conditioner to reach the voltage levels that can be detected by the data acquisition system.

As for the tire radial model shapes, the experimental data from the Tire Model Performance Test program (TMPT) is adopted. The TMPT program introduces a standard set of test procedures to evaluate the performance of the tire models in conjunction with multibody system (MBS) vehicle models. These tests are divided into model capability tests and validation tests. The capability tests are designed to study the qualitative behavior of the tire, and show the physical plausibility of using the model. The validation tests contain the experimental test results for some

steady-state and dynamic measurements [132]. It should be noted that similar definitions and arrangements for principal axis and force measurements are considered as the basis for constructing the current FEM model.

For the tire torsional modes, the modal analysis data from the modal test rig at University of Pretoria is incorporated. The test setups for unconstrained and constrained tire configurations are shown in Figure 36. The Michelin LTX 235/85R16 tire is mounted horizontally on a hub with the UP VDG Wheel Force Transducer and KMT telemeter. A 100 kN hydraulic actuator with a 100 kN load cell is mounted horizontally. The tests are aimed at determining the frequency of the torsional modes of the test tire at different inflation pressures. The modes are determined for a free rotation tire at an inflation pressure of 0, 100 and 200 kPa. Additional tests are conducted with the tire preloaded/constrained at 5, 20 and 30 mm tire deflection at the same inflation pressures as for the free rotating wheel, as shown in Figure 36 (a).

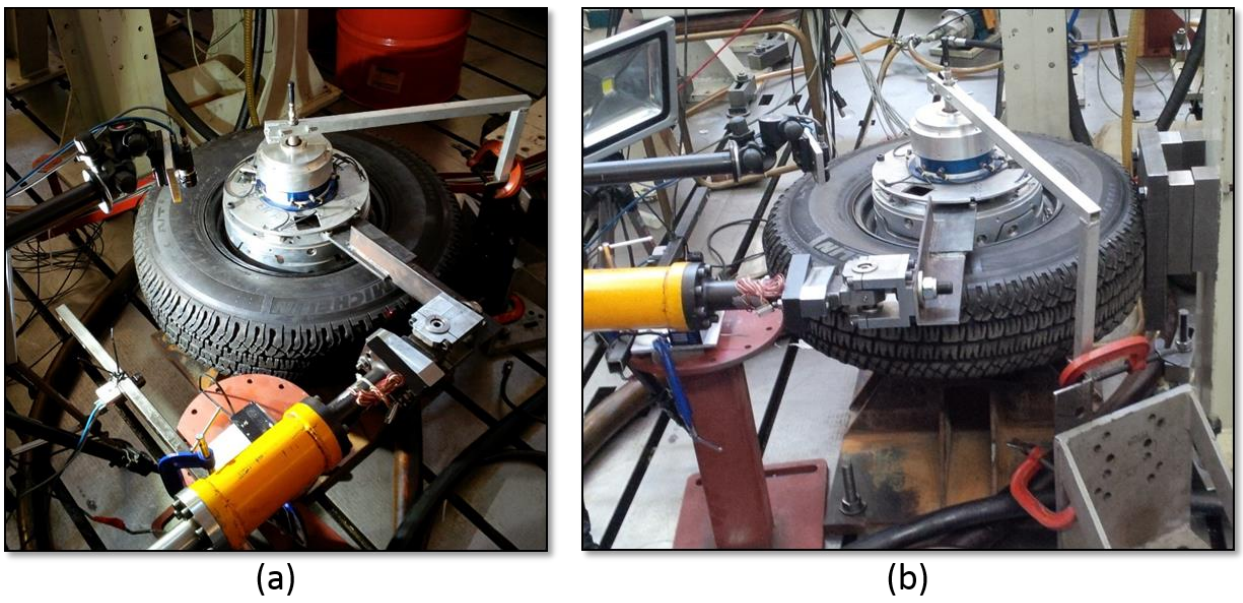

Figure 36: The modal analysis test rig at University of Pretoria; (a) setup for unconstrained tire (b) setup for constrained tire

High-speed cameras were used to record the movement of the tire at 250 Hz. One camera was positioned perpendicular to the tread pattern. A second camera was positioned perpendicular to the sidewall. During the constrained tests, the sidewall movement was captured in the constrained and the unconstrained areas. A trigger channel was generated to synchronize the photographs with the sampling frequency of the data acquisitioning system.

Figure 37: Camera view for the (a) tire tread camera (b) tire sidewall camera

The actuator is controlled in displacement mode and supplied with a sinusoidal signal with 1 mm amplitude. The frequency of the sinusoidal input is swept from 0 to 40 and 45 Hz for the free rotating wheel and preloaded tests respectively. For each test setup 3 runs are conducted per test file. The first run was a slow sweep from 0 to 40 or 45 Hz. The second run is a fast sweep from 15 to 40 or 45 Hz. The third run is a slow sweep from 15 to 40 or 45 Hz. The frequency sweeps are conducted by hand on the actuator controller at an average sweep rate of 1.5 Hz/sec and 0.15 Hz/sec for the fast and slow sweeps respectively. An Acuity AR700-RP laser (SN) is used to measure the rotational displacement of one of the tread blocks.

The processed natural frequency and damping values from the radial and torsional modal analysis test studies are presented in Chapter 7.

6.3. Quasi-static Loading Test

The cleat test experimental data used for studying the tire radial behavior is courtesy of the Vehicle Dynamics Group at the University of Pretoria, S. Africa, led by Professor Schalk Els. The tests were aimed at characterizing the vertical stiffness of the Michelin LTX 235/85R16 tire on a flat plate and for various cleats at 100 kPa and 200 kPa tire gauge pressure at 0°, 3° and 6° camber. The test tire was mounted on a pedestal with the UP VDG Wheel Force Transducer and KMT telemetry. A 16 kN hydraulic actuator with a 20 kN load cell was mounted horizontally. A single test at 0 kPa tire gauge pressure at zero camber was done with a flat plate to characterize the tire carcass stiffness with no air in the tire. A road profiling laser was mounted on the wheel load cell to measure the displacement of the plate or cleat pressing the tire. A camera was used on some of the tests to record the deformation of the tire. A trigger channel was generated to synchronize the photographs with the sampling frequency of the data acquisitioning system.

Two sets of tests were performed, at 100 kPa and 200 kPa tire gauge pressure and 0°, 3° and 6° camber. The first set of tests was on a flat glass plate to determine the tire's vertical stiffness as a function of displacement. A camera was mounted beneath the glass plate to determine the contact patch shape and area. The image from the camera is used to construct the Bitmap image of the contact patch. A ruler is placed near the contact patch area for scaling the image to proper dimensions during the post-processing. The contact patch area is calculated from this image, as shown in Figure 38. The comparison between the estimated contact patch area values at different camber angles and experimental results is made in the next chapter.

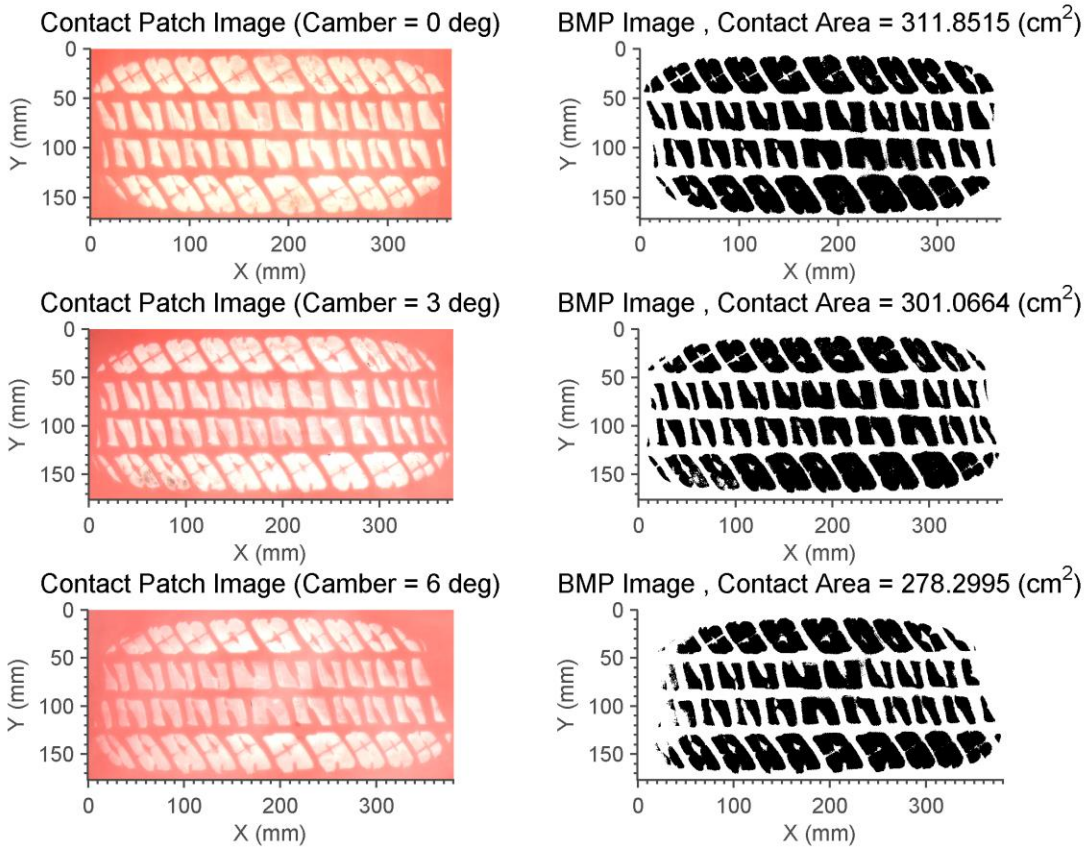

Figure 38: (Left) tire contact patch image at different camber angles (Right) corresponding Bitmap image with the calculated contact area

The second set of tests was conducted on 25 mm and 32 mm cleats mounted on a flat steel plate. The cleats were mounted transversely, longitudinally and at a 45° angle, as shown in Figure 39. The quasi-static cleat test data is used for tire model parameter estimation in radial direction and model validation. This procedure is elaborated in Chapter 7.

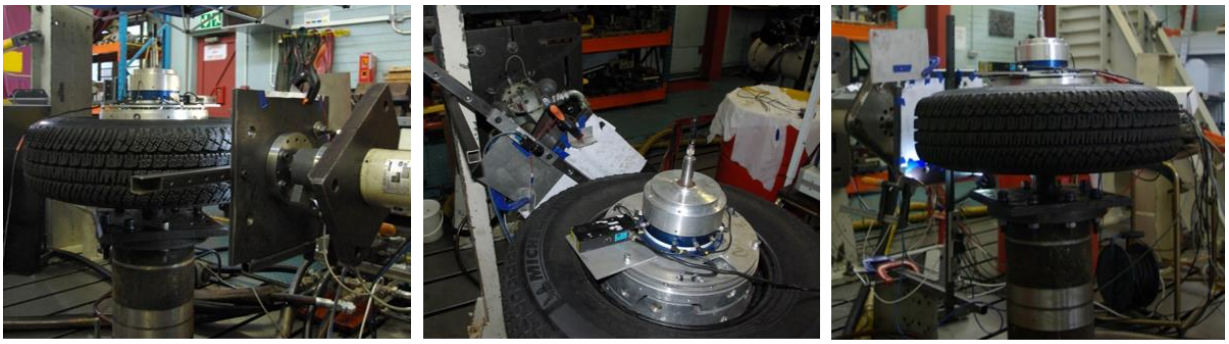

Figure 39: Quasi-static cleat test at different cleat orientations (a) longitudinal (b) 45° orientation (c) transverse

6.4. Off-road Experimental Test Setup

For the off-road conditions, the experimental work has been performed on an indoor single-wheel Terramechanics Rig at Advanced Vehicle Dynamics Laboratory (AVDL). The test rig was developed to investigate wheel interaction with various terrains under a well-controlled environment, essentially the terramechanics of a loaded wheel. This test rig can accommodate different terrains such as mineral terrains and ice. The rig provides a well-controlled environment to assure repeatable testing conditions, and is presented in Figure 40. The test rig is filled with a sandy loam soil, which is a combination of different percentages of clay, silt and sand. The composition of the tested soil is shown in Figure 41.

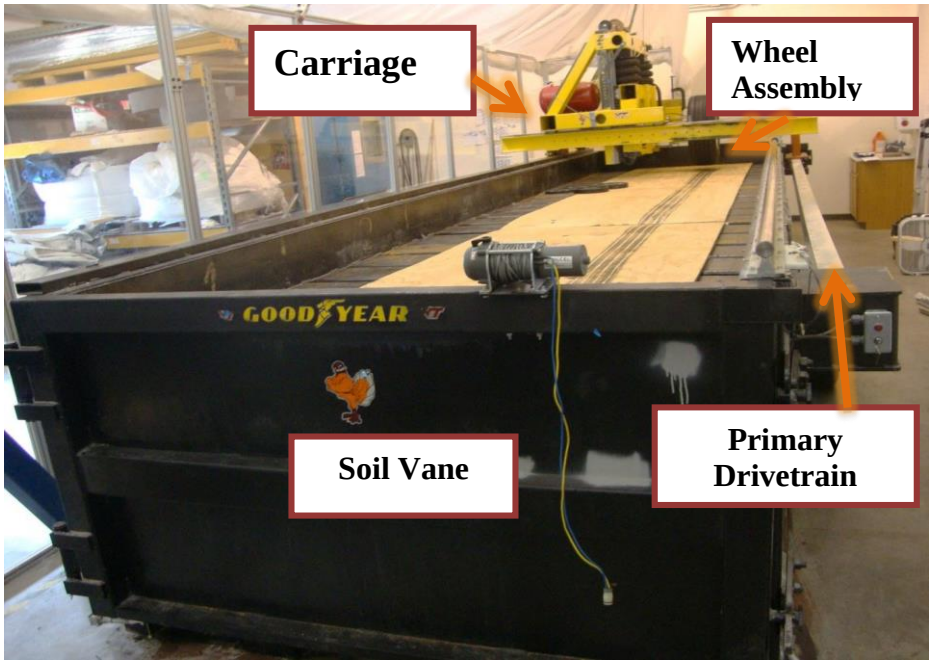

Figure 40: The Terramechanics test rig in Advance Vehicle Dynamics Laboratory (AVDL) at Virginia Tech.

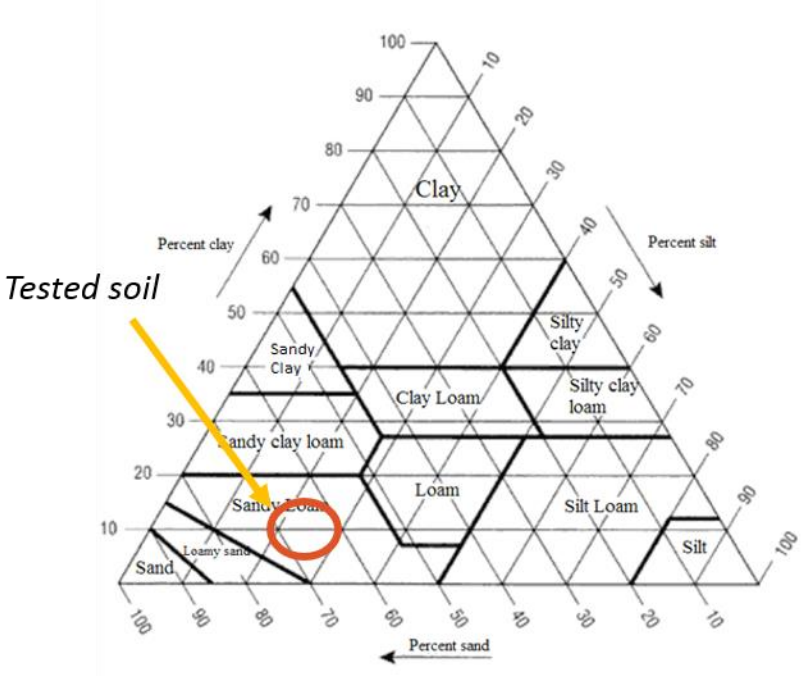

Figure 41: The sandy loam soil used in terramechanics rig for conducting the experiments

The carriage of the rig represents the quarter-car model of a vehicle. The close view of the wheel carriage of the test rig is shown in Figure 42. All the three forces and three moments at the tire spindle are measured using a Kistler wheel hub sensor. The methodical soil preparation procedure implemented in order to rendered data used to analyze the tire tractive performance.

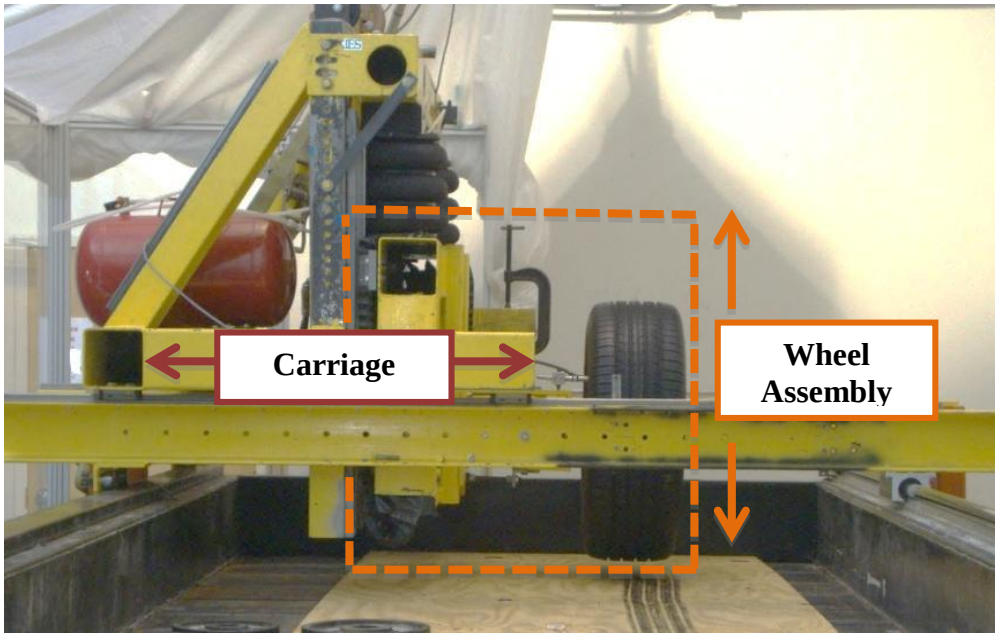

Figure 42: The wheel carriage of the test rig (close view)

A wireless sensory system that measures tire deflection at the contact patch has been developed; combining this system with other sensors allowed accurate estimations of wheel sinkage. The rig has active normal load control to keep wheel load variation at less than 3% difference from the target value. The load is applied with two pneumatic air springs that vary in air pressure and is controlled with an electro-pneumatic control valve that can hold several open and close positions proportional to an input voltage signal. Input from the wheel hub sensor is used in the normal load control system. Additionally, the rig was developed to fit several tire sizes that can be set to ±25˚ in toe and from 0˚ to 6˚ in camber angle.

The preliminary set of tests is standard measurement tests, in which tire general information, such as its overall geometry, section geometry, moment of inertia about the three axes, and individual tire component weights are measured. The tire used for tests in this study is a Michelin LTX P235/85 R16 Radial Reference Test Tire. This is a standard tire used by many tire researchers, and its properties, in addition to some static and dynamic test data are available. The dynamic loading radius of the tire is measured using the optical distance measuring sensors implemented inside the tire. Footprint of the tire on a flat rough surface is measured through pressure pads, and the stiffness of the tire in radial direction is obtained from tests for which the tire is loaded using hydraulic shakers and vertical reaction forces are measured through the force hub at the tire spindle in the Terramechanics rig [9, 109, 133, 134].

Because the initial version of the tire model developed in this study did not consider the tread, one of the test tires was buffed. This buffed tire is used for conducting the experiments, and as the reference geometry for developing a finite element tire model.

6.5. Outdoor Off-road Testing

The outdoor off-road test are conducted using the Center for Tire Research (CenTiRe) mobile tire test trailer seen in Figure 43. The test rig is equipped with a 3-axis force and moment measurement system at the wheel center. The normal load is actively controlled with an air spring system capable of applying up to 9000 lbs vertical load. The camber angle sweeps from -16 to 16 deg, and slip angle changes between -30 to 30 deg are possible. The outdoor test trailer accommodates high speed testing up to 70 mph. Furthermore, an onboard 500 gallon tank provides wet testing capability.

Figure 43: (a) test rig housing is attached to a tow vehicle that has a generator for power supply (b) test rig setup

The tire test trailer is a robust, standalone system capable of traversing smooth and rough surfaces under dry and wet conditions. The testing trailer was designed to test tires ranging from small passenger and motorcycle tires up to large semi-truck tires [135]. The data acquisition system for the trailer is shown in Figure 44.

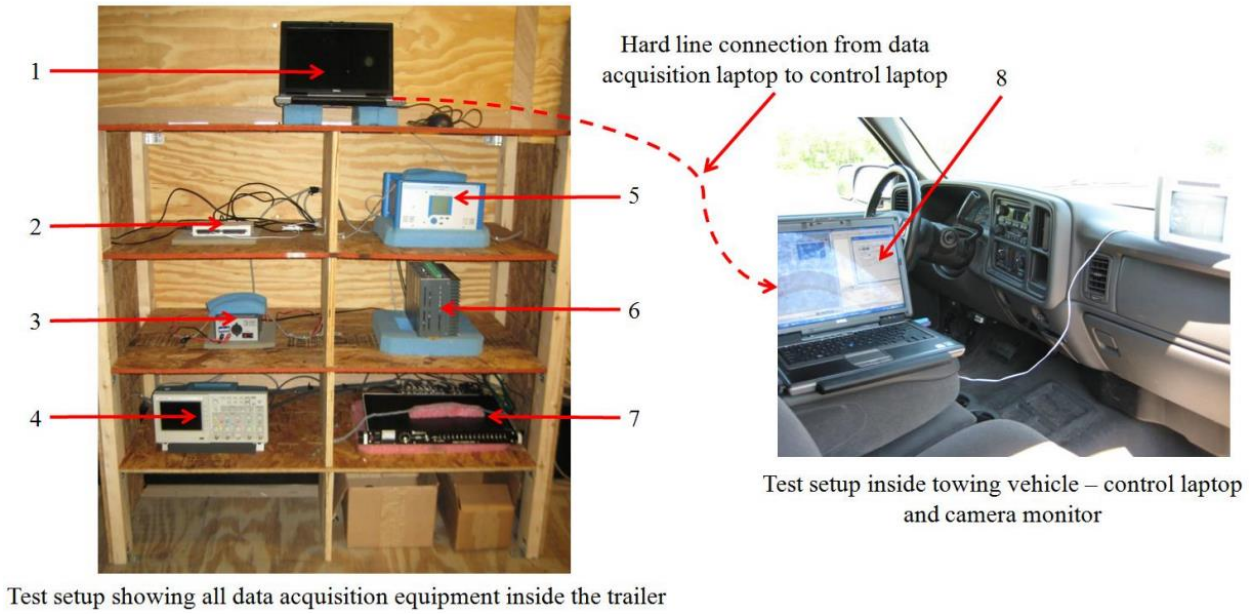

Figure 44: The data acquisition system for tire test trailer

The list of test setup instruments shown in Figure 44 includes:

1. Laptop responsible for collecting and storing all data processed through LabView
2. National Instruments data acquisition board (NI USB 6212)
3. DC Voltage regulator to supply constant power to dSpace data acquisition unit
4. dSPACE Micro Auto Box data acquisition unit (DS 1401/1501)
5. Kistler power amplifier
6. Steering servo motor controller
7. 16-channel power source for the tire sensors (Dytran 4116)
8. Remote laptop for user control of data acquisition laptop and all control equipment

For performing the outdoor testing, a wooden container is constructed to carry the test soil. This structure has 30 feet length, 3 feet width, and 10 inches height. A commercial gardening soil is used for testing which is similar to sandy loam in texture, and has a combination of sand, silt and clay. The test maneuvers are conducted in a straight line with 5 different slip angles, and two tire inflation pressure values. During the tests, tire normal load is controlled at 1200 N, and forces and moments are measured at the wheel center. Tire longitudinal velocity is recorded with a V-Box GPS data logger, and tire rotational position is captured using an encoder.

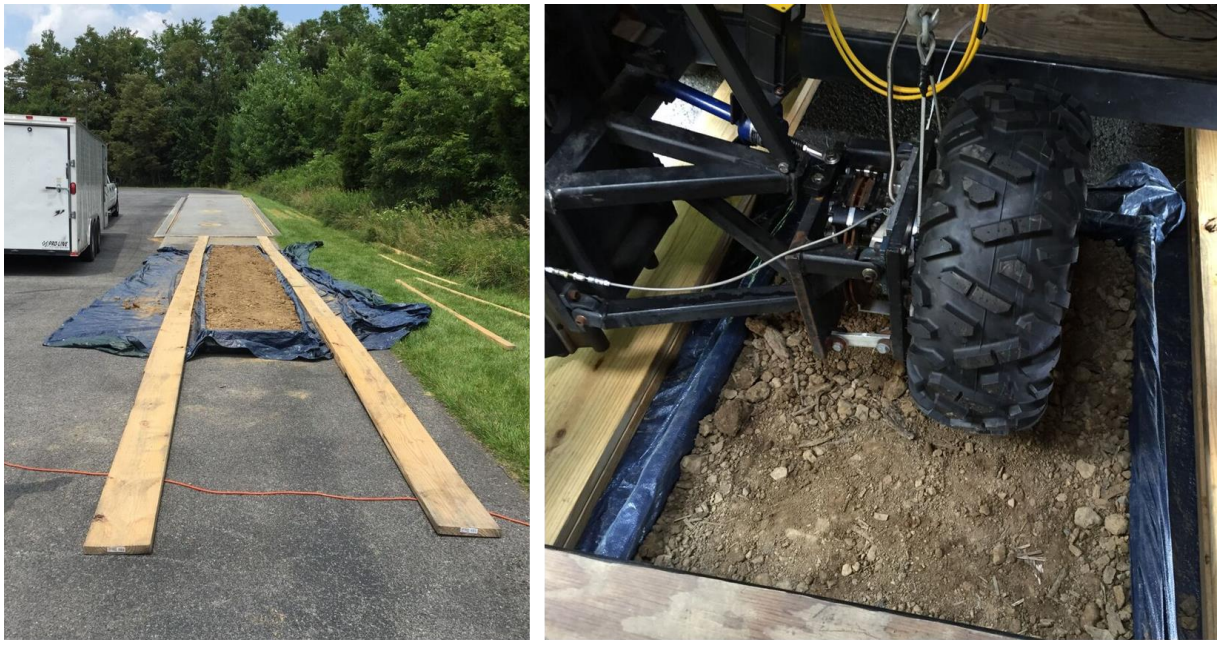

(a) (b)

Figure 45: (a) Outdoor soil rig filled with sandy loam soil (b) An ATV tire mounted on the spindle running on the outdoor soil rig

The acquired forces and moment signals are filtered using a 4th order Butterworth filter to eliminate signal contents over 1000 Hz, which can be associated to noise. Next, a moving average filter is applied to signals to smooth them. Also, the data outliers are identified and excluded from the signals. Finally, the longitudinal and lateral force signals are normalized with the vertical force data. The resulted signals are shown in Figure 46 and Figure 47.

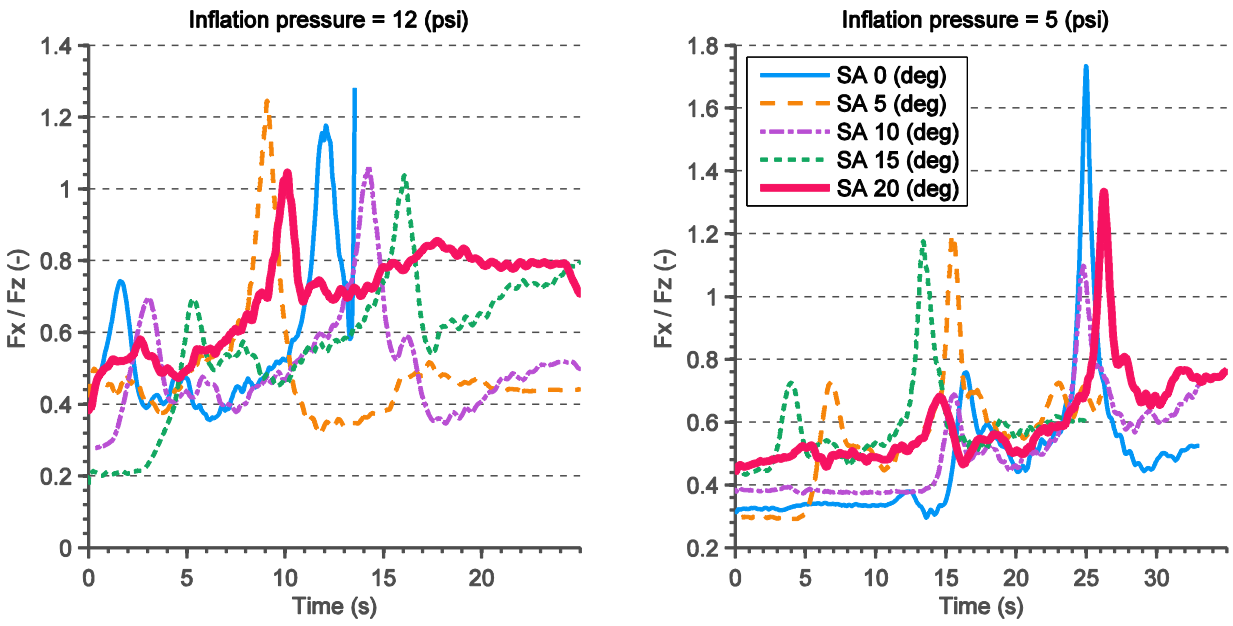

Figure 46: Normalized longitudinal force at the wheel center of the tire in instrumented trailer. Tire is in free rolling condition and travels on a flat peat soil at five different slip angles and two inflation pressure values.

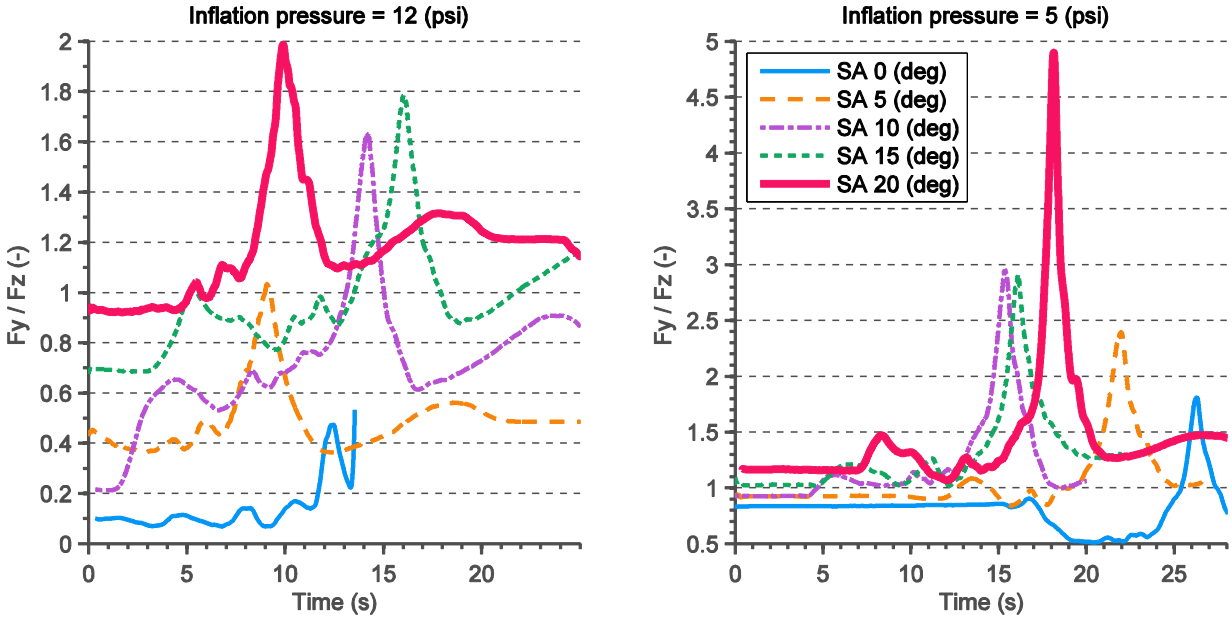

Figure 47: Normalized lateral force at the wheel center of the tire in instrumented trailer. Tire is in free rolling condition and travels on a flat peat soil at five different slip angles and two inflation pressure values.

Increasing the tire inflation pressure causes the tire to sink more into to the soil and have a smaller contact patch. This reduces the capacity of shear force generation in the contact patch, and consequently decreases the peak and average of the longitudinal and lateral forces. Moreover, increasing the slip angle increases soil shear stress and soil displacement in lateral direction, and peak of the lateral force. Therefore, at higher slip angles tire longitudinal force generation capacity declines.

The soil was artificially constrained due to the very narrow path constructed, so it did not have the lateral behavior of the natural/field soil. The terramechanics equations that are implemented in the terrain model consider the soil to be a semi-indefinite medium, and consequently cannot be used to study the acquired outdoor test data. Also, the height of the soil was shallow due to the limited amount of the available soil. This will magnify the effect of the rigid surface under the soil volume. It should be emphasized that due to the limitation of the outdoor test studies, the recorded data is not used for benchmarking purposes or any other direct comparison. The results from outdoor tests are mostly used for evaluating the performance of the tire test trailer for outdoor maneuvers, and improving the test rig setup for future similar experiments.

6.6. Conclusion

Initially, tire geometrical properties were measured for the LTX P235/85 R16 Radial Reference Test Tire. This tire was instrumented with accelerometers around its circumference, and the radial modal analysis tests were performed. During these tests, the tire was excited at different locations with an instrumented hammer, and the acceleration data was recorded at multiple sensor locations. This test data, collected at University of Pretoria, has been used for tire model parameter estimation in the radial direction. For the tire torsional behavior, the test tire was mounted on a force hub and torsional displacements were applied to the tire using a controlled actuator. Tire sidewall and tread

movements were captured using high-speed cameras at 250 Hz, and processed for extracting tire torsional natural frequencies and damping values.

Additionally, the test tire was mounted on a Terramechanics test rig at Virginia Tech's AVDL, which allows performing controlled tire maneuvers on various terrains such as sandy loam and ice. The experiments were conducted by rolling the tire over the terrain and controlling the levels of slip angle, camber angle, normal load, and slip ratio. All the forces and moments at the tire spindle were measured using a Kistler P650 force transducer. Also, wireless infrared (WITS) sensors were installed inside the tire to measure the tire deflection during the tests in order to help compute the sinkage [109, 133, 134].

The tire test trailer is used for performing the outdoor testing. A small passenger car tire was tested on a sandy loam soil in straight line travels with five different tire slip angles, and two inflation pressure levels. For these tests, the tire normal load was controlled with an air spring system, and forces and moments were measured at the wheel center using a Kistler P530 force transducer system. The processed force data shows that increasing the slip angle increases the peak of the lateral forces while decreasing the longitudinal force generation capability. Also, increasing the tire inflation pressure causes more tire sinkage and reduces tire contact patch area. This will ultimately reduce the average values of the longitudinal and of the lateral forces.

Chapter 7: Tire Model Parameter Estimation

7.1. Introduction

The tire model parameter estimation is defined as the set of experiments and data processing methods that are performed to parameterize the tire model. There are different methods that can be used for tire model parameter estimation. These methods range from completely empirical to semi-empirical methods. For the model developed in this study, a complete set of tire parameterization methods for individual parameters is proposed. In Figure 48, the types of parameters that can be obtained from each set of tests are shown.

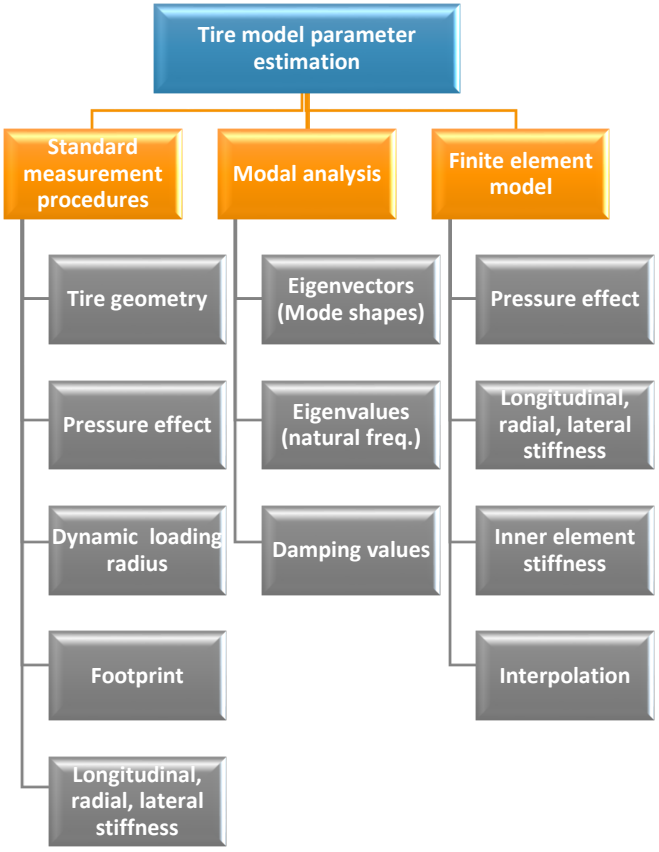

Figure 48: Tire model parameter estimation procedures which are used for defining the tire model parameters (gray rectangles), and tire parameters resulted from post-processing of each set of tests (light blue rectangles).

For the tire model developed in this study, the stiffness and the damping characteristics of the tire are considered to be different for in-plane and out-of-plane directions. As a result, during the loading of the tire in the vertical direction, for example, the slope of the tangent line to the load-deflection curve is not just due to the in-plane radial stiffness of the tire. Therefore, for measuring different stiffness and damping parameters of the model, depending solely on standard measurement procedures, is not always effective. Furthermore, conducting a wide variety of tests on the tire in different configuration, such as axial and tangential loading, tire relaxation time measurements, and cleat tests requires a large amount of time and resources, which may not always be feasible.

Having these limitations in mind, a finite element model (FEM) of the tire has been implemented [51, 52], which can be used for simulating virtual parameterization tests, as well as for the validation of the lumped mass soft-soil tire model simulations. As mentioned previously, the tire tread is not considered in the initial version of the FEM model to make the validation of the lumped mass model easier. Some material properties of the FEM model were obtained from the manufacturer documentation; the rest of the required properties were obtained through experimental tests done on a similar tire by other researchers [24]. The FEM model validation based on Tire Model Performance Test (TMPT) data is done qualitatively and quantitatively. The details of the TMPT program are explained in the "Experimental study" section.

In the qualitative method, the trend of the data with different parameter changes is studied. The quantitative approach compares measured data from two similar simulations done with different methods. The tire FEM model used in this study is developed by the author and presented in his

M.S. thesis [51]. The finite element model is initially compared with steady-state experimental data.

An optimization routine is developed to estimate a set of model parameters that can result in the highest correlation between the model estimations and the test data. The overview of the parameterization procedure is shown in Figure 49. The nonlinear curve-fitting procedure is implemented as a least-squares optimization [136]. The cost function for this optimization problem reads:

$$\min_{\lambda} \left\| \Omega(\lambda, inputs) - responses \right\|_2^2 = \min_{\lambda} \sum_i \left(\Omega(\lambda, input_i) - response_i \right)^2 \tag{172}$$

Where Ω is the tire structure model outputs, *responses* is corresponding system output from the test data, and λ is the set of model parameters. Having a correct estimation of the tire model parameters as the initial conditions in the optimization algorithm is crucial in its fast convergence to the final set of model parameters that can minimize cost function [137]. The "lsqcurvefit" function in MATLAB is used to solve the optimization problem. The function solver is set to the trust-region-reflective algorithm [138]. This algorithm is a subspace trust-region method and is based on the interior-reflective Newton method [139]. Each iteration involves the approximate solution of a large linear system using the method of preconditioned conjugate gradients (PCG).

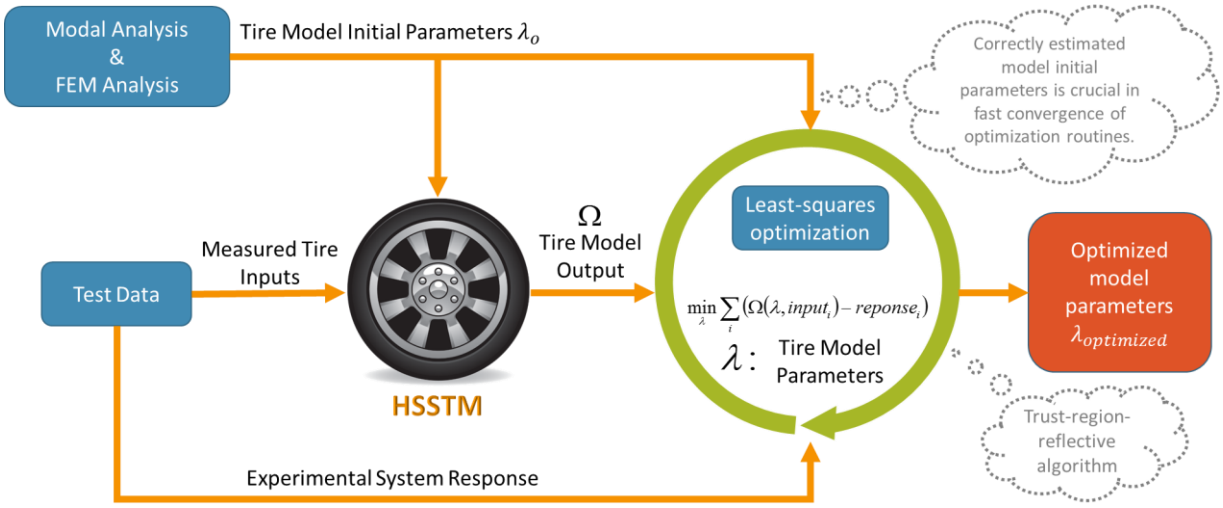

Figure 49: Overview of the HSSTM parameter estimation procedure

7.2. Tire Modal Analysis

For the modal analysis test tire is excited using a dynamic force and dynamic acceleration signals are measured at multiple locations around the tire circumference. This method is called the Single Input Multiple Output technique (SIMO). The Frequency Response Functions (FRFs) are obtained using the following function:

$$H_i = \frac{S_{FX_i}(\omega)}{S_{FF_i}(\omega)} \tag{173}$$

Where $S_{FX_i}(\omega)$ is the averaged crossed spectral density, $S_{X_iX_i}(\omega)$ is auto spectral density at the i^{th} measurement location, and $S_{FF}(\omega)$ is auto spectral density of the excitation force. The input excitation is applied to the tire using a hand-held excitation hammer. In this approach, it is challenging to control the intensity and direction of impacts precisely. The coherence function is exploited for each set of measurement signals to assess the validity of measurements:

$$\Gamma_i(\omega) = \sqrt{\frac{\left|S_{FX_i}(\omega)\right|^2}{S_{X_iX_i}(\omega) S_{FF}(\omega)}} \tag{174}$$

Using the frequency response functions, the natural frequencies are identified from the location of the peaks and the damping values can be calculated from the width of the peaks. The natural frequencies and damping values for the radial modes (R) and transverse modes (T) of the unloaded, non-rotating tire are compared to the experimental values obtained from the TMPT data. The results are shown in Table 13.

Table 13: Comparison between modal analysis simulation test results and experimental data.

	Natural Freq. (Hz)			Damping %		
Modes	**ABAQUS**	**Test**	**Error**	**ABAQUS**	**Test**	**Error**
T0	47.54	47.20	0.72	0.023	0.021	9.52
T1	55.85	61.40	9.04	0.031	0.029	6.9
R0	79.35	81.77	2.96	0.066	0.068	2.94
R1	87.60	97.35	10.01	0.041	0.044	6.82
T2	104.68	116.02	9.77	0.038	0.036	5.56
R2	124.74	122.93	1.47	0.027	0.032	15.63
R3	145.17	149.47	2.87	0.02	0.024	16.67
R4	165.48	176.64	6.31	0.021	0.024	12.5

It can be seen that in most of the modes, the FEM model results correlate with the experimental data within a reasonable error margin. Meanwhile, the model slightly underestimates most of the natural frequencies and radial damping values; on the other hand, it overestimates the transverse damping values. The natural frequencies and damping values are further processed in order to find the force elements, stiffness and damping values in different directions (lateral, radial, longitudinal, inner element, etc.).

7.3. Estimating Tire Mode Shapes

The tire mode shapes are related to the gain of the resonance frequencies. The gains can be specified from the height of the peaks of the frequency response functions. In order to estimate the tire mode shapes, the frequency response function should be decomposed into individual response function corresponding to each resonance natural frequency. The structure dynamic response at each resonance peak is modeled using a single degree of freedom system SDOF. This simplifying assumption is applicable because the resonance frequencies are well separated. The FRF of a SDOF has the following form:

$$S_n(\omega) = \frac{\omega_{0n}^2}{\omega_{0n}^2 + 2jc_n\omega\omega_{0n} - \omega^2} \tag{175}$$

Where ω_{0n} is natural frequency of the SDOF system and c_n is the corresponding damping. The total estimated response function of the tire at point i^{th} is equal to the sum of all modal response functions multiplied by modal amplitudes $a_{i,n}$:

$$H_i^{est}(\omega) = \sum_{n=1}^{m} a_{i,n} S_n(\omega) \tag{176}$$

Where *n* and *m* represent the mode number and number of modes used respectively. The modal amplitude is calculated using the i^{th} experimental modal response $H_i^{\exp}(\omega)$:

$$a_{i,n} = \frac{\overline{S_n}(\omega)^T H_i^{\exp}(\omega)}{\overline{S_n}(\omega)^T S_n(\omega)} \qquad (0.95\omega_{0n} < \omega < 1.05\omega_{0n}) \tag{177}$$

To evaluate the fitted frequency response function $H_i^{est}(\omega)$, we define the error function $E_{i,n}$ as:

$$E_{i,n} = \left\| H_i(\omega) - a_{i,n} S_n(\omega) \right\| \qquad (0.95\omega_{0n} < \omega < 1.05\omega_{0n}) \tag{178}$$

And the total error is found as:

$$E_n = \sum_{j=1}^{n_{mr}} E_{n,i} \tag{179}$$

Where n_{imr} is the total number of measured frequency response functions. Table 14 and Table 15 demonstrate the tire mode shapes in radial and transverse directions corresponding to the natural frequency listed in Table 13 [51].

Table 14: Tire radial modes

Modes	Front View	Top View
R0	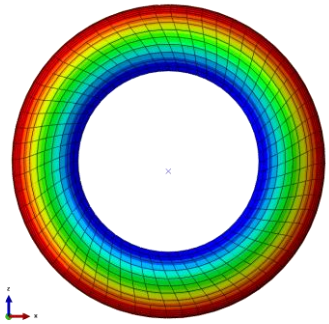	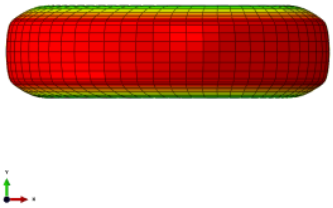
R1	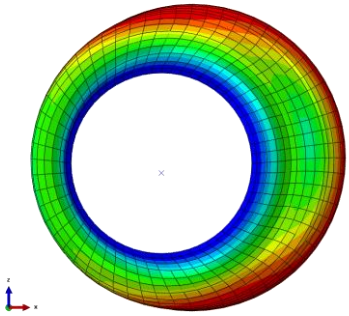	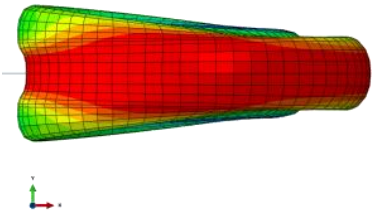
R2	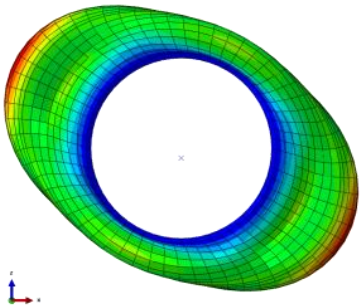	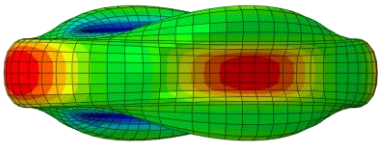
R3	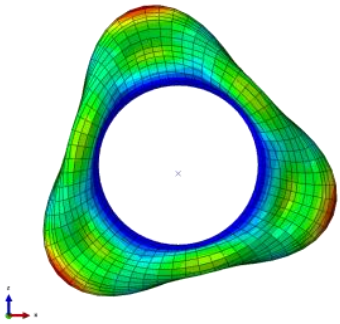	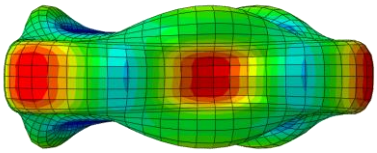

Table 15: Tire transverse modes

Modes	Front View	Top View
T0	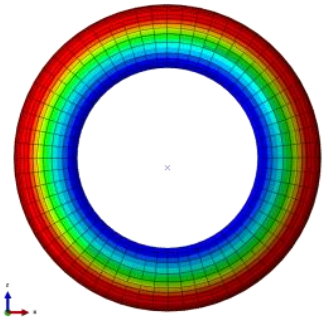	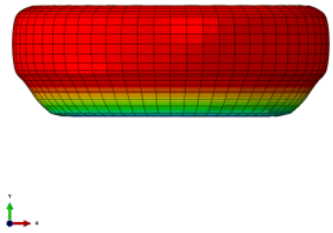
T1	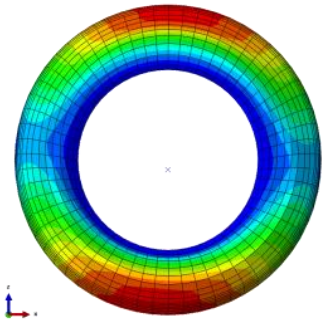	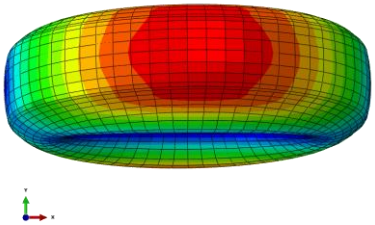
T2	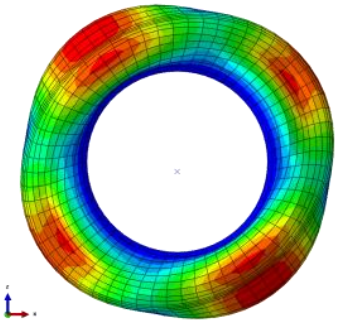	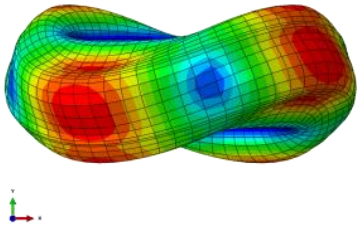
T3	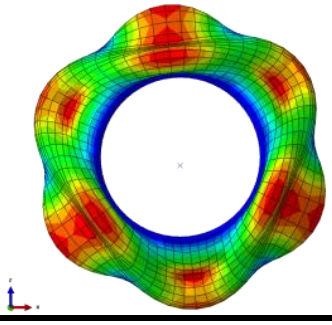	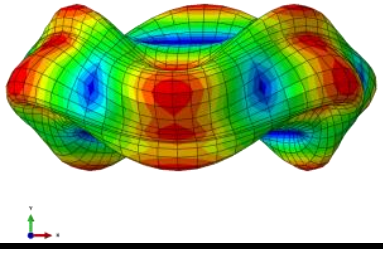

7.4. Theoretical Tire In-plane Vibrational Analysis

In order to calculate the theoretical tire in-plane natural frequencies and damping values, tire can be simplified as an elastic ring on an elastic foundation. Using this realization for tire, the equations of motion can be written as:

$$-\frac{EI}{a^4}\left(\frac{\partial^2 u_\theta}{\partial\theta^2}-\frac{\partial^3 u_r}{\partial\theta^3}\right)-\frac{EI}{a^2}\left(\frac{\partial^2 u_\theta}{\partial\theta^2}-\frac{\partial u_r}{\partial\theta}\right)+k_\theta^{'}u_\theta+m\ddot{u}_\theta=0 \tag{180}$$

$$-\frac{EI}{a^4}\left(\frac{\partial^3 u_\theta}{\partial\theta^3}-\frac{\partial^4 u_r}{\partial\theta^4}\right)+\frac{EI}{a^2}\left(\frac{\partial u_\theta}{\partial\theta}+u_r\right)+k_r^{'}u_r+m\ddot{u}_r=0 \tag{181}$$

Where:

$$k_\theta^{'}=k_\theta b \tag{182}$$

$$k_r^{'}=k_r b \tag{183}$$

$$m=\rho A+\frac{1}{3}\rho_F h_F b \tag{184}$$

The parameters k_θ and k_r are the foundation stiffness values in radial and tangential directions, b is the width of the ring, h is the thickness of the ring, $A=bh$ is the cross area, and $I=bh^3/12$ is the area moment of inertia. The radial and tangential solutions for the equations of motion are denoted as:

$$u_r(\theta,t)=A_n\cos n(\theta-\phi)e^{j\omega t} \tag{185}$$

$$u_\theta(\theta,t)=B_n\sin n(\theta-\phi)e^{j\omega t} \tag{186}$$

Substituting above solutions in the equations of motion (EOM) will result in:

$$\begin{bmatrix} \alpha_{11} - m\omega_n^2 & \alpha_{12} \\ \alpha_{21} & \alpha_{22} - m\omega_n^2 \end{bmatrix} \begin{Bmatrix} A_n \\ B \end{Bmatrix} = 0 \tag{187}$$

Where:

$$\alpha_{11} = \frac{n^4 EI}{a^4} + \frac{EA}{a^2} + k_3^{'} \tag{188}$$

$$\alpha_{12} = \alpha_{21} = \frac{n^3 EI}{a^4} + \frac{nEA}{a^2} \tag{189}$$

$$\alpha_{22} = \frac{n^2 EI}{a^4} + \frac{n^2 EA}{a^2} + k_\theta^{'} \tag{190}$$

The nontrivial roots of the determinant is calculated by solving the following equation:

$$\omega_n^4 - K_1 \omega_n^2 + K_2 = 0 \tag{191}$$

Where

$$K_1 = \frac{n^2 + 1}{a^2 m}\left(\frac{n^2 EI}{a^2} + EA\right) + \frac{k_r^{'} + k_\theta^{'}}{m} \tag{192}$$

$$K_2 = \frac{n^2\left(n^2 - 1\right)^2}{a^6 m^2} E^2 IA + \frac{k_r^{'} k_\theta^{'} + k_r^{'}\left(n^2 E/a^2\right)\left[\left(I/a^2\right) + A\right] + k_\theta^{'}\left(E/a^2\right)\left[\left(n^4 I/a^2\right) + A\right]}{m^2} \tag{193}$$

The natural frequency for the n^{th} mode is:

$$\omega_{n1}^2 = \frac{K_1}{2}\left(1 - \sqrt{1 - 4\frac{K_2}{K_1^2}}\right) \tag{194}$$

$$\omega_{n2}^2 = \frac{K_1}{2}\left(1+\sqrt{1-4\frac{K_2}{K_1^2}}\right) \tag{195}$$

The natural frequency set ω_{n1} is associated with the ring modes for which the radial motion dominates. On the other hand, the higher natural frequency set ω_{n2} corresponds to ring modes where tangential displacement is more significant. Therefore, by measuring the frequencies ω_{n1} and ω_{n2} for the first radial and torsional modes of the tire we can calculate k_θ and k_r.

7.5. Parameter Estimation Procedure

The parameter estimation process is started by finding initial values for the tire structure model parameters. These initial values are used in a non-linear curve-fitting process as initial guesses for finding a set of model parameters that can result in the highest correlation between the model estimations and the test data. In this regard, the measured tire modal frequencies have been utilized to estimate tire parameters corresponding to in-plane tire dynamics. The calculated tire model parameters are included in Table 16.

Table 16: Tire model parameters

Parameter	Symbol	Value	Unit
Tire bending stiffness	*EI*	3.654	N.m^2
Tire extensional stiffness	*EA*	4.12 E6	N
Sidewall tangential stiffness	K_{st}	3.234 E5	N/ m^2
Sidewall radial stiffness	K_{sr}	8.168 E4	N/ m^2

Sidewall lateral stiffness	K_{sl}	2.212 E5	N/ m^2
Belt tangential stiffness	K_{bt}	3.544 E6	N/ m^2
Belt radial stiffness	K_{br}	5.481 E4	N/ m^2
Belt lateral stiffness	K_{bl}	6.990 E6	N/ m^2

7.5.1. Tire Model Parameter Estimation in Radial Direction

In order to find the sidewall and belt radial stiffness values, the cost function for the optimization problem is defined as:

$$\min_{K_{sr},K_{br}} \sum_i \left(\Omega\left(K_{sr}, K_{br}, Z_{ground}, Camber\right) - F_z\right)^2 \tag{196}$$

Where K_{sr} is the sidewall radial stiffness, K_{br} is the belt radial stiffness, and F_z is the vertical load at the wheel center. The vertical loading simulations are conducted by applying the camber angle, fixing the tire at the spindle, placing the cleat at the test configuration angle and adjacent to the tire circumference, and vertically displacing the ground. Next, a smoothing function is fitted to the vertical force versus displacement experimental data at different test configurations (The cleat test experimental data used for parameter estimation is courtesy of Vehicle Dynamics Group at the University of Pretoria, S. Africa). This process results in 9 different force-displacement curves for 3 camber angles and 3 cleat configurations. The fitted line to the experimental data is shown as a blue line in Figure 50, Figure 51, and Figure 52. These 9 data sets are concatenated and used in the described optimization routine to find tire model sidewall and belt radial stiffness values.

The parameterized tire structure model is used to estimate the vertical force at the wheel center with model inputs from the experimental setup including the tire camber angle, cleat orientation and vertical displacement. The estimated vertical load signals at different test conditions are shown in Figure 50, Figure 51, and Figure 52.

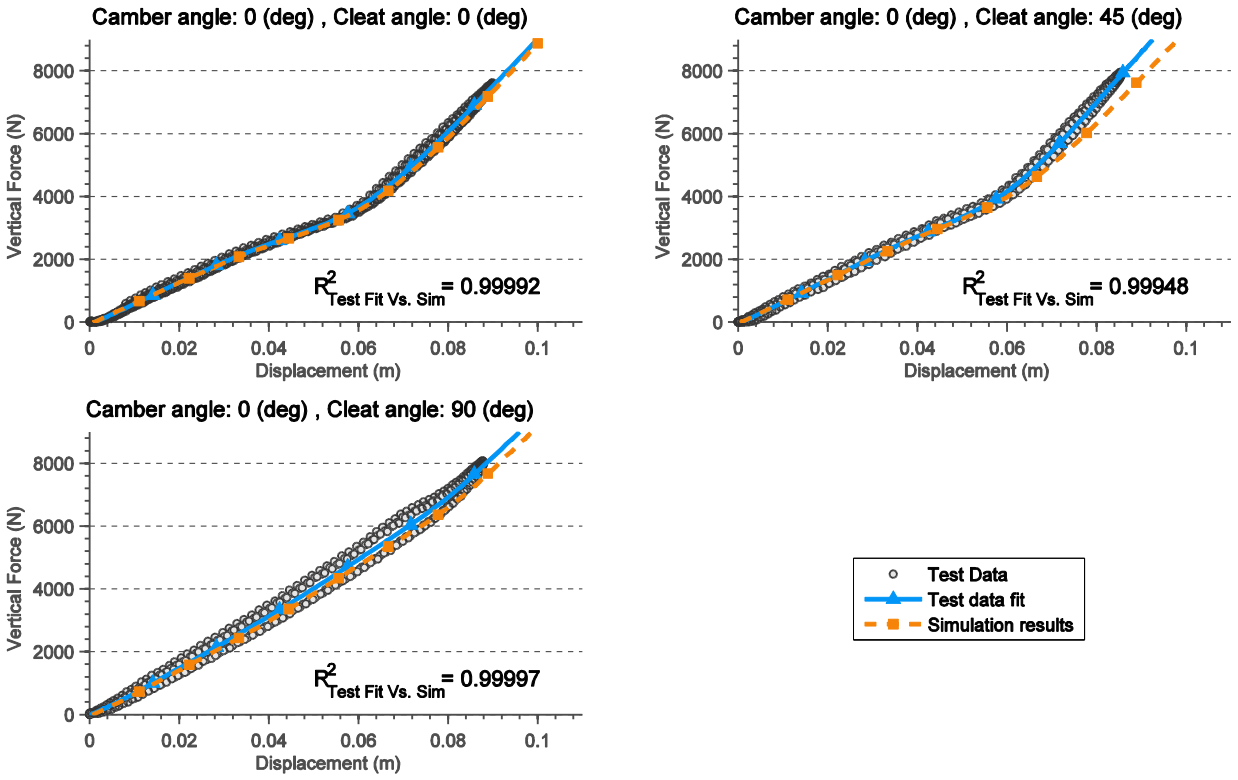

Figure 50: Tire quasi-static loading test with rectangular cleat setup at 0, 45, and 90 deg orientations and at 0 deg camber angle

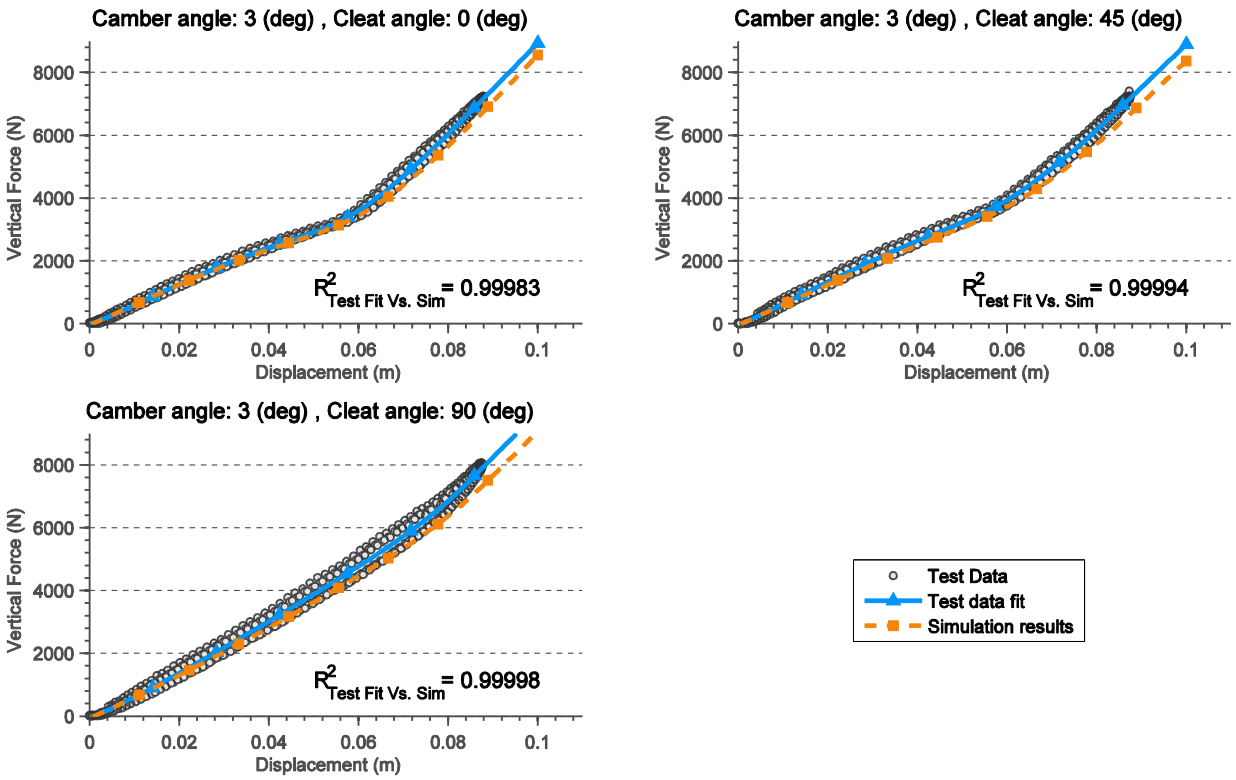

Figure 51: Tire quasi-static loading test with rectangular cleat setup at 0, 45, and 90 deg orientations and at 3 deg camber angle

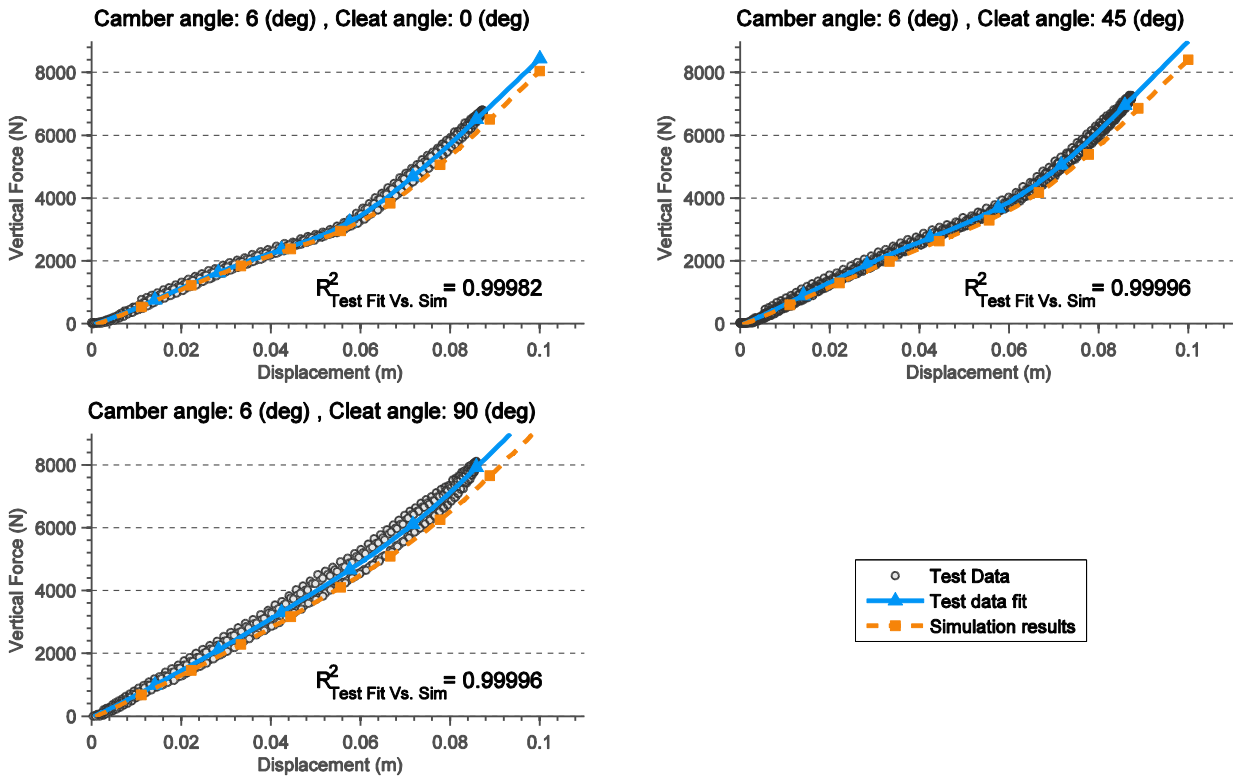

Figure 52: Tire quasi-static loading test with rectangular cleat setup at 0, 45, and 90 deg orientations and at 6 deg camber angle

In order to measure the accuracy of force-displacement estimations, the simulation results are correlated with experimental results at identical input conditions, and the correlation coefficient R^2 is shown on the figures. It can be seen that using the final optimized tire sidewall and belt radial stiffness values, the estimated normal loads at the wheel center during the cleat test loading at different test conditions have high correlation (R^2 near unity) with experimental data.

7.5.2. Tire Model Contact Area Validation

During the tire vertical loading experiments, a series of test runs are conducted on a flat glass plate to determine the tire's contact patch area. A camera was mounted beneath the glass plate to capture the contact patch shape and area. As it was discussed in section 6.3, the contact patch images are converted to bitmap images, which are ultimately used to calculate the tire contact

patch area. The calculated contact patch area values at the end of the loading process on a flat plate at three tire camber angles are shown in Figure 38. Tire model simulations are conducted with the input configurations similar to the test setup in order to evaluate the contact patch area. The estimated area calculations at three tire camber angle values are included in Figure 53.

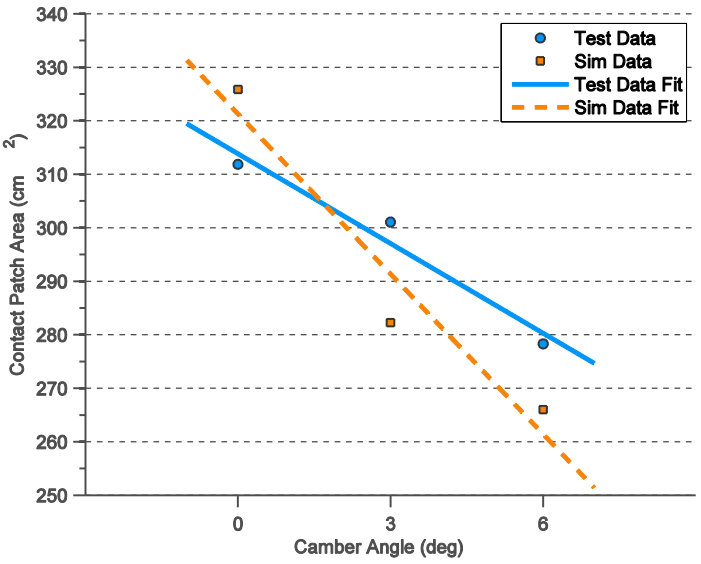

Figure 53: Contact patch area comparison between model estimation and experimental results

The developed tire model overestimates the contact patch area at zero camber angle. This was expected because the tread pattern is not included in the simulation model. In other words, the sipes and grooves in the tread pattern reduce the effective contact patch area during the experiments. Moreover, at non-zero camber angles, the tread pattern features enable the belt package to deform extensively under the loading, which results in uniform contact over the surface, whereas for the simulated tire model, the belt package behaves as a membrane that pivots over the contacting sidewall, and, consequently, has less uniform contact with the ground surface. This makes the estimated tire contact patch area less than the calculated value from the experiments at non-zero camber angles.

7.5.3. Tire Model Parameter Estimation in Longitudinal and Lateral Directions

As it was discussed earlier, the total deformation of the brushes, which are used in the non-deformable terrain model, relative to the ground surface, depends on the brush stiffness as well as tire sidewall and belt stiffness values in longitudinal and lateral directions. Therefore, a set of model parameters for the integrated tire-terrain models should be identified that can results in accurate contact shear force estimations. The terrain model, which was parameterized previously, is integrated with the HSSTM tire model to conduct some cornering and braking/accelerating simulations. During the braking/accelerating tests, tire slip ratio is changed from -30% to 30% to -30% at different levels of normal load. The tire steady-state force generation characteristics as well its transient dynamic behavior are involved in this type of simulation. The following cost function is defined to find the model parameters in longitudinal direction:

$$\min_{K_{st},K_{bt},C_{st},C_{bt}} \sum_i \left(\Omega\left(K_{st},K_{bt},C_{st},C_{bt},\kappa\right)-F_x\right)^2 \tag{197}$$

Where K_{st} is the sidewall tangential stiffness, K_{bt} is the belt tangential stiffness, C_{st} is the sidewall tangential damping, K_{bt} is the belt tangential damping, κ is slip ratio, F_z is the vertical load at the wheel center, and F_x is the longitudinal force at the wheel center. The optimization algorithm is applied to the experimental data to find a set of tangential model parameters that can minimize the model longitudinal force estimation error. With this set of model parameters, the simulations are conducted at the test condition to estimate the longitudinal forces at different normal load levels. The experimental and calculated tire longitudinal forces are shown in Figure 54.

As for the cornering case study, the tire slip angle is swept from -12 deg to 12 deg to -12 deg at different levels of normal load. For the lateral parameter estimation case study, the following cost functions is introduced:

$$\min_{K_{sl},K_{bl},C_{sl},C_{bl}} \sum_i \left(\Omega(K_{sl},K_{bl},C_{sl},C_{bl},\alpha) - F_y\right)^2 \tag{198}$$

Where K_{sl} is the sidewall lateral stiffness, K_{bl} is the belt lateral stiffness, C_{sl} is the sidewall lateral damping, K_{bl} is the belt lateral damping, α is slip angle, F_z is the vertical load at the wheel center, and F_y is the lateral force at the wheel center. Similar to tangential case study, the optimization algorithm was incorporated to find the lateral model parameters that minimize the error of lateral force. With this parameter set, the lateral tests are simulated at the similar normal load and slip angle inputs. The lateral force curves from experimental data as well as model estimations are shown in Figure 54.

Furthermore, the aligning and overturning moment curves are plotted in Figure 55. It can be seen that terrain model force and moment estimations are in good agreement with experimental results. The hysteresis loop in the forces and moments curves is associated with the tire transient effect. This phenomenon causes the forces and moments curves to not follow the same trend during the increasing and the decreasing slip value changes, as can be seen in Figure 54 and Figure 55.

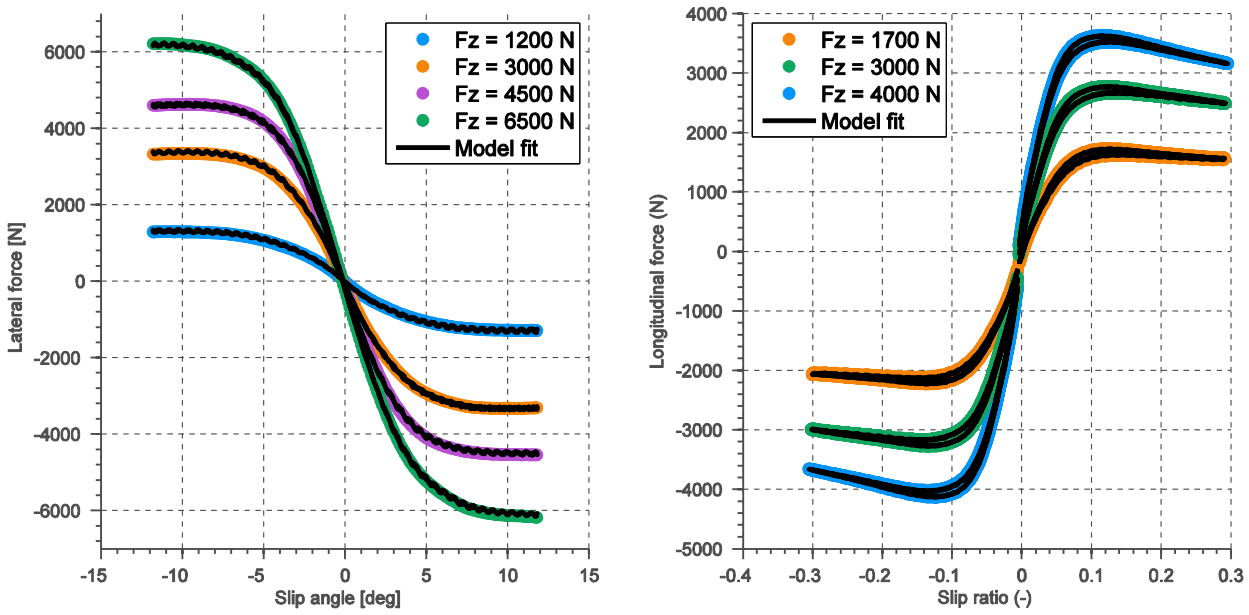

Figure 54: lateral and longitudinal forces during tire interaction with non-deformable terrain

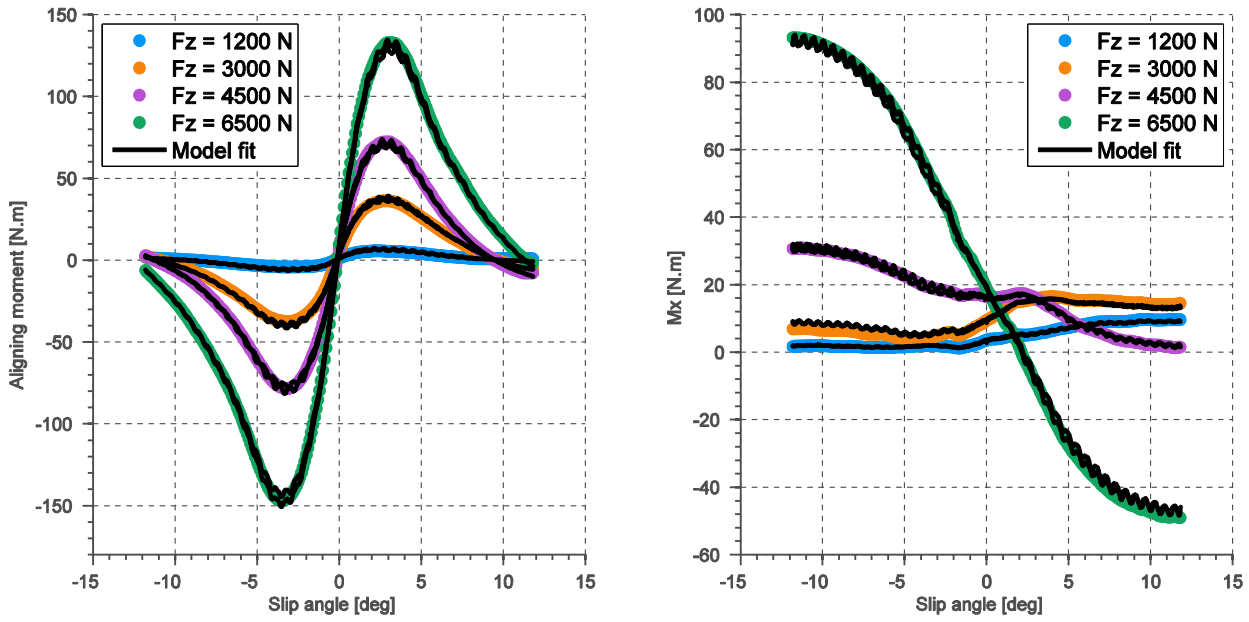

Figure 55: aligning and overturning moments during tire interaction with non-deformable terrain

The final calculated tire model parameters are included in Table 17.

Table 17: Tire model final optimized parameters

Parameter	Symbol	Value	Unit
Sidewall tangential stiffness	K_{st}	2.921 E5	N/ m^2
Sidewall radial stiffness	K_{sr}	8.965 E4	N/ m^2
Sidewall lateral stiffness	K_{sl}	3.251 E5	N/ m^2
Belt tangential stiffness	K_{bt}	3.129 E6	N/ m^2
Belt radial stiffness	K_{br}	5.520 E4	N/ m^2
Belt lateral stiffness	K_{bl}	7.103 E6	N/ m^2

7.6. Conclusion

The HSSTM model parameter estimation study is conducted to find a set of model parameters that can minimize the error between the model estimations and the experimental results. The individual test studies are done to compute the model parameters in radial, tangential, and lateral directions.

Initially, from the modal analysis data, the input acceleration signal (from the input hammer), and output acceleration signals (from the accelerometers installed on the circumference of the tire) are used to construct the frequency response functions between the input-output points. Moreover, the tire mode shapes, natural frequencies and damping values were extracted from the corresponding FRFs. In order to correlate the modal analysis results to tire in-plane dynamics, tire

structure was idealized as an elastic ring on an elastic foundation. The natural frequency and damping values for the theoretical model were calculated and related to the experimental data. As a result, the initial stiffness and damping values for the in-plane force elements used in the tire model were identified.

A least-square curve-fitting algorithm is used to find the model parameters in radial, longitudinal and lateral directions. The initially calculated model parameters are essential in having the optimization algorithm to converge to the final set of model parameters quickly. The quasi-static cleat loading tests are used to find the tire model sidewall and belt radial parameters. The accuracy of the tire structure model in estimating tire radial behavior is examined by comparing the vertical force at the spindle and tire contact patch area from the model to those from the experimental results. Finally, tire longitudinal and lateral force test data from the FlatTrac machine are exploited in the developed optimization algorithm to estimate the tire model parameters in longitudinal and lateral directions.

Chapter 8: HSSTM Simulation Platform

8.1. Introduction

The HSSTM simulation platform is described in this chapter. The simulation interface for integrating the tire model with a multi-body dynamics software is introduced. For model verification, a series of benchmark case studies are discussed, which can demonstrate the dynamic capabilities of the HSSTM model. These simulations are envisioned to verify the correctness of the computation model, and ensure that it represents the mathematical formulation developed. Additionally, the validation studies are performed based on the experimental data to make sure that the developed mathematical model can express the physical problem with acceptable accuracy.

8.2. Vehicle Simulation Platform

In order to characterize the configuration of the test rig in the simulation environment, an application platform is designed in order to accommodate the communications with the multibody dynamics solver. The spindle carriage is represented using a quarter-car model, and is implemented in a separate module, which has its own ordinary differential equations (ODE) solver. At every time step, the vehicle model, which is described in a multibody dynamics framework, provides the wheel kinetics and kinematics variables to the tire model. The time step for the tire model solver is chosen as half the time step set for the multibody dynamics solver. This is due to the fact that extra calculations are performed in the middle of the fixed time intervals to improve the accuracy. These extra calculation results are provided to the external solver for maximizing the ODE solver performance. Next, the tire model updates the position and velocity state vectors of the tire. Using this new tire configuration, the terrain model exploits the contact conditions, which results in the

tire/ground deflection and stress distribution in the contact patch. The normal and shear stress fields are feedback to the tire model, which are used for solving the tire equations of motion. At the end of this step, the tire model calculates three forces and moments at the spindle and feeds them back to the vehicle model. An overview of the discussed procedure is shown in Figure 56. Additionally, as for the tire-vehicle interface, the data communication routines are developed such that they follow the standard formats from Standard Tire Interface (STI) practices.

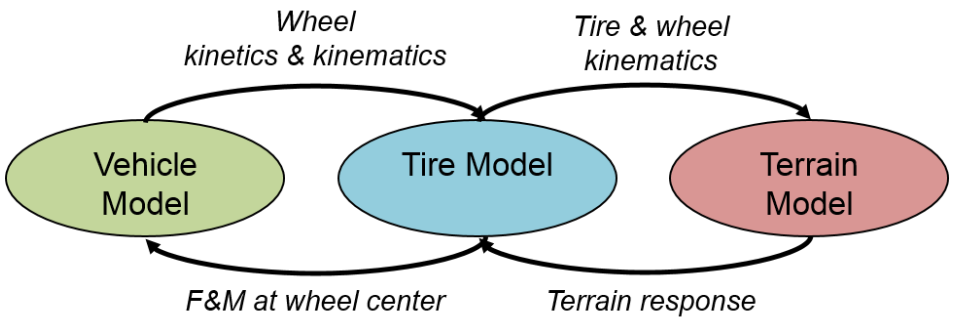

Figure 56: The communication data flow between the tire model modules during the full vehicle simulation.

It should be noted that great attention is given to the optimization of the tire model performance in order to make it a practical option for full vehicle simulations. This has become possible by applying some parallelization and multi-processing techniques to the architecture of the program. In this regard, the tire model stiffness matrix is partitioned into smaller matrices corresponding to tire belt element nodes located in multiple rings across tire width. At each simulation time step, the task of calculating forces on belt elements and solving the equations of motion for each ring is assigned to an individual CPUs. The computing of each local matrix is totally independent and so parallelization of these computations is straightforward and can be naturally explored.

To evaluate the performance of the multi-processing program architecture, tire free rolling on a non-deformable terrain is simulated with and without utilizing the multi-processing feature. The total simulation time is set to 10 s and 1800 degrees of freedom are used in the model. The

computational run time for three main simulation tasks are reported in Figure 57. It can be seen that by using the multi-processing techniques, a great improvement in the time required for assembling the model equation system and imposing the boundary conditions is observed.

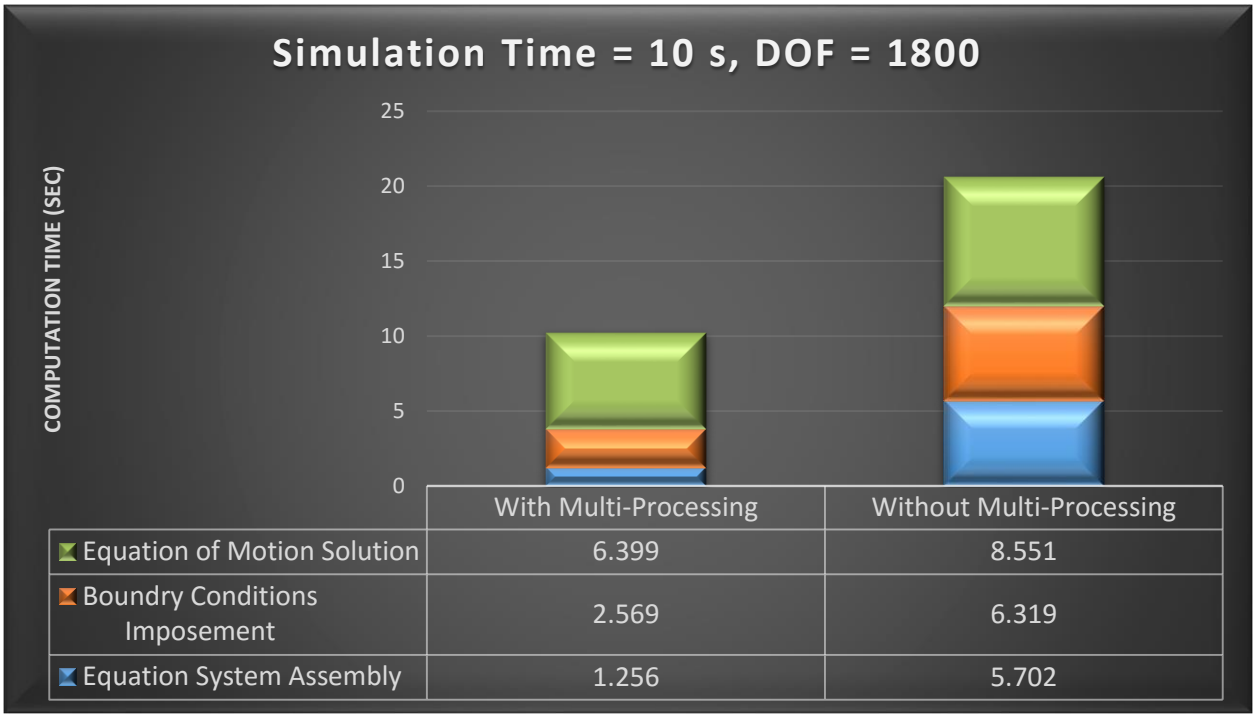

Figure 57: Contribution of each task group in the total processing time for simulations with and without utilizing multi-processing architecture

8.3. Verification studies

In this section, the verification studies are conducted to evaluate the simulation performance of the HSSTM package. The main emphasis is to showcase the capabilities of the model, and to confirm that the implemented algorithms can correctly represent the developed mathematical formulations.

8.3.1. Terrain Repetitive Loading

As it was explained in the tire-terrain interaction section, when the tire is traveling over the terrain, the ground under the contact patch is deformed. If, for the second time, the tire travels on

the same path, it will experience a different amount of resistance from the ground. Furthermore, the elastic and plastic deformation of the terrain would differ during loading and unloading phases. The visualization of the tire-terrain interaction can help debugging the implemented terrain model as well as offering a better insight into the physics of the problem. Consequently, a visualization environment is implemented to show the user-defined terrain behavior such as the terrain plastic deformation and stress distribution. Figure 58 shows snapshots of the terrain visualization environment during a terrain multi-pass maneuver.

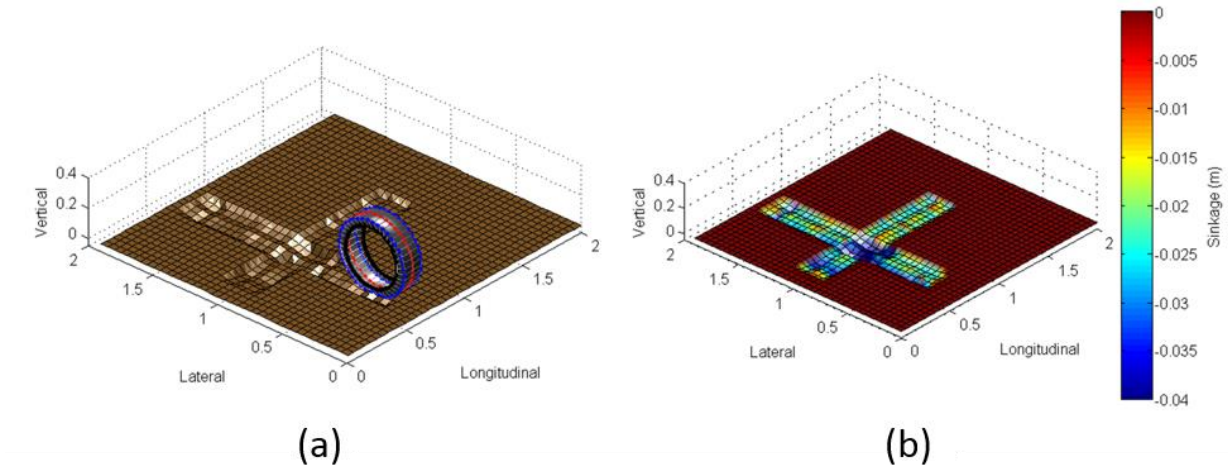

Figure 58: Terrain visualization during the multi pass simulation: (a) soil consecutive loading-unloading (b) Terrain sinkage color contour

In this simulation, the tire starts traveling over the terrain in a straight line, and it deforms the terrain surface, creating a rut. Next, the tire continues on a second path, which in this case is perpendicular to the first path. Because the HSSTM is a nonlinear system, the tire elements go under different states of normal and tangential stresses. As a result, the permanent plastic deformation of the ground after the tire passage is uneven. This deformation has larger value at the crossing section of two paths, which has gone through deformation twice. However, this deformation is less than twice the value of the rut depth on the soil sections negotiated over only

once. The mechanical properties of the mineral terrain used for conducting this simulation is the same as the "Medium terrain" shown in Table 18.

Table 18: Mechanical properties of three mineral terrains used for simulations.

Soil Type	Bekker's equation			Moisture content (%)	Shear characteristics			
	n (–)	K_c $\left(\frac{kN}{m^{n+1}}\right)$	K_ϕ $\left(\frac{kN}{m^{n+1}}\right)$		RS $\left(\frac{cm}{s}\right)$	C $\left(\frac{kN}{m^{n+1}}\right)$	Φ (deg)	K (–)
Soft terrain (LETE soil)	0.611	1.16	475.0	0	2.5	1.15	31.5	-
Medium terrain (Upland sandy loam)	0.74	26.8	1522	44.3	2.5	2.7	26.1	0.45
Hard soil (Grenville loam)	1.01	0.06	5880	24.1	2.5	3.1	29.8	0.40

8.3.2. Drawbar Pull

When the tire is moving on a deformable terrain under an applied torque at its spindle, the positive shear forces keep pushing the tire forward, while the negative ground forces (rolling resistance, bulldozing force, etc.) resist the tire motion. The resultant force is called the drawbar pull, which is an indication for the ability of a vehicle to pull/push external load, accelerate, or overcome the grade resistance. Consequently, in calculation of the drawbar pull, both motion resistance due to tire flexing and the one due to soil compaction are included. To normalize it, the drawbar pull is divided by the normal load at the spindle, thus obtaining the drawbar pull coefficient. The drawbar pull coefficient explicitly relates the tire tractive performance to the

wheel slip ratio and implicitly to the terrain normal and shearing characteristics. Using the developed model, the drawbar pull coefficient is calculated at four slip ratio values and on three selective terrain types: soft, medium, and hard soil. The slip ratio is calculated by normalizing the wheel slip velocity with the carriage longitudinal velocity:

$$\kappa = \frac{{}_{wheel}V_{sx}}{{}_{carriage}V_x} \times 100 = \frac{\left(R_{eff}\,\Omega - {}_{carriage}V_x\right)}{{}_{carriage}V_x} \times 100 \tag{199}$$

Where R_{eff} is the wheel effective rolling radius and Ω is the wheel rotational velocity. The slip ratio values are maintained at their nominal values using a PID controller that regulates the applied torque to the spindle. The terrain mechanical properties used for the simulated terrains are documented in Table 18. The results of this simulation that indicate the effect of the terrain properties on the mobility performance of the tire are presented in Figure 59.

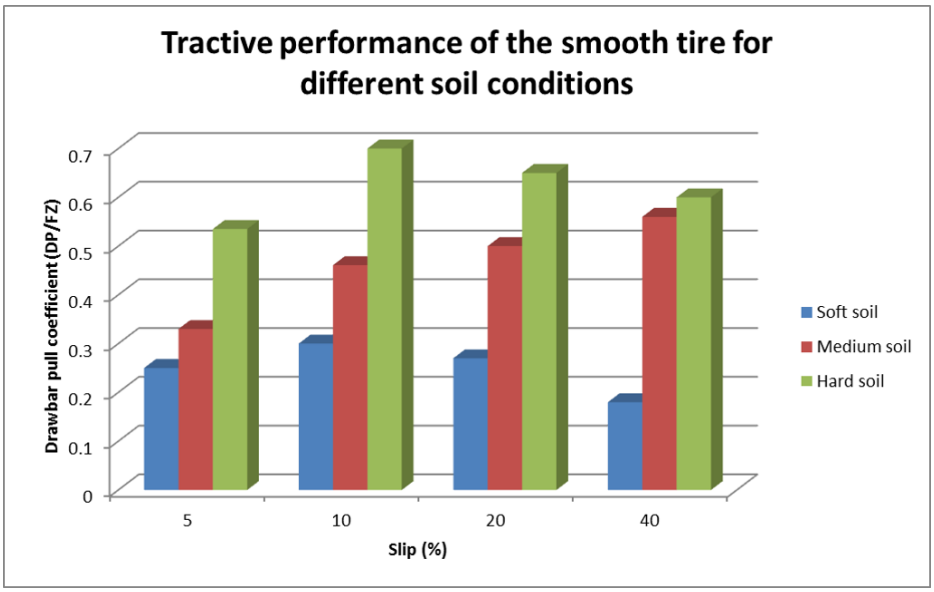

Figure 59: Tractive performance of the buffed tire simulated at four slip ratios and three different soil conditions.

8.4. HSSTM Dynamic Validation Studies

During tire parameter estimation process, tire structure quasi-static behavior was studied with the static cleat test data as well as the contact patch area data. Moreover, the validation of the developed deformable/non-deformable terrain models was done in the tire-terrain interaction chapter. In the following sections, the tire structure model dynamic characteristics are validated with the dynamic cleat test data. Next, the tire and the soft soil terrain models are integrated in the HSSTM simulation package and are used to simulate the Terramechanics test rig conditions.

8.4.1. Dynamic Cleat Test Simulations

The dynamic behavior of the tire structure model should be studied for non-deformable terrains with obstacles. In this regard, a cleat test simulation was conducted using the HSSTM model, and results were compared with three commercially available tire models, including MF-Swift, CarSim internal tire model, and Delft tire model. For the cleat test maneuver, a 225/60 R18 tire is constrained laterally, and it is towed at a speed of 40 km/h over a sharp rectangular cleat, which is 7 m wide, 0.40 m long, and 0.035 m high. The tire transient behavior in the frequency range of under 10 Hz is dominant in this test, and consequently the linear tire structure model is used for the simulations.

The MF-Swift tire model represents the tire structure with a rigid ring that is suspended on an elastic foundation. This rigid ring has a single point contact with terrain. The effect of the tread modulus is modeled as residual spring and dampers that are connected to the contact point. The normal load, slip and camber angles, and slip ratio at the tire/terrain contact point are the main inputs to the ground interaction model which outputs the forces and moments at the center of the contact patch. The Delft tire model is an implementation of the Magic Formula tire model, which models the tire structure with a single spring having a point contact with terrain. The CarSim

internal tire model has the same methodology as the Delft tire model for characterizing the tire structure stiffness, and calculating the normal load the location of tire contact with ground. The CarSim internal tire model uses table interpolation/extrapolation for calculating tire forces and moments at the center of the contact patch.

In order to estimate the HSSTM tire structure model parameters, the tire natural frequencies and damping values from the literature [140] are used as inputs to the parameters estimation procedure developed for the in-plane elastic tire model in section 7.4. The tire parameters for other benchmarked tire models are picked from the CarSim available data base for the same tire. The wheel center height and the longitudinal and vertical forces at the wheel center are plotted in Figure 60 against the wheel longitudinal displacement.

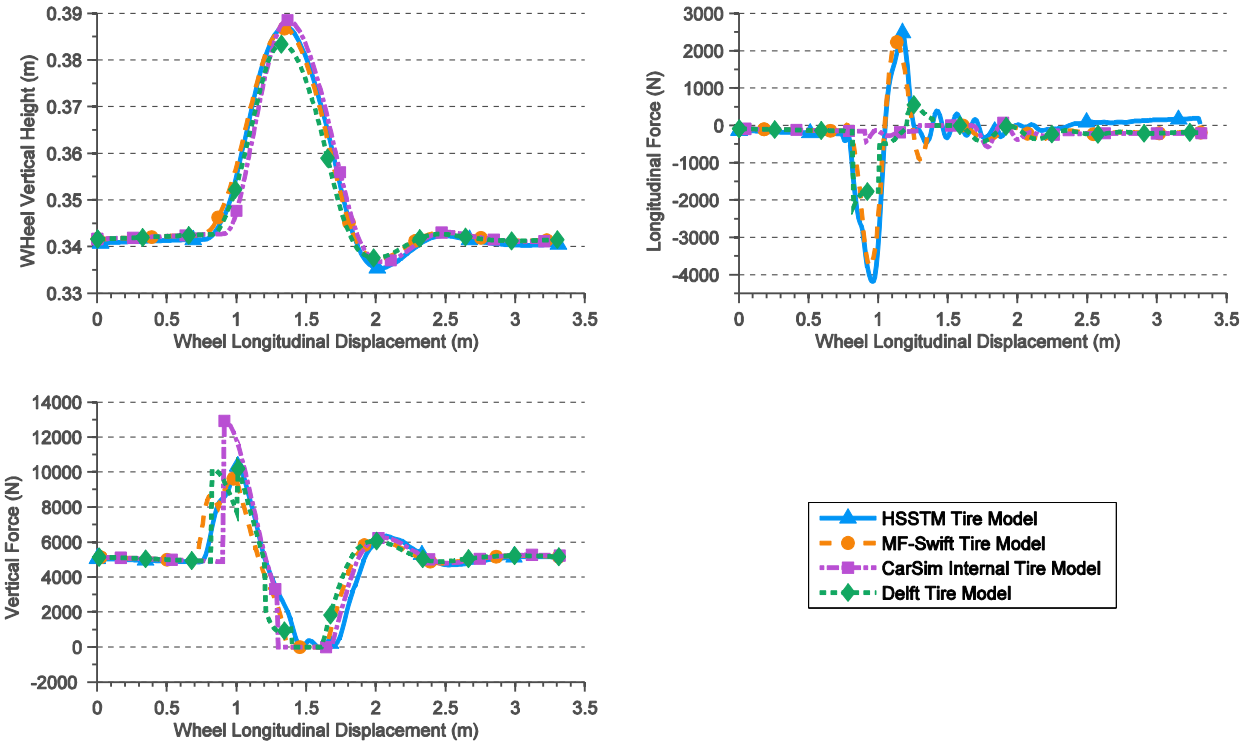

Figure 60: Cleat test simulation results for four tire models: HSSTM tire model, MF-Swift Tire Model, CarSim Tire Model, Delft Tire Model

In Figure 60, the vertical force signals at the wheel center estimated by CarSim internal tire model and Delft tire model suddenly rise when tire encounters the cleat. This impulsive behavior is due to the simplistic single spring model used in these models, which does not provide any in-plane damping nor accurate enveloping characteristics. Failure to evaluate the normal forces correctly, some of the main inputs to the force and moments estimation module, results in inaccurate longitudinal force calculation. On the other hand, the MF-Swift model, which is validated for this tire choice and test configuration in [140], has a good performance in estimating the tire vertical position and longitudinal and vertical forces. The developed HSSTM tire model has a very high correlation with the performance of the MF-Swift model. This emphasizes the capability of the HSSTM tire structure model in characterizing the dynamic tire behavior, such as enveloping over a cleat.

8.4.2. Terramechanics Test Rig Simulations

In order to compare model longitudinal force estimations with experimental results, initially, the straight line tests are conducted in Terramechanics test rig [134]. During the tests, tire slip angle, camber angle, normal load, and tire pressure are remained constant while the tire slip ratio is changed. The main tire model input signals including slip angle, slip ratio, camber angle, and normal load are measured and provided to the developed simulation environment to estimate the F&M at wheel center. The overview of the described validation test bench is presented in Figure 61.

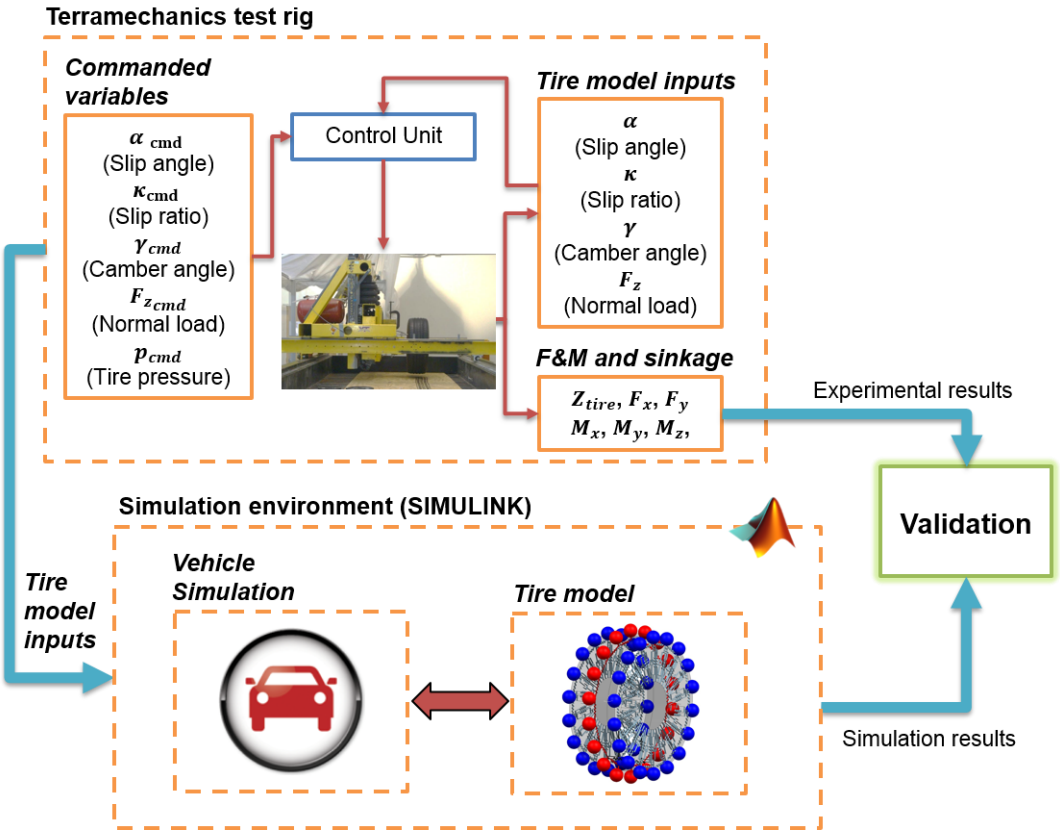

Figure 61: Validating the tire model results using experimental data from Terramechanics test rig

The forces and moments at the wheel spindle directly affect the vehicle handling and rollover behavior. In this regard, the longitudinal force, the lateral force, and the aligning moment values are the quantities of interest, because they define the planar motion of the vehicle. All the forces and moments are measured at the spindle, and the wheel sinkage is calculated using a novel method developed by Naranjo [109, 110, 133, 134]. In this method, the wheel sinkage is calculated by post-processing the data from the sensors that are implemented inside the tire cavity. These sensors are integrated units composed of a position sensitive detector (PSD), five infrared emitting diodes (IREDs), and a signal processing circuit. The similar test configuration is designed using the developed tire model platform, and simulation runs are conducted at the input conditions identical to the experimental test setup. The tire used for conducting the tests is the Michelin LTX 235/85R16. The tire tread is buffed in order to study the performance of the treadles tire.

For the longitudinal case study, the slip and camber angles were set to zero, normal load maintained near 4000 N, and slip ratio controlled at 9 different levels using the applied torque to the wheel. The test data was collected and reposted by Naranjo [133]. Three test runs were conducted at each commanded slip ratio level. It was not possible to change the slip ratio continuously from zero to its maximum value, because of the transient behavior of the soil. The longitudinal force data sets at each slip ratio are averaged between the test runs, and plotted in Figure 62 (a) with their error bars. The horizontal error bars correspond to standard deviations in slip ratio measurements, and vertical error bars are associated with the standard deviations in force readings. It can be observed that at each commanded slip ratio value, the longitudinal force have some small variations, possibly due to changes in the measured slip ratio value and normal load, in addition to irregularities in the soil compaction. Using the tire models input signals acquired from the test rig, the runs are simulated, and the results are plotted in Figure 62 (a). The developed model can estimate the overall trend of the longitudinal force vs. slip ratio curve including the slop of the linear region and the location of the peak.

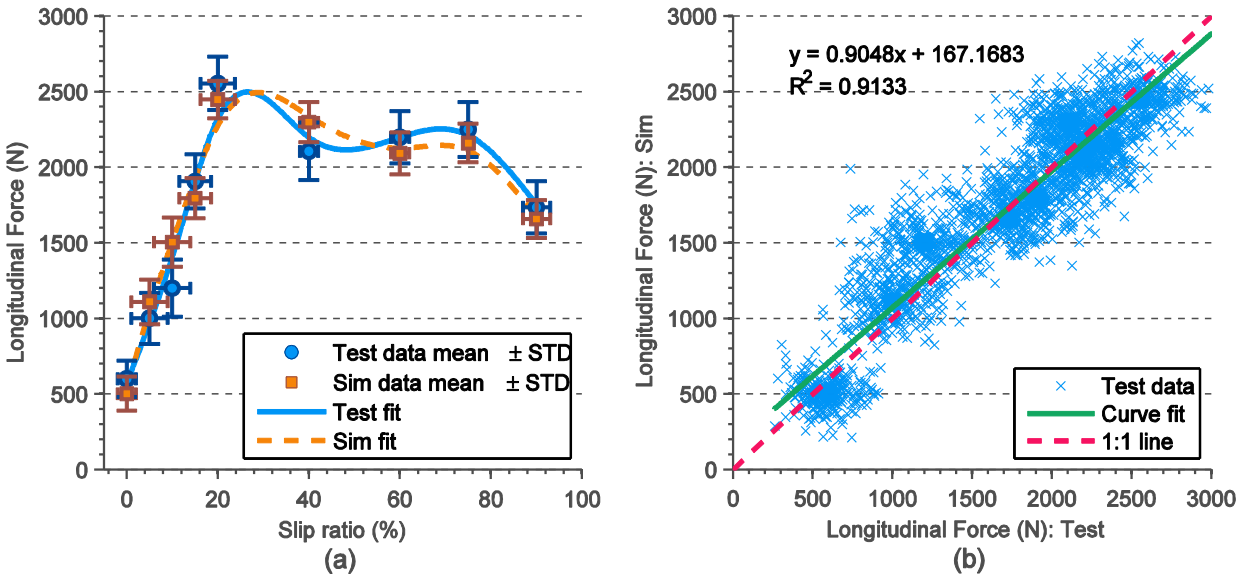

Figure 62: Longitudinal force at wheel center at different slip ratio levels (a) force vs. slip results including error bars (b) cross plot validation

The validation of the tire model response quantities versus the measurement data is done using the cross plot validation charts. For every parameter, simulation results are plotted versus the test data across the entire simulation time span. The Y-value of every blue cross on the cross plot validation chart is the simulation result at the input condition identical to test condition and the X-value is the experimental output. The simulation and experimental output signals from all of the test runs are concatenated to form the entire data points. Next, a linear line is curve-fitted to the resulted data points, and is plotted on the same figure. It should be noted that for better visualization only a reduced number of data points are shown in the cross plot validation plots.

A better approach in analyzing the simulation results is to plot them against the test data, and fit a linear line to the resulted data points. The cross-plot validation results are shown in Figure 62 (b). To assess the quality of the match, curve-fitted line properties including the slope, intersection with the Y axis and coefficient of determination (R^2) are shown on the figures. For a perfect model, the slope and coefficient of determination R^2 for this linear line should be equal to one. The R^2 index is an indication of how the data is distributed around the curve-fitted line; so, for a completely scattered data, this value will become zero. Due to the uncertainties in the experimental procedures as well as modeling approach there would be deviation between model estimations and test data. As shown in Figure 62 (b), the developed model can perform a good job in estimating the longitudinal force across the entire range of slip ratio values. The validation results for the three main response quantities, including sinkage, lateral force, and aligning moment are shown in Figure 63 to Figure 65.

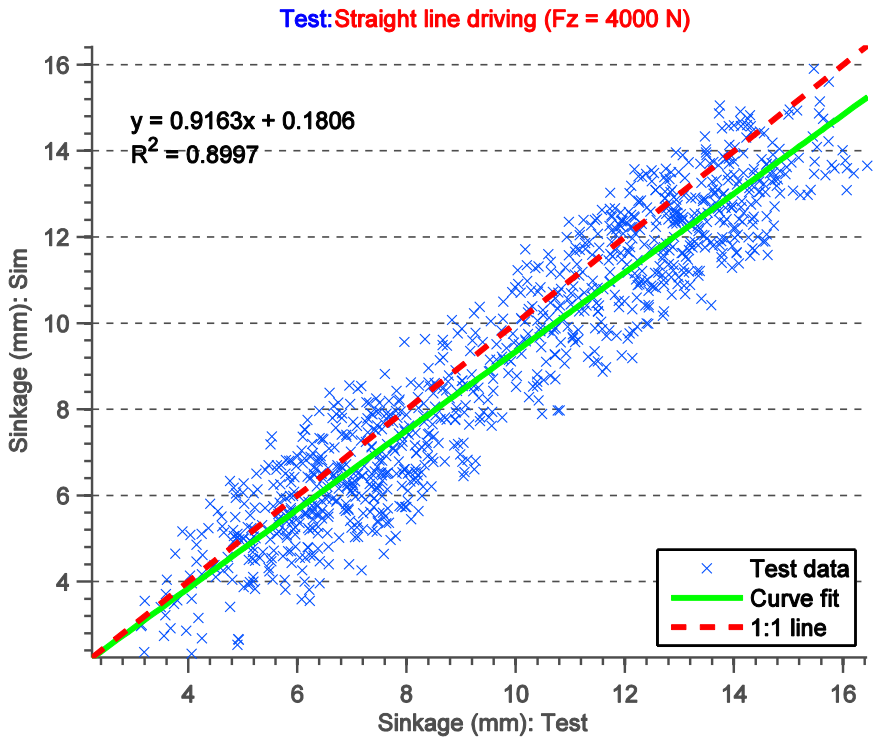

Figure 63: System response quantities cross-plot validation: wheel sinkage

Looking at the sinkage and the longitudinal force validation plots suggests that the HSSTM model performs well in estimating these parameters. The solid green curve-fitted line in the sinkage plot starts to deviate from the 1:1 line as the sinkage increases, and always remains below the red dashed line. This means that at higher sinkage values, the measured sinkage value is greater than the simulation results. The higher sinkage values occur at higher slip values, at which the tire starts to displace large volumes of soil particles and dig into the terrain. Considering the fact that the soil volume displacement model is not used in this simulation can justify the trend of the sinkage cross-plot results. The longitudinal force model has also a good performance in estimating the measurement data.

As shown in Figure 64 and Figure 65, although the test runs are performed in a straight line, the lateral force and the aligning moment values change during these maneuvers. This can be

explained by considering the following facts: (1) when the tire is traveling on a solid, non-deformable ground, it produces a lateral force and an aligning moment. This results from the plysteer and the conicity in the tire construction. The effect of these manufacturing defects is modeled as a pseudo slip angle (for plysteer) and a pseudo inclination angle (for conicity). The pseudo slip angle and the inclination angle (camber angle) cause the residual lateral force and aligning moment to appear in the straight line maneuvers; (2) The ground surface is not perfectly flat and does not have identical mechanical properties in all directions (non-isotropic). Therefore, once the tire deforms the terrain, the ground reaction force would not be parallel to the wheel direction of motion. This inclined reaction force produces a component perpendicular to the wheel plane. Additionally, when the tire sinks into the ground, soil pressure distribution is applied to the tire sidewalls from the accumulated soil pile that is displaced out of the tire path. This force is known as bulldozing force, and contributes to the lateral force and, consequently, to the aligning moment generation. The wheel carriage in the Terramechanics test rig is located relatively near the right wall of the experimental test rig. Therefore, the soil is piled up near the wall edges, and produces a pressure gradient on the tire sidewall that shifts the generated lateral force values. This effect can be observed in the shape of the lateral force cross-plot data points. Based on Figure 64, most of the blue data points are below the green solid curve-fitted line, which means that model underestimates the lateral force values throughout the simulation.

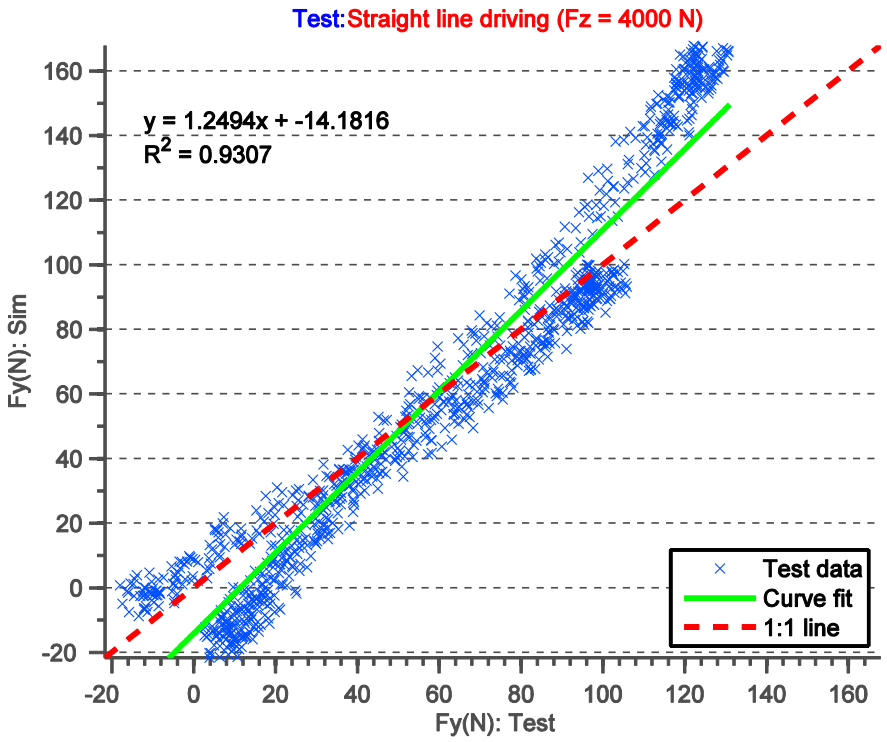

Figure 64: System response quantities cross-plot validation: lateral force at the spindle

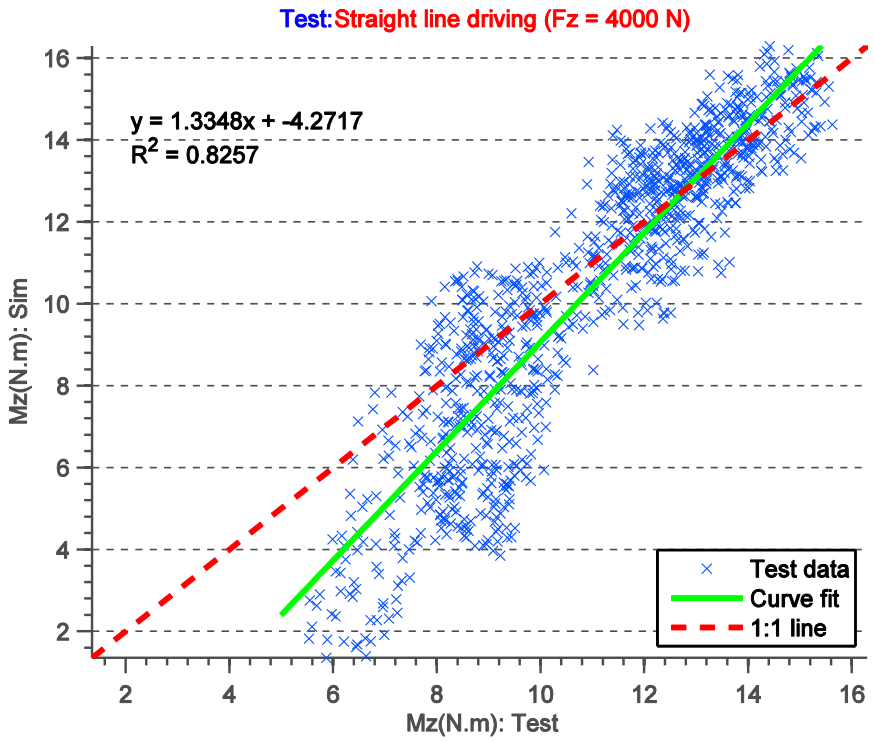

Figure 65: System response quantities cross-plot validation: aligning moment at the spindle

For the lateral case study, the tire is tested at a free rolling condition (zero slip ratio), zero camber, and 5 levels of slip angle, while the normal load is maintained near 5000 N. The test data was collected by Jimenez at the Terramechanics test rig [141]. The lateral force measurements between the three test runs are averaged and plotted in Figure 66 (a) with their associated error bars. It can be seen that at high slip angle values, the average values for the simulation data slightly deviate from the ones for the test data but their error bars have a substantial overlap. This is mostly due to the soil displacement at higher slip values. Furthermore, the cornering stiffness is relatively low because at low tire velocity during the test most of the lateral force is generated by the bulldozing force. Unlike the tire interaction with the hard surface, which causes large lateral deformation in the tire structure, the tire-soil contact mostly results in the terrain deformation and soil displacement. The cross-plot correlation results for the lateral case study are plotted in Figure 66 (b) that indicate a high correlation between the model and experimental lateral forces.

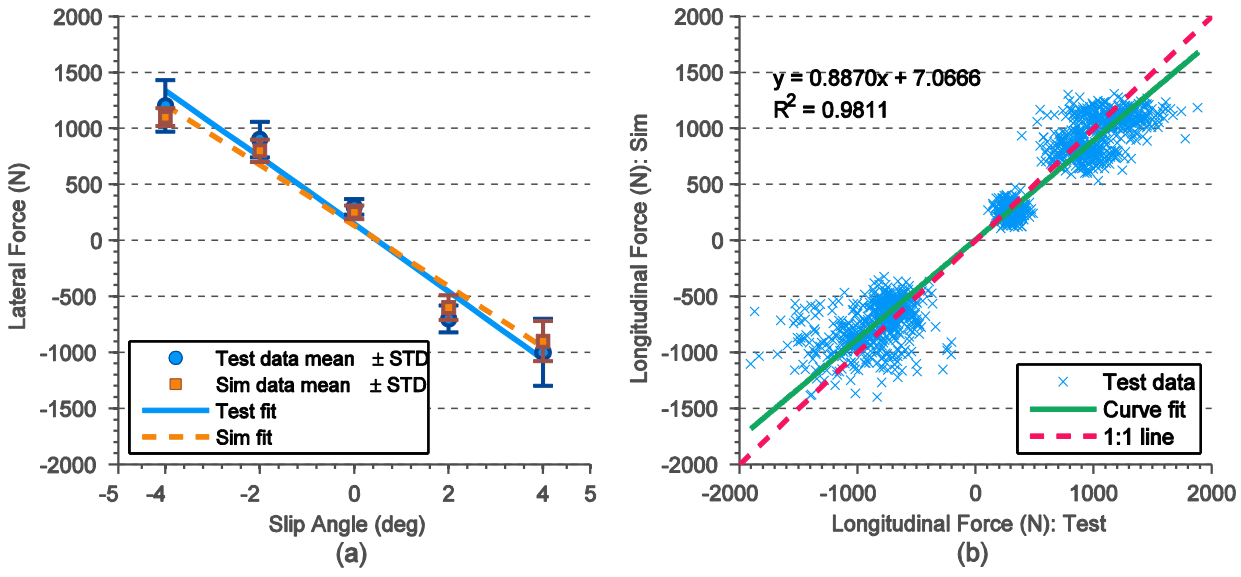

Figure 66: Lateral force at wheel center at different slip angle levels (a) force vs. slip results including error bars (b) cross plot validation

8.5. Conclusion

The verification and validation studies were discussed in this chapter. The implemented tire modeling program should correctly represent the developed mathematical model. Consequently, the verification procedures were enforced to ensure the correctness of the implemented tire model. The tire model dynamic behavior is studied in a cleat test case study. Then, the verified tire model is used to simulate the test runs conducted at the Terramechanics test rig. The signal measurements including the normal load, slip ratio, slip angle, inclination angle, and inflation pressure were input to the tire model, and tire forces and moments at the spindle as well sinkage were estimated. Finally, the cross-plot validation plots were exploited to assess the accuracy of the developed tire-terrain modeling approach.

Chapter 9: Concluding Remarks and Future Work

In order to model the dynamic behavior of the tire on soft soil, a lumped mass discretized tire model using Kelvin-Voigt elements was developed. This model, named Hybrid Soft Soil Tire Model (HSSTM), was developed to be easily linked with multibody dynamics software packages to simulate vehicle performance on deformable terrains. To optimize the computational time of the code, different techniques were used in memory allocation, parameter initialization, code sequence, and multi-processing.

To model the interaction of the HSSTM with different terrain types, two computational models were developed for evaluating non-deformable and deformable terrain behaviors. The non-deformable terrain model is a 3D distributed brush model enhanced with LuGre model for dynamic maneuvers. The developed model was integrated with the HSSTM tire model by connecting an array of deformable bristles to each of the tire belt elements. Using this approach, a predefined normal pressure distribution for the tire contact patch is not required, because the tire model can envelope over the terrain and calculate the stress distribution respectively. As a result, the contact patch pressure distribution is more accurate and will conform to the terrain profile. The experimental forces and moments data described by Magic Formula were used for parameterizing the developed terrain model using a nonlinear least square method. The terrain model was shown to provide good accuracy in estimating the tire forces and moments at different slip values and normal loads.

The terrain model for deformable terrains was based on the semi-empirical formulations that are developed using the field test data for mineral, muskeg, and snow covered terrains. Employing the empirical relations in addition to analytical approaches to describe terrain behavior helps achieving high fidelity results while keeping the computational effort and number of model

variables low. The semi-empirical formulations were implemented as incremental algorithms in a RGR environment to allow performing explicit simulations. Also, the terrain model capability in describing the pressure-sinkage and repetitive loading/unloading behavior of four different terrain types was demonstrated.

A terrain visualization module was introduced that can help debug the implemented terrain model, as well as provide a better understanding of the physics of tire-terrain interaction. Furthermore, the normal pressure and shear stress distributions across the contact patch of a driven rigid wheel on loose sand were validated against the experimental results at two different values of slip ratio. Integrating the developed terrain models with the 3D deformable HSSTM tire model, allows a dynamic pressure distribution over the tire contact patch that can result in more accurate tire force and moment estimations during tire mobility analysis.

Experimental tests were performed on the Terramechanics rig at the Advanced Vehicle Dynamics Laboratory at Virginia Tech using the Michelin LTX 235/85R16 Standard Reference Test Tire (SRTT). The tests were performed on sandy loam, and data were collected for various case studies and parameter changes.

The tire model parameter estimation was performed using a reduced finite element tire model for the same tire, modal analysis, and other experimental test procedures. Individual optimization algorithm were introduced for radial, tangential, and lateral case studies in order to find a unique set of model parameters that can minimize the error between model estimation and experimental data.

Different case studies were simulated in order to analyze the performance of the developed model. Initially, a soil multi-pass effect simulation is conducted to demonstrate the functionality of the model. Next, the tire drawbar pull coefficients on three selective terrains are estimated. It is

shown that the drawbar pull coefficients are mainly influenced by the terrain stiffness and shear deformation parameter. For evaluating the dynamic behavior of the tire, cleat test simulations are conducted, and model results are compared with three benchmarked commercially available tire models.

As for the validation case studies on deformable surfaces, a straight-line driving maneuver is conducted at constant normal load and varying slip ratio values. Using the cross-plot validation graphs it is shown that the HSSTM can estimate four main vehicle handling parameters including longitudinal force, lateral force, aligning moment, and sinkage with a reasonable accuracy. The observed discrepancies are thought to be mainly from the test conditions that are not modeled in the simulations, such as soil displacement at high slip ratios, tire construction defects (plysteer, comity), tire tread pattern, soil compaction variations, and soil bulldozing effects due to the proximity of the walls of the test rig.

9.1. Main Contributions

The main contributions of this study can be summarized as the following:

- Development of a new 3D idealization and of a mathematical model for a pneumatic tire structure using a lumped parameter approach, the simulation tool, and its integration with commercially available software.
- Development of a tire-terrain interaction module for non-deformable surfaces using the brush theory that can accommodate tire simulation on 3D roads with short-wavelength roughness.
- Development and implementation of a tire-terrain interaction module for estimating the behavior of various deformable terrains including mineral, muskeg, and snow-covered terrains.

- Development and implementation of parameterization procedures for identifying the tire and terrain model parameters from experimental data as well as from a finite element tire model.

9.2. Future Work

Furthermore, the following aspects are suggested to be incorporated for the future investigations in order to explore the integrity and the application potential of the proposed concepts in this study:

- The tire-terrain interaction during the combined slip situations that involve simultaneous driving/braking and steering should be investigated.
- Most of the tire model parameter estimation routines are automated but some still require user intervention and many trial-and-error iterations in order to achieve a set of model parameters that results in accurate tire structure behavior estimations. A robust and highly automated model parameter estimation package should be developed for HSSTM and verified for tires with different specifications.
- A closed-form analytical solution for the equations used to express tire responses to applied load/deflection inputs is essential. Deriving this solution for the complete model could be challenging, but for a simplified idealization of the tire is more practical. Having this solution would facilitate studying the tire structural behavior as well as conducting the verification and validations procedures.
- A graphical user interface can be implemented for the developed tire model that allows the end user to conduct the simulations of interest more efficiently.
- Instead of using the lumped parameter approach for representing the tire structure, a simplified FEM model can be incorporated. This approach helps representing the tire rebar

elements, specifying the tire cross-section profile, simplifying the parameterization procedures, and ultimately increasing the accuracy of tire structural responses estimations.

- A frequency analysis study is recommend to investigate the effects of terrain properties on the force and moments characteristics of the tire during interaction with deformable terrains. This would be beneficial in studying anti-lock braking system (ABS) braking and traction control systems (TCS) on soil or snow.

References

1. Gipser, M., *The FTire Tire Model Family*. 2003, Esslingen University of Applied Sciences: Esslingen, Germany. p. 18.
2. Oertel, C., *On Modeling Contact and Friction Calculation of Tyre Response on Uneven Roads.* Vehicle System Dynamics, 1997. **27**(S1): p. 289-302.
3. Oertel, C. and A. Fandre. *Ride Comfort Simulations and Steps Towards Life Time Calculations: RMOD-K and ADAMS.* in *International ADAMS User's Conference*. 1999. Berlin, Germany.
4. Gallrein, A. and M. Backer, *CDTire: A tire model for comfort and durability applications.* Vehicle System Dynamics, 2007. **45**(1): p. 69-77.
5. Pacejka, H.B. and E. Bakker, *The Magic Formula Tyre Model.* Vehicle System Dynamics, 1992. **21**(001): p. 1-18.
6. Chae, S., *Nonlinear Finite Element Modeling and Analysis of a Truck Tire*, in *Intercollege Graduate Program in Materials*. 2006, Pennsylvania State University. p. 207.
7. Mastinu, G. and E. Pairana, *Parameter Identification and Validation of a Pneumatic Tyre Model.* Vehicle System Dynamics, 1992. **21**(01): p. 58-81.
8. Gipser, M., *FTire - The tire simulation model for all applications related to vehicle dynamics.* Vehicle System Dynamics, 2007. **45**: p. 139-151.
9. Dasch, J.M. and D.J. Gorsich, *TARDEC Story: Sixty-Five Years of Innovation, 1846-2010*. 2012: Defense Department, Army, U.S. Army Tank Automotive Research, Development and Engineering Center (TARDEC).
10. Wismer, R.D. and H.J. Luth, *Off-road traction prediction for wheeled vehicles.* Journal of Terramechanics, 1973. **10**(2): p. 49-61.

11. Freitag, D.R., *A dimensional analysis of the performance of pneumatic tires on soft soils*. 1965, DTIC Document.

12. Freitag, D.R., *Performance Evaluation of Wheels for Lunar Roving Vehicles*. 1970, U.S. Army Engineer Waterways Experiment Station: Vicksburg, MS.

13. Turnage, G.W. *Tire selection and performance prediction for off-road wheeled vehicle operations*. in *Proceedings of the 4th International ISTVS Conference* 1972. Stockholm, Sweden.

14. Brixius, W.W., *Traction prediction equations for bias ply tires*, in *ASAE*. 1987. p. 162.

15. Maclaurin, E.B. *The effect of tread pattern on the field performance of tyres*. in *Proceedings of the 7th International ISTVS Conference*. 1981.

16. Maclaurin, E.B. *The use of mobility numbers to describe the in-field tractive performance of pneumatic tyres*. in *Proceedings of the 10th International ISTVS Conference, Kobe, Japan*. 1990.

17. Maclaurin, E.B. *The use of mobility numbers to predict the tractive performance of wheeled and tracked vehicles in soft cohesive soils*. in *Proceedings of the 7th European ISTVS Conference, Ferrara, Italy*. 1997.

18. Rowland, D. and J.W. Peel, *Soft ground performance prediction and assessment for wheeled and tracked vehicles.* Institute of Mechanical Engineering, 1975. **205**: p. 81.

19. Rowland, D. *Tracked vehicle ground pressure and its effect on soft ground performance*. in *Proceeding of 4th International ISTVS Conference*. 1972.

20. Hegazy, S. and C. Sandu, *Experimental investigation of vehicle mobility using a novel wheel mobility number.* Journal of Terramechanics, 2013. **50**(5–6): p. 303-310.

21. Rula, A.A., C.J. Nuttall, and U.S.A.E.W.E. Station, *An Analysis of Ground Mobility Models (ANAMOB)*. 1971: U.S. Army Engineer Waterways Experiment Station.

22. Rula, A.A. and C.J. Nuttall, *An Analysis of Ground Mobility Models (ANAMOB)*. 1971: U.S. Army Engineer Waterways Experiment Station.

23. Turnage, G.W., *Performance of Soils Under Tire loads-Application of Test Results to Tire Selection for Off-Road Vehicles*. 1972, U.S. Army Corps of Engineers Waterway Experiment Station.

24. Turnage, G.W., *Prediction of in-sand tire and wheeled vehicle drawbar performance*. 1984, DTIC Document.

25. Allen, R.W., J.P. Chrstos, and T.J. Rosenthal, *A Tire Model for Use With Vehicle Dynamics Simulations on Pavement and Off-road Surfaces.* Vehicle System Dynamics, 1997. **27**(sup001): p. 318-321.

26. Allen, R.W., T.J. Rosenthal, and J.P. Chrstos, *A Vehicle Dynamics Tire Model for Both Pavement and Off-Road Conditions (# 970559)*, in *SAE Int. Congress & Exposition*. 1997: Detroit, Michigan.

27. Metz, D., *Dynamics of Four-Wheel-Steer Off-Highway Vehicles.* SAE Technical Paper, 1993: p. 30.

28. Wong, J.Y. and A.R. Reece, *Prediction of Rigid Wheel Performance Based on the Analysis of Soil-Wheel Stresses. Part II. Performance of Towed Rigid Wheels.* Journal of Terramechanics, 1967. **4**(2): p. 7-25.

29. Madsen, J., et al., *A Physics-Based Vehicle/Terrain Interaction Model for Soft Soil Off-Road Vehicle Simulations.* SAE International Journal of Commercial Vehicles, 2012. **5**(1): p. 280-290.

30. Negrut, D. and J.S. Freeman, *Dynamic tire modeling for application with vehicle simulations incorporating terrain.* SAE transactions, 1994. **103**(6): p. 96-103.

31. Ayers, P.D. and J. Van Riper, *Stress distribution under a uniformly loaded rectangular area in agricultural soils.* Transactions of the ASAE, 1991. **34**.

32. Janosi, Z. and B. Hanamoto. *Analytical determination of draw bar pull as a function of slip for tracked vehicles in deformable soils*. in *Proceedings of the 1st International ISTVS Conference* 1961. Turin, Italy.

33. Tanaka, H., et al., *Simulation of soil deformation and resistance at bar penetration by the Distinct Element Method.* Journal of Terramechanics, 2000. **37**(1): p. 41-56.

34. Cundall, P.A. and O.D.L. Strack, *A discrete numerical model for granular assemblies.* Geotechnique, 1979. **29**(1): p. 47-65.

35. Momozu, M., et al., *Simulation of a soil loosening process by means of the modified distinct element method.* Journal of Terramechanics, 2002. **39**(4): p. 207-220.

36. Asaf, Z., D. Rubinstein, and I. Shmulevich, *Evaluation of link-track performances using DEM.* Journal of Terramechanics, 2006. **43**(2): p. 141-161.

37. Nakashima, H. and A. Oida, *Algorithm and implementation of soil–tire contact analysis code based on dynamic FE–DE method.* Journal of Terramechanics, 2004. **41**(2–3): p. 127-137.

38. Oida, A., S. Ohkubo, and H. Schwanghart. *Effect of tire lug cross section on tire performance simulated by distinct element method*. in *Proceeings of the 13th International ISTVS Conference*. 1999.

39. Nakashima, H. and J.Y. Wong, *A three-dimensional tire model by the finite element method.* Journal of Terramechanics, 1993. **30**(1): p. 21-34.

40. Nakashima, H. and J.Y. Wong, *A Three Dimensional Tire Model by the Finite Element Method.* Journal of Terramechanics, 1993. **30**(1): p. 21-34.

41. Nakashima, H. and M. Yamazaki. *3D FEM procedure for static sinkage problems of tire on soil surface*. in *Proceedings of the ARBIP95, Japanese Society of Agricultural Machinery*. 1995. Kobe, Jepan.

42. Wakui, F. and Y. Terumichi, *Numerical Simulation of Tire Behavior on Soft Ground.* Journal of System Design and Dynamics, 2011. **5**(3): p. 486-500.

43. Wakui, F. and Y. Terumichi, *Numerical Simulation of Tire-Ground System Considering Soft Ground Characteristics.* Journal of System Design and Dynamics, 2011. **5**(8).

44. Wong, J.Y., *Theory of Ground Vehicles*. 4th ed. 2008, Hoboken, NJ: John Wiley & Sons.

45. Smith, W. and H. Peng, *Modeling of wheel–soil interaction over rough terrain using the discrete element method.* Journal of Terramechanics, 2013. **50**(5–6): p. 277-287.

46. Kloss, C. and C. Goniva. *LIGGGHTS A new open source discrete element simulation software*. in *Proceedings of The Fifth International Conference on Discrete Element Methods, London, UK*. 2010.

47. Ai, J., et al., *Assessment of rolling resistance models in discrete element simulations.* Powder Technology, 2011. **206**(3): p. 269-282.

48. Hopkins, M.A., J.B. Johnson, and R.J. Sullivan, *Discrete element modeling of a rover wheel in granular material under the influence of Earth, Mars, and Lunar Gravity.* Proceedings of Earth & Space, 2008.

49. Knuth, M.A., et al., *Discrete element modeling of a Mars Exploration Rover wheel in granular material.* Journal of Terramechanics, 2012. **49**(1): p. 27-36.

50. Ding, L., et al., *Experimental study and analysis on driving wheels' performance for planetary exploration rovers moving in deformable soil.* Journal of Terramechanics, 2011. **48**(1): p. 27-45.

51. Taheri, S., *Finite Element Modeling of Tire-Terrain Dynamic Interaction for Full Vehicle Simulation Application* in *Mechanical Engineering* 2014, Virginia Tech Blacksburg, Virginia

52. Taheri, S., C. Sandu, and S. Taheri, *Finite Element Modeling of Tire Transient Characteristics in Dynamic Maneuvers.* SAE Int. J. Passeng. Cars - Mech. Syst., 2014. **7**(1): p. 221-230.

53. Mootaz Abo-Elnor, R. and J.T.B. Hamilton, *3D Dynamic analysis of soil–tool interaction using the finite element method.* Journal of Terramechanics, 2003. **40**: p. 51-62.

54. Yong, R.N., E.A. Fattah, and R.N. Boonsinsuk, *Analysis and Prediction of Tyre-Soil Interaction and Performance Using Finite Elements.* Journal of Terramechanics, 1978. **15**(1): p. 43-63.

55. Yong, R.N. and E.A. Fattah, *Prediction of wheel-soil interaction and performance using the finite element method.* Journal of Terramechanics, 1976. **13**(4): p. 227-240.

56. Yong, R.N. and E. Windisch, *Determination of wheel contact stresses from measured instantaneous soil deformations.* Journal of Terramechanics, 1970. **7**(3): p. 57-67.

57. Yong, R.N., P. Boonsinsuk, and E.A. Fattah, *Tyre Flexibility and Mobility on Soft Soils.* Journal of Terramechanics, 1980. **17**(1): p. 43-58.

58. Shoop, S.A., *Finite Element Modeling of Tire–Terrain Interaction*. 2001, US Army Corps of Engineers: Hanover, NH.

59. Darnell, I., G.M. Hulbert, and C.W. Mousseau, *An Efficient Three-Dimensional Tire Model for Vehicle Dynamics Simulations**. Journal of Structural Mechanics, 1997. **25**(1): p. 1-19.

60. Shoop, S.A., K. Kestler, and R. Haehnel, *Finite Element Modeling of Tires on Snow 2.* Tire science and technology, 2006. **34**(1): p. 2-37.

61. Iizuka, K., Y. Kunii, and T. Kubota. *Study on wheeled forms of lunar robots for traversing soft terrain*. in *Intelligent Robots and Systems, 2008. IROS 2008. IEEE/RSJ International Conference on*. 2008. IEEE.

62. Fervers, C.W., *Improved FEM simulation model for tire–soil interaction.* Journal of Terramechanics, 2004. **41**(2): p. 87-100.

63. Fervers, C.W. *Phenomena of tire-profile on different soils*. in *Proceedings of the 13th International ISTVS Conference* 1999. München, Germany.

64. Lee, J. and Q. Kiu. *Modeling and simulation of in-plane and out-of-plane forces of pneumatic tires on fresh snow based on the finite element method*. in *Proceedings of the Joint North America, Asia-Pacific ISTVS Conference and Annual Meeting of Japanese Society for Terramechanics, University of Alaska, Fairbanks, AK, USA*. 2007. Intec.

65. Grujicic, M., et al., *Computational analysis of mine blast on a commercial vehicle structure.* Multidiscipline Modeling in Materials and Structures, 2007. **3**(4): p. 431-460.

66. Grujicic, M., et al., *A finite element analysis of pneumatic-tire/sand interactions during off-road vehicle travel.* Multidiscipline Modeling in Materials and Structures, 2009. **6**(2): p. 284-308.

67. Xia, K., *Finite element modeling of tire/terrain interaction: Application to predicting soil compaction and tire mobility.* Journal of Terramechanics, 2010. **48**(2): p. 113-123.

68. Wang, L.-R. and Z.-H. Lu, *Modeling method of constitutive law of rubber hyperelasticity based on finite element simulations.* Rubber chemistry and technology, 2003. **76**(1): p. 271-285.

69. Bolarinwa, E.O. and O.A. Olatunbosun, *Finite element simulation of the tyre burst test.* Proceedings of the Institution of Mechanical Engineers, Part D: Journal of Automobile Engineering, 2004. **218**(11): p. 1251-1258.

70. Ghoreishy, M.H.R., *Finite element analysis of the steel-belted radial tyre with tread pattern under contact load.* Iranian Polymer Journal, 2006. **15**(8): p. 667-674.

71. Han, L.H., et al., *A modified Drucker-Prager Cap model for die compaction simulation of pharmaceutical powders.* International Journal of Solids and Structures, 2008. **45**(10): p. 3088-3106.

72. Li, H. and C. Schindler, *Analysis of soil compaction and tire mobility with finite element method.* Proceedings of the Institution of Mechanical Engineers, Part K: Journal of Multi-body Dynamics, 2013.

73. Taheri, S. and T. Wei, *A New Semi-Empirical Method for Estimating Tire Combined Slip Forces and Moments during Handling Maneuvers.* SAE International Journal of Passenger Cars-Mechanical Systems, 2015. **8**(2015-01-9112): p. 797-815.

74. Taheri, S., C. Sandu, and S. Taheri, *Hybrid Soft Soil Tire Model (HSSTM). Part II: Tire-Terrain Interaction Modeling.* Journal of Terramechanics, 2015.

75. Taheri, S., et al., *A technical survey on Terramechanics models for tire–terrain interaction used in modeling and simulation of wheeled vehicles.* Journal of Terramechanics, 2015. **57**: p. 1-22.

76. Taheri, S., et al., *Hybrid Soft Soil Tire Model (HSSTM). Part I: Tire Material and Structure Modeling.* Journal of Terramechanics, 2015.

77. Bekker, M.G., *Introduction to Terrain-Vehicle System*. 1969: Ann Arbor: The University of Michigan Press.

78. Bekker, M.G., *Off the Road Locomotion*. 1960, Ann Arbor, Michigan: University of Michigan Press.

79. Bekker, M.G., *The Theory of Land Locomotion*. 1956, Ann Arbor, Michigan: University of Michigan Press.

80. Bekker, M.G., *Theory of Land Locomotion : The Mechanics of Vehicle Mobility*. 1956: Ann Arbor: The University of Michigan Press.

81. Wong, J.Y. and J. Preston-Thomas, *On the Characterization of the Shear Stress-Displacement Relationship of Terrain.* Journal of Terramechanics, 1983. **19**(4): p. 225-234.

82. Wong, J.Y., *On The Study of Wheel-Soil Interaction.* Journal of Terramechanics, 1984. **21**(2): p. 117-131.

83. Wong, J.Y. and A.R. Reece, *Prediction of Rigid Wheel Performance Based on the Analysis of Soil-Wheel Stresses. Part I. Performance of Driven Rigid Wheels.* Journal of Terramechanics, 1967. **4**(1): p. 81-98.

84. Wong, J.Y., *Terramechanics and Off-Road Vehicle Engineering: Terrain Behaviour, Off-Road Vehicle Performance and Design*. 2nd Edition ed. 2010, Amsterdam, The Netherlands: Elsevier.

85. Wong, J.Y. and V.M. Asnani, *Study of the correlation between the performances of lunar vehicle wheels predicted by the Nepean wheeled vehicle performance model and test data.*

Proceedings of the Institution of Mechanical Engineers, Part D: Journal of Automobile Engineering, 2008. **222**(11): p. 1939-1954.

86. Chan, B.J., *Development of an off-road capable tire model for vehicle dynamics simulations*, in *Mechanical Engineering*. 2008, Virginia Tech: Blacksburg, VA. p. 226.

87. Chan, B.J. and C. Sandu, *Development of a 3-D Quasi-static Tire Model for On-road and Off-road Vehicle Dynamics Simulations: Part III–Off-road Flexible Wheel Model.* International Journal of Vehicle Systems Modelling and Testing, 2014. **9**(2): p. 151-176.

88. Chan, B.J. and C. Sandu, *Development of a 3-D Quasi-static Tire Model for On-road and Off-road Vehicle Dynamics Simulations: Part II–Off-road Rigid Wheel Model.* International Journal of Vehicle Systems Modelling and Testing, May 2014. **9**(2): p. 107-136.

89. Chan, B.J. and C. Sandu, *Development of a 3-D Quasi-static Tire Model for On-road and Off-road Vehicle Dynamics Simulations: Part I–On-road Flexible Tire Model.* International Journal of Vehicle Systems Modelling and Testing, 2014. **9**(1): p. 77-105

90. Yu, Z.-X., et al., *A Simple Analysis Method for Contact Deformation of Rolling Tire.* Vehicle System Dynamics, 2001. **36**(6): p. 435-443.

91. Reece, A.R. *Principles of soil-vehicle mechanics*. in *Proceedings of the Institution of Mechanical Engineers: Automobile Division*. 1965. Sage publications.

92. Janosi, Z. and B. Hanamoto. *The analytical determination of drawbar pull as a function of slip for tracked vehicles in deformable soils*. in *Proceedings of the 1st International Conference on the Mechanics of Soil–Vehicle Systems* 1961. Turin, Italy.

93. Senatore, C. and C. Sandu, *Off-road tire modeling and the multi-pass effect for vehicle dynamics simulation.* Journal of Terramechanics, 2011. **48**(4): p. 265-276.

94. Senatore, C., *Prediction of mobility, handling, and tractive efficiency of wheeled off-road vehicles*, in *Mechanical Engineering*. 2010, Virginia Tech: Blacksburg, VA.

95. Senatore, C. and C. Sandu, *Torque distribution influence on tractive efficiency and mobility of off-road wheeled vehicles.* Journal of Terramechanics, 2011. **48**(5): p. 372-383.

96. Liang, C.Y., et al., *Tire Modeling for Off-Road Vehicle Simulations.* SAE, 2004. **113**(6): p. 1063-1073.

97. Christoffersen, S.R., et al. *Deceleration factors on off-road surfaces applicable for accident reconstruction*. in *SAE Publication SP-1083. Accident Reconstruction: Technology And Animation V. Proceedings Of The International Congress And Exposition, February 27-March 2, 1995, Detroit, Michigan, USA*. 1995.

98. Harnisch, C., et al., *A new tyre soil interaction model for vehicle simulation on deformable ground.* International Journal of Vehicle Mechanics and Mobility, 2005. **43**(1): p. 384-394.

99. Schmid, I.C. and J. Ludewig. *Improved calculation of sinkage of a wheel on soft ground*. in *Proceedings of the 5th European ISTVS Conference* 1991. Budapest, Hungary.

100. Schmid, I.C., *Interaction of Vehicle and Terrain Results from 10 Years Research at IKK.* Journal of Terramechanics, 1995. **32**(1): p. 3-26.

101. Schwanghart, H., *Lateral Forces on Steered Tyres in Loose Soil.* Journal of Terramechanics, 1968. **5**(1): p. 9-29.

102. Schwanghart, H., *Measurement of Contact Area, Contact Pressure and Compaction Under Tires in Soft Soil.* Journal of Terramechanics, 1991. **28**(4): p. 309-318.

103. Krenn, R. and A. Gibbesch, *Soft Soil Contact Modeling Technique for Multi-Body System Simulation.* Trends in Computational Contact Mechanics, 2011. **58**: p. 135–155.

104. Krenn, R. and G. Hirzinger. *Simulation of rover locomotion on sandy terrain-modeling, verification and validation*. in *Proceedings of the 10th Workshop on ASTRA, Noordwijk, The Netherlands*. 2008.

105. Gipser, M., *FTire: 10 Years of Development and Application*. 2008, Esslingen: Esslingen University of Applied Sciences. 13.

106. Gipser, M., *FTire – the tire simulation model for all applications related to vehicle dynamics.* Vehicle System Dynamics, 2007. **45**(sup1): p. 139-151.

107. Gipser, M. *Cosin/Road, Cosin Road Modeling*. Available from: https://www.cosin.eu/res/cosinroad.pdf.

108. Pinto, E., *A Three Dimensional Discretized Tire Model for Soft Soil Applications*, in *Mechanical Engineering*. 2012, Virginia Tech: Blacksburg, VA.

109. Sandu, C., et al. *Off-Road Soft Soil Tire Model and Experimental Testing*. in *Proceedings of the 12th European ISTVS Conference* 2012. Pretoria, South Africa.

110. Sandu, C., et al. *Off-Road Soft Soil Tire Model Development, Validation, and Interface to Commercial Multibody Dynamics Software*. in *Proceedings of the 17th International ISTVS Conference* 2011. Blacksburg, VA, USA.

111. Umsrithong, A. and C. Sandu, *A 3D semi-empirical on-road transient tire model.* SAE International Journal of Commercial Vehicles, 2010. **3**(1): p. 42-59.

112. Umsrithong, A. and C. Sandu. *A 3D semi-empirical stochastic tire model on hard flat and uneven surfaces*. in *International Congress on Automotive and Transport Engineering*. 2010. Brasov, Romania.

113. Umsrithong, A., *Deterministic and Stochastic Semi-Empirical Transient Tire Models*. 2012, Virginia Tech: Blacksburg, VA.

114. Umsrithong, A. and C. Sandu. *Parameter Identification and Experimental Validation of a Discrete Mass Tire Model for Uneven Rigid Terrain*. in *Proceedings of ASME 2012 IDETC/CIE 14th International Conference on Advance Vehicle Technologies (AVT)*. 2012. Chicago, IL: American Society of Mechanical Engineers.

115. Umsrithong, A. and C. Sandu, *A Semi-Empirical Tire Model for Transient Maneuver of On Road Vehicle*, in *SAE Commercial Vehicle Engineering Congress and Exposition*. 2009: Chicago, IL. p. 9.

116. Umsrithong, A. and C. Sandu, *Stochastic transient tyre model for vehicle dynamic simulations on rough rigid ground.* International Journal of Vehicle Systems Modelling and Testing, 2012. **7**(4): p. 351-371.

117. Taheri, S., et al. *Off-road Soft Soil Tire Model*. in *7th Americas Regional ISTVS Conference* 2013. Tampa, FL.

118. Fassbender, F.R. *Soil-Tire Interface for the Rigid Body Simulation Program ADAMS - Simulation of the Dynamic Vehicle-Soil Interaction*. in *Proceedings of the 12th Internationa ISTVS Conference* 1996. Hamburg, Germany.

119. Fassbender, F.R. *Vehicle Oscillation on Soft Soil Simulated with STINA*. in *Proceedings of the 7th European ISTVS Conference* 1997. Hamburg: University of the Federal Armed Forces.

120. Taylor, B.P., *Experimental Evaluation and Semi-Empirical Modeling of the Tractive Performance of Rigid and Flexible Wheels on Lunar Soil Simulant*, in *Mechanical Engineering*. 2009, Virginia Tech: Blacksburg, VA. p. 172.

121. Scharringhausen, M., *Martian, terrestrial and lunar soil parameters*. 2008, DLR Internal Report.

122. Gipser, M. *FTire - Flexible Ring Tire Model, Modelization and Parameter Specifications*. 2013 April 17th]; Available from: https://www.cosin.eu/res/ftire_model.pdf.

123. Taheri, S., C. Sandu, and S. Taheri. *Development and Implementation of a Hybrid Soft Soil Tire Model (HSSTM)*. in *The 18th International ISTVS Conference Seoul, Korea.* 2014.

124. Zavarise, G. and L. De Lorenzis, *The node-to-segment algorithm for 2D frictionless contact: Classical formulation and special cases.* Computer Methods in Applied Mechanics and Engineering, 2009. **198**(41–44): p. 3428-3451.

125. Pacejka, H.B., and Bakker, E., *The Magic Formula Tyre Model.* Vehicle System Dynamics, 1992. **21**(001): p. 1-18.

126. Mastinu, G. and E. Pairana, *Parameter Identification and Validation of a Pneumatic Tyre Model.* Vehicle System Dynamics, 1992. **21**(sup001): p. 58-81.

127. Oertel, C., and Fandre, A. *Ride Comfort Simulations and Steps Towards Life Time Calculations: RMOD-K and ADAMS*. in *International ADAMS User's Conference*. 1999. Berlin, Germany.

128. Gallrein, A., and Backer, M. , *CDTire: a tire model for comfort and durability applications.* Vehicle System Dynamics, 2007. **45**(1): p. 69-77.

129. Pacejka, H., *Tire and vehicle dynamics*. 2005: Elsevier.

130. McCullough, M. and E. Haug, *Dynamics of high mobility track vehicles.* Journal of Mechanical Design, 1986. **108**(2): p. 189-196.

131. Onafeko, O. and A. Reece, *Soil stresses and deformations beneath rigid wheels.* Journal of Terramechanics, 1967. **4**(1): p. 59-80.

132. Lugner, P. and M. Plöchl, *Tyre model performance test: First experiences and results.* Vehicle System Dynamics, 2005. **43**(sup1): p. 48-62.

133. Naranjo, S., *Experimental Investigation of the Tractive Performance of an Instrumented Off-Road Tire on a Soft Soil Terrain*, in *Mechanical Engineering*. 2013, Virginia Polytechnic Institute and State University: Blacksburg, VA.

134. Naranjo, S.D., et al., *Experimental testing of an off-road instrumented tire on soft soil.* Journal of Terramechanics, 2014. **56**(0): p. 119-137.

135. Singh, K., *Development of an Intelligent Tire Based Tire-Vehicle State Estimator for Application to Global Chassis Control.* Mechanical Engineering Dept, Virginia Tech, Blacksburg, 2012.

136. Dennis Jr, J.E., D.M. Gay, and R.E. Walsh, *An adaptive nonlinear least-squares algorithm.* ACM Transactions on Mathematical Software (TOMS), 1981. **7**(3): p. 348-368.

137. Marquardt, D.W., *An algorithm for least-squares estimation of nonlinear parameters.* Journal of the Society for Industrial & Applied Mathematics, 1963. **11**(2): p. 431-441.

138. Bellavia, S., M. Macconi, and B. Morini, *An affine scaling trust-region approach to bound-constrained nonlinear systems.* Applied Numerical Mathematics, 2003. **44**(3): p. 257-280.

139. Coleman, T.F. and Y. Li, *A reflective Newton method for minimizing a quadratic function subject to bounds on some of the variables.* SIAM Journal on Optimization, 1996. **6**(4): p. 1040-1058.

140. Zegelaar, P.W.A., *The dynamic response of tyres to brake torque variations and road unevenesses*. 1998: TU Delft, Delft University of Technology.

141. Jimenez, E. and C. Sandu, *Handling Performance of Pneumatic Tires on Sandy Loam*, in *The 13th European Conf. of the ISTVS*. 2015: Rome, Italy.